University of Granada

Department of Computer Architecture and Technology

Doctoral Program in Information and
Communication Technologies

Simulation Models and Tools of the Early Stages of the Visual System

Presented by

Pablo Martínez Cañada

Supervised by

Prof. Francisco J. Pelayo Valle

Prof. Christian A. Morillas Gutiérrez

April 2018

Universidad de Granada

Departamento de Arquitectura y Tecnología de Computadores

Programa de Doctorado en Tecnologías de la Información y la Comunicación

Modelos y Herramientas de Simulación de las Primeras Etapas del Sistema Visual

Presentada por

Pablo Martínez Cañada

Dirigido por

Prof. Francisco J. Pelayo Valle

Prof. Christian A. Morillas Gutiérrez

Abril, 2018

Editor: Universidad de Granada. Tesis Doctorales
Autor: Pablo Martínez Cañada
ISBN: 978-84-9163-985-5
URI: http://hdl.handle.net/10481/53591

Abstract

The focus of this thesis was on the implementation of software tools and biological models that simulate the neuronal behavior of the first stages of the visual system, retina, lateral geniculate nucleus (LGN) and primary visual cortex (V1), and can serve as a realistic experimentation framework within which several hypotheses of the neural coding of visual processing can be explored.

First, we developed an efficient software platform that facilitates the implementation of retina models at different abstraction levels, from single-cell to large-scale network levels. The platform provides a set of computational retinal microcircuits as basic building blocks that can be combined to form different retina architectures. To show the configurability and potential of the proposed framework, we constructed a series of different retina models that capture the properties of the retina response for some of the best-known phenomena observed in the retina: adaptation to the mean light intensity and temporal contrast, and differential motion sensitivity.

The next stage that was investigated was the LGN. A striking feature of the LGN circuit is that LGN cells, both relay cells (RCs) and interneurons (INs), not only receive feedforward input from retinal ganglion cells (GCs), but also a prominent feedback from cells in layer 6 of V1. We explored the spatial effects of cortical feedback on the relay-cell response by means of a biophysically detailed network model. We considered two different arrangements of synaptic feedback from the ON and OFF zones in V1 to the LGN, as well as different spatial extents of the corticothalamic projection pattern. Our simulation results are in agreement with the feedback-evoked increase in center-surround antagonism observed in experiments both for flashing spots and, even more prominently, for patch gratings.

Finally, we developed a comprehensive network model of the first stages in the primate parvocellular pathway, built upon two-dimensional grids of point neurons, which represent the retina, the LGN and a simplified version of the multilayered structure of V1. Special attention was given to ensuring that the morphological properties of the network (e.g., spatial extent of connections) were based strictly on experimental data of the primate visual system. We exhaustively benchmarked the model against well-established chromatic and achromatic visual stimuli, showing spatial and temporal responses of the model to light flashes of different shapes, spatially uniform squares and sine-wave gratings of varying spatial frequency. The model was used to validate a hypothesis that is under debate and concerns the spatial properties of the V1 response to surfaces of uniform color. According to this hypothesis, V1 population responses to chromatic and achromatic surfaces remain both edge-enhanced throughout the stimulus presentation but only achromatic surfaces elicit a neuronal *filling-in* response of the center.

In parallel, different optimization strategies based on genetic algorithm (GA) were investigated to fit parameters of some of the models proposed in this work.

Resumen

El trabajo de esta Tesis se ha centrado en la implementación de herramientas software y modelos biológicos que simulan el comportamiento neuronal de las primeras etapas del sistema visual, retina, núcleo geniculado lateral (LGN) y corteza visual primaria (V1), y que constituyen una plataforma de experimentación realista en la cual se pueden explorar diferentes hipótesis de la codificación neuronal del procesamiento visual.

En primer lugar hemos desarrollado una plataforma software eficiente que facilita la implementación de modelos de retina a diferentes niveles de abstracción, desde el nivel celular hasta niveles de red de gran escala. La plataforma proporciona un conjunto de microcircuitos computacionales de la retina que pueden ser combinados como unidades básicas de procesamiento para formar diferentes arquitecturas de retina. Para demostrar la configurabilidad y el potencial de la plataforma, se han desarrollado una serie de modelos diferentes de retina que reproducen las propiedades de la respuesta retiniana para algunos de los fenómenos mejor conocidos: adaptación al nivel medio de intensidad lumínica y al contraste temporal, y sensibilidad al movimiento.

La siguiente etapa que se ha investigado es el LGN. Una propiedad sorprendente de este circuito es que las células del LGN, tanto las "relay-cells" (RCs) como las interneuronas (INs), no sólo reciben entrada "feedforward" de las células ganglionares (GCs) de la retina, sino que también reciben un marcado "feedback" de las células de capa 6 de V1. Hemos explorado los efectos del "feedback" cortical en la respuesta espacial de las RCs usando para ello un modelo de red biofísicamente detallado. Se han considerado dos organizaciones distintas de las conexiones sinápticas de "feedback" que provienen de las zonas ON y OFF en V1, así como diferentes tamaños de la proyección espacial corticotalámica. Nuestros resultados de simulación están en conformidad con el aumento del antagonismo centro-periferia, evocado por la señal de "feedback", observado en experimentos con destellos de forma circular y, de forma más prominente, con rejillas sinusoidales.

Finalmente se ha desarrollado un modelo de red exhaustivo de las primeras etapas del camino parvocelular del primate, construido en base a capas bi-dimensionales de neuronas unicompartimentales, que representan la retina, el LGN y una versión simplificada de la estructura multi-capas de V1. Se ha prestado especial atención en asegurar que las propiedades morfológicas de la red (e.g., la extensión espacial de las conexiones) estén basadas estrictamente en datos experimentales del sistema visual del primate. El modelo se ha evaluado de forma minuciosa, usando estímulos cromáticos y acromáticos, y mostrando las respuestas espaciales y temporales del

modelo a destellos lumínicos de diferentes formas, cuadrados espacialmente uniformes y rejillas sinusoidales de distinta frecuencia espacial. El modelo ha sido usado para validar una hipótesis que todavía está siendo debatida y que está relacionada con las propiedades espaciales de la respuesta de V1 a superficies uniformes de color. Esta hipótesis postula que las respuestas de la población de V1 para superficies cromáticas y acromáticas permanecen ambas con un nivel alto de activación en los bordes a lo largo de la presentación del estímulo pero sólo las superficies acromáticas provocan una respuesta de "filling-in" en el centro de la superficie.

En paralelo, hemos investigado diferentes estrategias de optimización basadas en algoritmo genético (GA) para ajustar los parámetros de algunos de los modelos propuestos en este trabajo.

Acknowledgements

I would like to express my sincere gratitude to my supervisors, Prof. Francisco J. Pelayo Valle and Prof. Christian A. Morillas Gutiérrez, for their tireless support and unbelievable amount of patience and comprehension. I would also like to thank my family and friends for supporting me with their endless love and for being there when I needed them the most.

I wish to thank staff of CINPLA, University of Oslo, for their hospitality and support during my research stay. They also gave me the opportunity to use the Stallo supercomputer cluster at Notur, the Norwegian metacenter for computational science.

This work has been supported by the PhD scholarship FPU13/01487 and the research stay grant EST15/00055, both awarded by the Government of Spain, FPU program. Additional funding was also received from the Human Brain Project (FET project 604102), grants TIN2013-47069-P, TIN2015-67020-P and TIN2016-81041-R by the Spanish government, and the research project P11-TIC-7983 of "Junta de Andalucía" (Spain), cofinanced by the European Regional Development Fund (ERDF).

Contents

List of Figures

Acronyms

AC: Amacrine cell

BC: Bipolar cell

CL: Color-luminance (cell)

CP: Color-preferring (cell)

DoG: Difference-of-Gaussians

GA: Genetic algorithm

GC: Ganglion cell

HBP: Human Brain Project

HC: Horizontal cell

IF: Integrate-and-fire (model)

IN: Interneuron

LGN: Lateral geniculate nucleus

LP: Luminance-preferring (cell)

RC: Relay cell

V1: Primary visual cortex

Chapter 1

Introduction

1.1 Motivation and Objectives

This thesis falls within the field of Computational Neuroscience. Computational Neuroscience comprises the study of the brain function in terms of the information processing properties and the network architecture that make up the neuronal system. It is an interdisciplinary science that links the diverse fields of Neuroscience, Cognitive science and Psychology with Electrical Engineering, Computer Science, Mathematics and Physics. Computational Neuroscience is currently at the epicenter of one of the most important European project, the H2020 FET Flagship Project Human Brain Project (HBP) [HBP18], in which our research group is involved in. Part of the work presented here has also been focused on the HBP.

Mathematical and computational modeling have played a crucial role to understand the functionality of the visual, auditory and olfactory systems, as well as the neural basis of learning and memory [Min18]. There exist computational models of other types of physical systems (e.g., planetary systems, fluid flows, and so on). However, biological structures of the nervous system can be seen as processors of information so that computational models in these systems are not just tools for calculation or prediction, but often for inferring their functionality.

To extract the functionality of the nervous system, it is essential to explain how phenomena at each level arise from those at lower levels (e.g., how neuronal activity of cells in the visual cortex produce the perception of color). Unfortunately, experimental methods often do not provide the data necessary for this. Electrode arrays, for example, provide extracellular access only to a few hundred neurons at best. Computational modeling bridges the gap between incomplete experimental data and a coherent quantitative and testable functional description of the brain. Computational modeling allows us to develop large-scale network models, based on data obtained from experiments, and simulate them computationally under a variety of situations to gain insight into how the corresponding networks in the brain might work.

Computational models of the visual system have been of particular interest. The visual system has drawn the attention of many scientists over the last sixty years, since the seminal work of Hubel and Wiesel [HW62, HW59], which was the landmark in exploring how neurons in the brain could be organized to produce visual perception. Vision is the primary sensory modality in primates such ourselves, and the complexity of the visual system is reflected in the extent of the cerebral cortex used for the analysis of visual information [KVE92]. The working of the visual system is a matter of fascination not only for our understanding of visual perception, but also for its relevance to other cortical functions, including cognitive processing.

A great number of models have been proposed to explain the properties of the visual processing. One of the pioneers in the field, and maybe the best known mathematical model in visual neuroscience, was the Difference-of-Gaussians (DoG) introduced in 1965 by R.W. Rodieck [Rod65]. Descriptive models, such as the DoG, have been essential to understand how neurons convert visual stimuli into a neural response. With recent advancements in neuroimaging techniques, availability of an increasing amount of physiological data and current computational capabilities, we now have powerful resources for developing biologically more realistic models of the brain.

This thesis has been primarily focused on the development of computational models of the early stages of the visual system that could bring novel and valuable tools to the Neuroscience community. In general terms, we set the following goals:

- To generalize the computational basis of the visual processing, rather than fitting the model response to a single experimental observation. While many of the proposed models for vision share common computational stages, previous efforts have been more focused on fitting specific experimental data rather than generalizing the model beyond a particular result. We exhaustively benchmarked our models against a large repertoire of different visual stimuli, in which the model responses were well within the range of values experimentally reported for all types of stimuli. We believe that a general and unified modeling framework should be pursued to facilitate the construction of a coherent description of the visual system.

- To achieve the best tradeoff between complexity of the models to explain functionality and biological accuracy. Thus, our proposed models are as simple as possible (e.g., they are mainly built upon point neuron models) but are able to capture most properties of the neural response. Although the models have been largely simplified, it does not mean their parameter values do not correspond to biological values. In fact, it is just the opposite. Special attention was given to ensuring that morphological and physiological properties of the models were based strictly on experimental data.

- For the purpose of independent validation and further scientific exploration, these models were implemented using well-established simulation tools, such as NEST [NES18], and all the code projects have been released as open source software [Git18].

1.2 Contributions

The biologically realistic models presented in this Thesis have the ultimate goal of gaining insight into the neural mechanisms underlying the early processing of visual information. A number of hypotheses raised on the basis of experimental findings were evaluated by means of model simulations under different scenarios. Compared to other biological models for vision, our models make the following contributions:

- Our software might be considered as an evolutionary tool for neuroscientists who need realistic large-scale and relatively detailed models of the visual system. The category of large-scale models appears under-represented in the literature. We will illustrate the importance of large-scale models to connect lower level phenomena with the perceptual response.

- Model parameters were carefully tuned based on physiological and anatomical data. In this manner, we ensure that our models are reliable and perfectly suited for applications that require a high level of biological realism, such as the study of visual diseases.

- Following the idea of generalization of the modeling presented above, we exhaustively benchmarked our models against a large set of different visual stimuli, showing that the model responses were in agreement with the responses observed in the laboratory for all types of stimuli.

- The software was designed for easy use and to be interfaced with other well-established simulation tools used by the Neuroscience community. A resounding success here was the integration of our retina simulation platform within the Neurorobotics Platform of the HBP.

1.3 Publications

We have published 5 journal articles during the thesis research period. In three of them, the PhD candidate is the first author.

- Mobarhan, M. H., Halnes, G., Martínez-Cañada P., Hafting, T., Fyhn, M., & Einevoll, G. T. (2018). **Firing-Rate Based Network Modeling of the dLGN Circuit: Effects of Cortical Feedback on Spatiotemporal Response Properties of Relay Cells**. PLoS Computational Biology, accepted for publication.

- Martínez-Cañada P., Mobarhan, M. H., Halnes, G., Fyhn, M., Morillas, C., Pelayo, F., & Einevoll, G. T. (2018). **Biophysical network modeling of the dLGN circuit: Effects of cortical feedback on spatial response properties of relay cells**. PLoS Computational Biology, 14(1).

- Martínez-Cañada P., Morillas, C., Plesser, H. E., Romero, S., & Pelayo, F. (2017). **Genetic algorithm for optimization of models of the early stages in the visual system**. Neurocomputing, 250.

- Falotico, E., Vannucci, L., Ambrosano, A., Albanese, U., Ulbrich, S., Vasquez Tieck, J. C., Hinkel, G., Kaiser, J., Peric, I., Denninger, O., Cauli, N., Kirtay, M., Roennau, A., Klinker, G., Von Arnim, A., Guyot, L., Peppicelli, D., Martínez-Cañada, P., Ros, E., Maier, P., Weber, S., Huber, M., Plecher, D., Röhrbein, F., Deser, S., Roitberg, A., van der Smagt, P., Dillman, R., Levi, P., Laschi, C., Knoll, A. C., & Gewaltig, M. O. (2017). **Connecting artificial brains to robots in a comprehensive simulation framework: The neurorobotics platform**. Frontiers in Neurorobotics, 11.

- Martínez-Cañada P., Morillas, C., Pino, B., Ros, E., & Pelayo, F. (2016). **A computational framework for realistic retina modeling**. International Journal of Neural Systems, 26(07).

Another 2 journal articles have been submitted for publication.

- Martínez-Cañada P., Morillas, C., & Pelayo, F. (2018). **A Neuronal Network Model of the Primate Visual System: Coding of Color Surfaces**. Journal of Computational Neuroscience. Submitted for publication.
- Martínez-Cañada P., Morillas, C., & Pelayo, F. (2017). **A Neuronal Network Model of the Primate Visual System: Color Mechanisms in the Retina, LGN and V1**. International Journal of Neural Systems. Submitted for publication.

And there are 5 conference papers.

- Martínez-Cañada P., Morillas, C., & Pelayo, F. (2017, June). **A Conductance-Based Neuronal Network Model for Color Coding in the Primate Foveal Retina**. In International Work-Conference on the Interplay Between Natural and Artificial Computation (pp. 63-74). Springer, Cham.
- Ambrosano, A., Vannucci, L., Albanese, U., Kirtay, M., Falotico, E., Martínez-Cañada, P., Hinkel, G., Kaiser, J., Ulbrich, S., Levi, P., Morillas, C., Knoll, A., Gewaltig, M. O., & Laschi, C. (2016, July). **Retina color-opponency based pursuit implemented through spiking neural networks in the neurorobotics platform**. In Conference on Biomimetic and Biohybrid Systems (pp. 16-27). Springer, Cham.
- Martínez-Cañada P., Morillas, C., Romero, S., & Pelayo, F. (2015, June). **Modeling Retina Adaptation with Multiobjective Parameter Fitting**. In International Work-Conference on Artificial Neural Networks (pp. 175-184). Springer, Cham.
- Martínez-Cañada P., Morillas, C., Pino, B., & Pelayo, F. (2015, June). **Towards a generic simulation tool of retina models**. In International Work-Conference on the Interplay Between Natural and Artificial Computation (pp. 47-57). Springer, Cham.
- Martínez-Cañada P., Morillas, C., Nieves, J. L., Pino, B., & Pelayo, F. (2015, March). **First Stage of a Human Visual System Simulator: The Retina**. In International Workshop on Computational Color Imaging (pp. 118-127). Springer, Cham.

Chapter 2

Introducción

2.1 Motivación y objetivos

Esta tesis queda englobada en el campo de la Neurociencia Computacional. La Neurociencia Computacional comprende el estudio de la función del cerebro en términos de las propiedades del procesamiento de la información y de la arquitectura de red que compone el sistema nervioso. Se trata de una ciencia interdisciplinar que conecta diversos campos de investigación como son la Neurociencia, las Ciencias Cognitivas y la Psicología con la Ingeniería Eléctrica, las Ciencias de la Computación, las Matemáticas y la Física. La Neurociencia Computacional se encuentra actualmente en el epicentro de uno de los proyectos europeos más importantes, el proyecto H2020 "Human Brain Project" (HBP), del cual nuestro grupo de investigación forma parte. Parte del trabajo que aquí se presenta se centra en el HBP.

El modelado computacional y matemático ha desempeñado un papel crucial para entender la funcionalidad de los sistemas visual, auditivo y olfativo, así como la base neuronal de los mecanismos de aprendizaje y de la memoria [Min18]. Existen modelos computacionales de otros tipos de sistemas físicos (e.g., los sistemas planetarios). Sin embargo, las estructuras biológicas del sistema nervioso se pueden considerar como procesadores de información por lo que los modelos computacionales de estos sistemas no son sólo herramientas para el cálculo o la predicción, sino también para inferir su funcionalidad.

Para extraer la funcionalidad del sistema nervioso, es esencial explicar cómo surgen los fenómenos de cada nivel en base a los fenómenos de niveles inferiores (e.g., cómo la actividad neuronal de las células en corteza visual da lugar a la percepción del color). Desafortunadamente, los métodos experimentales a menudo no proporcionan los datos necesarios para ello. Los arrays de electrodos, por ejemplo, proporcionan acceso extracelular sólo a unos cientos de neuronas en el mejor de los casos. El modelado computacional permite acortar las distancias entre los datos experimentales incompletos y la posibilidad de generar una descripción funcional coherente y cuantitativa del cerebro. El modelado computacional nos permite desarrollar modelos de gran escala, basados en datos obtenidos en el laboratorio, y realizar múltiples simulaciones en diferentes situaciones para obtener un mayor conocimiento de cómo funcionan las redes correspondientes del cerebro.

De especial interés han sido los modelos computacionales del sistema visual. El sistema visual ha atraído la atención de muchos científicos a lo largo de los últimos sesenta años, desde el influyente trabajo de Hubel y Wiesel [HW62, HW59], que marcó un referente en la investigación de cómo se organizan las neuronas del cerebro para producir la percepción visual. La visión es una modalidad sensorial fundamental en primates, como nosotros, y la complejidad del sistema visual se refleja en la gran extensión de corteza cerebral que se dedica al análisis de la información visual [KVE92]. Entender el funcionamiento del sistema visual es un tema fascinante no sólo por el conocimiento que podamos llegar a alcanzar de los mecanismos de percepción visual, sino también por su relevancia para otras funciones corticales, incluyendo el procesamiento cognitivo.

Se han propuesto un gran número de modelos para explicar las propiedades del procesamiento visual. Uno de los pioneros en este campo, y quizás el modelo matemático más conocido en Neurociencia de la Visión, es la Diferencia de Gaussianas (DoG, del inglés) introducida en 1965 por R.W. Rodieck [Rod65]. Los modelos descriptivos, como la DoG, han sido esenciales para entender cómo las neuronas convierten los estímulos visuales en una respuesta neuronal. Con los avances recientes en las técnicas de "neuroimagen", la disponibilidad de un volumen cada vez mayor de datos fisiológicos y las capacidades computacionales actuales, disponemos de recursos más que suficientes para desarrollar modelos del cerebro que sean biológicamente más realistas.

Esta Tesis ha estado enfocada principalmente en el desarrollo de modelos computacionales de las primeras etapas del sistema visual que puedan proporcionar herramientas novedosas y de utilidad para la comunidad Neurocientífica. En términos generales, nos marcamos los siguientes objetivos:

- Generalizar los fundamentos computacionales del procesamiento visual, en vez de ajustar la respuesta del modelo a una única observación experimental. Aunque muchos de los modelos de visión propuestos comparten etapas computacionales similares, se ha prestado más interés a ajustar el modelo a datos experimentales específicos en vez de generalizar el modelo más allá de un resultado concreto. Hemos evaluado de forma exhaustiva nuestros modelos usando un gran repertorio de estímulos visuales diversos, para los cuales las respuestas de los modelos estaban dentro del rango de valores experimentalmente medidos para todos los tipos de estímulos. Pensamos que los esfuerzos de investigación deben buscar un marco de modelado general y unificado que facilite la formulación de una descripción coherente del sistema visual.

- Conseguir el mejor compromiso entre la complejidad de los modelos para explicar la funcionalidad y su precisión biológica. De esta forma, los modelos que proponemos son lo más simples posible (e.g., están implementados en base a modelos de neurona unicompartimentales) pero al mismo tiempo son capaces de reproducir la mayoría de las propiedades de la respuesta neuronal. Aunque los modelos han sido simplificados en gran medida, esto no significa que los valores de sus parámetros no se correspondan con valores biológicos. De hecho, es justo lo contrario. Se ha tenido especial cuidado en asegurar que las propiedades morfológicas y fisiológicas de los modelos estén estrictamente basadas en datos experimentales.

- Para que puedan ser validados de forma independiente y se pueda seguir avanzando en su investigación, los modelos han sido implementados usando herramientas de simulación estandarizadas, como lo es NEST [NES18], y todo el código de los proyectos ha sido liberado como software de código abierto [Git18].

2.2 Aportaciones

Los modelos biológicamente realistas presentados en esta Tesis tienen como objetivo último la adquisición de un mayor conocimiento de los mecanismos neuronales subyacentes al procesamiento de la información en las primeras etapas del sistema visual. Una serie de hipótesis planteadas a partir de resultados experimentales han sido evaluadas por medio de simulaciones de los modelos en diferentes y múltiples escenarios. Comparados con otros modelos biológicos de visión, nuestros modelos aportan las siguientes contribuciones:

- Nuestro software puede ser considerado como una herramienta gradual y evolutiva para neurocientíficos que necesiten modelos de gran escala relativamente detallados. La categoría de los modelos de gran escala parece estar poco representada en la literatura. Ilustraremos la importancia de los modelos de gran escala para conectar fenómenos de bajo nivel con respuestas perceptuales.
- Los parámetros de los modelos han sido ajustados de forma minuciosa basándonos en datos fisiológicos y anatómicos. De esta forma, nos aseguramos de que nuestros modelos son fiables y están perfectamente indicados para aplicaciones que requieran un alto nivel de realismo biológico, como es el estudio de enfermedades visuales.
- Siguiendo la idea previamente presentada de generalización del modelado, hemos evaluado exhaustivamente nuestros modelos en base a un gran número de estímulos visuales diferentes, demostrando que las respuestas de los modelos se corresponden con las respuestas observadas en el laboratorio para todos los tipos de estímulos.
- El software ha sido diseñado para un uso sencillo y para ser conectado con otras herramientas de simulación estándar en la comunidad Neurocientífica. Un éxito rotundo en este ámbito ha sido la integración de nuestra plataforma de simulación de modelos de retina con la Plataforma de Neurorobótica del HBP.

2.3 Publicaciones

Se han publicado 5 artículos de revista durante el periodo de investigación de la tesis. En tres de ellos, el estudiante de doctorado es el primer autor.

- Mobarhan, M. H., Halnes, G., Martínez-Cañada P., Hafting, T., Fyhn, M., & Einevoll, G. T. (2018). **Firing-Rate Based Network Modeling of the dLGN Circuit: Effects of Cortical Feedback on Spatiotemporal Response Properties of Relay Cells**. PLoS Computational Biology, accepted for publication.
- Martínez-Cañada P., Mobarhan, M. H., Halnes, G., Fyhn, M., Morillas, C., Pelayo, F., & Einevoll, G. T. (2018). **Biophysical network modeling of the dLGN circuit: Effects of cortical feedback on spatial response properties of relay cells**. PLoS Computational Biology, 14(1).

- Martínez-Cañada P., Morillas, C., Plesser, H. E., Romero, S., & Pelayo, F. (2017). **Genetic algorithm for optimization of models of the early stages in the visual system**. Neurocomputing, 250.
- Falotico, E., Vannucci, L., Ambrosano, A., Albanese, U., Ulbrich, S., Vasquez Tieck, J. C., Hinkel, G., Kaiser, J., Peric, I., Denninger, O., Cauli, N., Kirtay, M., Roennau, A., Klinker, G., Von Arnim, A., Guyot, L., Peppicelli, D., Martínez-Cañada, P., Ros, E., Maier, P., Weber, S., Huber, M., Plecher, D., Röhrbein, F., Deser, S., Roitberg, A., van der Smagt, P., Dillman, R., Levi, P., Laschi, C., Knoll, A. C., & Gewaltig, M. O. (2017). **Connecting artificial brains to robots in a comprehensive simulation framework: The neurorobotics platform**. Frontiers in Neurorobotics, 11.
- Martínez-Cañada P., Morillas, C., Pino, B., Ros, E., & Pelayo, F. (2016). **A computational framework for realistic retina modeling**. International Journal of Neural Systems, 26(07).

Otros 2 artículos de revista han sido enviados para su publicación.

- Martínez-Cañada P., Morillas, C., & Pelayo, F. (2018). **A Neuronal Network Model of the Primate Visual System: Coding of Color Surfaces**. Journal of Computational Neuroscience. Submitted for publication.
- Martínez-Cañada P., Morillas, C., & Pelayo, F. (2017). **A Neuronal Network Model of the Primate Visual System: Color Mechanisms in the Retina, LGN and V1**. International Journal of Neural Systems. Submitted for publication.

Y hay 5 artículos de conferencias.

- Martínez-Cañada P., Morillas, C., & Pelayo, F. (2017, June). **A Conductance-Based Neuronal Network Model for Color Coding in the Primate Foveal Retina**. In International Work-Conference on the Interplay Between Natural and Artificial Computation (pp. 63-74). Springer, Cham.
- Ambrosano, A., Vannucci, L., Albanese, U., Kirtay, M., Falotico, E., Martínez-Cañada, P., Hinkel, G., Kaiser, J., Ulbrich, S., Levi, P., Morillas, C., Knoll, A., Gewaltig, M. O., & Laschi, C. (2016, July). **Retina color-opponency based pursuit implemented through spiking neural networks in the neurorobotics platform**. In Conference on Biomimetic and Biohybrid Systems (pp. 16-27). Springer, Cham.

- Martínez-Cañada P., Morillas, C., Romero, S., & Pelayo, F. (2015, June). **Modeling Retina Adaptation with Multiobjective Parameter Fitting**. In International Work-Conference on Artificial Neural Networks (pp. 175-184). Springer, Cham.
- Martínez-Cañada P., Morillas, C., Pino, B., & Pelayo, F. (2015, June). **Towards a generic simulation tool of retina models**. In International Work-Conference on the Interplay Between Natural and Artificial Computation (pp. 47-57). Springer, Cham.
- Martínez-Cañada P., Morillas, C., Nieves, J. L., Pino, B., & Pelayo, F. (2015, March). **First Stage of a Human Visual System Simulator: The Retina**. In International Workshop on Computational Color Imaging (pp. 118-127). Springer, Cham.

Chapter 3

Contextualization of the work

In Section 3.1 we provide an overview of the morphological organization of the retina, LGN and V1, and the essential properties of the spatiotemporal dynamics of the different cell classes. The focus is on the processing pathways and neuronal structures that are present in our computational models (e.g., the rod pathway is not included). We hope that this overview can help non-specialist readers to become familiarized with the theoretical framework used to formulate vision models. For a more detailed explanation, please refer to the following references: for the retina, the web page "Webvision" [KFN18], the reviews of the primate retina by Lee and coauthors [LMG10] and Dacey [Dac00], and the reviews of the mammalian retina by Masland [Mas12, Mas01]; for the LGN, the well-known book by Sherman and Guillery [SG01], the overview by Usrey and Alitto [UA15] and the most relevant reviews describing the corticothalamic function [AU03, SJ02]; for V1, our focus is on color coding (studies by Shapley and Johnson [SH11, JHS01]) and the functional organization of the primate cortex (studies by Callaway [Cal98]).

Section 3.2 presents the literature review on the previous biological models developed for each of the stages in the early visual pathway. There is a substantial number of models that have been proposed over the last few decades and it is out of the scope of this thesis to include all. Here we primarily focus on those models that have served as a reference for our work.

3.1 General anatomy and function of the early visual system

3.1.1 Parallel pathways in the retina

The retina is a multilayered structure in all mammals. The neural architecture of the retina can be seen as a three-neuron vertical pathway (see Figure 3.1 A) composed of excitatory cells: 1) photoreceptors (cones and rods) that transform the light stimulus into a neural signal, 2) bipolar cells (BCs) that relay the photoreceptor signals to 3) ganglion cells (GCs), the output neurons of the retina [Dac00]. Added to this pathway, there are two inhibitory pathways, whose cells' activity spreads horizontally. It is formed by horizontal cells (HCs) that modify the transfer at the photoreceptor-bipolar-cell synapse and the amacrine cells (ACs), modulating the synapse between BCs and GCs. The interplay between excitatory and inhibitory pathways is the origin of the fundamental center-surround antagonistic receptive field characteristic of retinal cells. Receptive fields of BCs already show this center-surround antagonistic structure [DPD⁺00]. The circularly symmetric center-surround mechanism at the bipolar-cell stage is created by combination of signals from HCs and cones that are opposite in sign and have different horizontal extents (Figure 3.1 B).

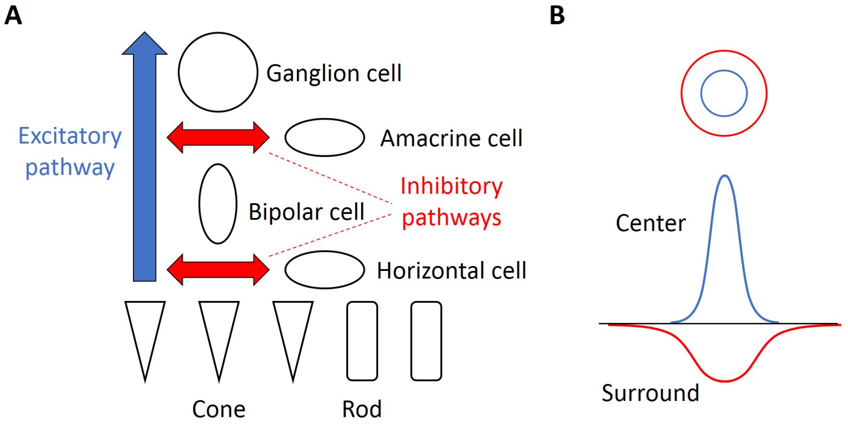

Figure 3.1: A: Neuron populations of the retina and representation of the vertical excitatory pathway and the horizontal inhibitory pathways. B: Top view and spatial profile of the schematized center-surround organization of the receptive field of an ON-center BC, where a narrow excitatory center is surrounded by a wider inhibitory surround.

The neural code for trichromatic color vision in primates begins with the sampling of visual stimuli by the three cone photoreceptor types, sensitive to long (L cones), middle (M cones), or short (S cones) wavelengths. Cone signals are subsequently transformed into spectrally opponent responses through two different parallel processing streams in the retina, commonly known as red-green and blue-yellow pathways, or parvocellular and koniocellular pathways [Dac00]. A third pathway, the magnocellular pathway, is not spectrally opponent but shows a broad spectral sensitivity created by additive input from L and M cones. Each pathway is associated with distinctive retinal architectures.

The vertical pathway of the red-green opponent pathway is well-established, consisting of L and M cones, midget BCs and midget GCs. Midget GCs are small and has a compact dendritic arbor [Cal05]. In the fovea, there is a one-to-one relationship between cones to midget BCs, which receive input from a single cone type, L or M type, and between midget BCs to midget GCs. Horizontal connections in the parvocellular pathway are formed by H1 HCs and different types of ACs. Anatomically, it has been seen that H1 HCs receive indiscriminate input from an extended region of L and M cones and do not transmit an S-cone signal [Dac00]. Midget BCs react to visual stimuli with two different responses, ON-center and OFF-center responses [SKSN08, NJ90]. ON-center BCs depolarize with light increments while OFF-center BCs depolarize when the intensity of the stimulus is reduced. The center and surround mechanisms of the parvocellular receptive fields are approximately linear and show low contrast sensitivity. It has been proposed that parvocellular cells are used for the analysis of form, texture, and color [KB01].

The blue-yellow pathway in the retina is transmitted to higher visual areas via a less common type of GC, the small bistratified GC. The substrate of the mechanisms of the blue-ON pathway is better known than that of the blue-OFF pathway. Blue-ON GCs receive parallel ON-depolarizing and OFF-hyperpolarizing inputs from S-cones and combined L- and M-cones, respectively [CDP$^+$09, Dac00]. Interestingly, the receptive field of the small bistratified GC is spatially coextensive, i.e., it has nearly spatially matched ON and OFF fields that only differ in spectral tuning. The synaptic mechanisms that create the cone opponency in the yellow-blue pathway remain controversial. One hypothesis is that the opponent S-ON and LM-OFF responses of the ganglion-cell receptive field originate from the excitatory receptive field centers of S-ON and LM-OFF cone BCs [CDP$^+$09].

The magnocellular pathway is formed by diffuse BCs and parasol GCs, which have a much larger cell body and dendritic arbor than midget cells [Cal05]. The receptive-field center of parasol cells near the fovea receives random sampling from about 6-8 cones [LMG10]. These inputs are primarily seen to be additive inputs from L- and

M-cones. The magnocellular-cell response is largely achromatic and more transient (or phasic) than the response of parvocellular cells. The temporal responses of magnocellular cells are nonlinear, and with increasing contrast they show the effects of a contrast gain control [KB01]. The contrast gain of cells in the magnocellular layers is about 10 times higher than that of the cells in the parvocellular layers. It is suggested that these cells are involved in motion analysis.

The parallel pathways in the cat are organized in many critical ways like those of the primate [She79]. There are different proposals for grouping primate GCs in a correspondence with cat GCs. One idea is that parvocellular cells in the primate are functionally similar to X cells in the cat, and magnocellular cells are similar to Y cells. However, some authors argue that the parvocellular type has no exact functional equivalent in the cat and magnocellular cells are actually composed of two subgroups which correspond to X and Y cells [Bra92]. The most accurate correspondence seems to be at the morphological level. Parvocellular cells are considered to be equivalent to β cells of cat. Magnocellular cells, on the other hand, are probably equivalent to α cells of cat [KFN18].

3.1.2 Lateral geniculate nucleus

Visual signals from the retina pass through the LGN of the dorsal thalamus, the visual part of thalamus, on the way to the visual cortex [UA15]. The LGN contains two types of cells: a excitatory class, the relay cell (RC), and a local inhibitory interneuron (IN). GCs provide the feedforward input to the LGN circuit. In primate, there are about as many RCs as GCs and there is nearly a one-to-one anatomical mapping from GCs to RCs [HWSM15, SKAT96]. In cat, there are approximately twice as many RCs as GCs [MMMW+14].

Inhibition in the LGN is mediated by INs, which synapse both on RCs, incorporating typically both axonal and triadic inhibition [HWSM15] (Figure 3.2), and other INs. In macaque monkeys, though, triads appear to be common in the magnocellular layers and much rarer in the parvocellular layers [Kre05]. Local INs are not the only elements involved in the role of inhibition in the thalamus: the GABAergic neurons of the reticular nucleus also project to the dorsal thalamic nuclei in all mammalian species. However, the role of the reticular nucleus in the processing of visual information is under debate. It has been hypothesized that the function of the reticular nucleus becomes more focused on the regulation of the sleep-waking cycle, acting as an internal thalamic pacemaker, rather than on direct inhibition of RCs [AFR+97].

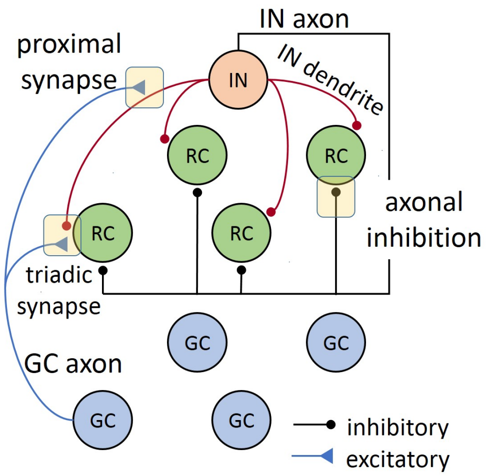

Figure 3.2: Feedforward inputs to LGN cells, RCs and INs, and local inhibitory connections. INs receive input from GCs via the triadic synapse and the proximal interneuron dendrite. RCs are contacted by the IN axon, receiving axonal inhibition, and by the IN dendrite at the triadic synapse, resulting in direct triadic inhibition. Figure adapted from `https://doi.org/10.1371/journal.pcbi.1005930.g001`.

In the cat, the receptive-field center of RCs is driven by excitation of GCs of the same sign (ON or OFF) and the surround apparently emerges through inhibition of INs that receive input from GCs of the opposite sign [HWSM15, WVS$^+$11]. Although there are some recordings of INs in the parvocellular laminae having center responses that are of the opposite sign of the RCs around them [Wil89], evidence suggests that same-sign inhibition of RCs is rather the general trend in the primate: first, ON and OFF cells, both RCs and INs, remain functionally separated at the level of the LGN [Wil89, Mic88]; second, axons of INs often ramify locally within the boundaries of the thalamic nucleus of origin [ZUL99, AFR$^+$97].

A fascinating feature of the LGN circuit is the prominent feedback received from cells in layer 6 of visual cortex, which extends significantly beyond the classical receptive field of RCs, and it has influence on the firing pattern, synchronization and sensory response mode of RCs [AU03, SJ02]. Perhaps, the most studied effect of cortical feedback is the increase of the center-surround antagonism of thalamic receptive fields, i.e., the suppression of the response to very large stimuli compared to smaller, more optimal stimuli [JAA$^+$12, SJ02, SCM93]. In this manner, cortical feedback may be understood as a mechanism that dynamically sharpens the spatial focus of the receptive field and increases its spatial resolution. A stronger enhancement of the strength of the inhibitory surround has been observed in the presence of moving stimuli, rather than flashing spots [SJ02].

3.1.3 Primary visual cortex: local circuitry and color mechanisms

The geniculate inputs from parvocellular and magnocellular cells in the LGN are segregated in the primary visual cortex. Parvocellular cells project to layer 4Cβ and the upper part of layer 6, whereas magnocellular innervate layer 4Cα and the lower part of layer 6 [SH05] (Figure 3.3). The third pathway, formed by koniocellular cells, provides direct geniculate input to superficial layers (layers 2-3). There is an additional connection, to layer 4A, although the innervation of this layer is uncertain. Interestingly, this connectivity scheme, with stream-specific feedforward projections to V1, seems to be replicated for the corticothalamic feedback connections. Recent studies have demonstrated that neurons in the upper part of layer 6, which receive thalamocortical connections from parvocellular LGN cells, project exclusively to the parvocellular LGN layers [BU11]. Neurons in the lower part of layer 6 (the target of magnocellular LGN cells) project primarily to the magnocellular layers and perhaps the koniocellular layers.

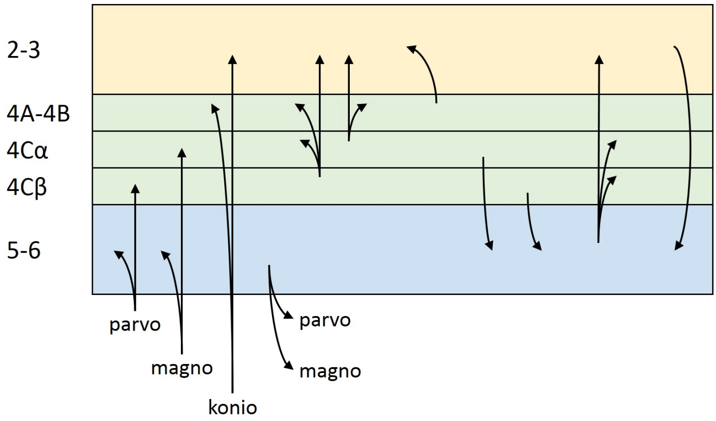

Figure 3.3: Simplified representation of the multilayered structure of V1 and the main connectivity patterns: thalamocortical connections from parvocellular, magnocellular and koniocellular layers, vertical interlaminar connections and corticothalamic connections from layer 6 cells to parvocellular and magnocellular cells. For the sake of clarity, horizontal intralaminar connections in V1 are not shown.

This neat segregation of thalamocortical and corticothalamic connections has motivated some researchers to propose a functional organization of V1 where the analysis of visual attributes of color, form, and motion remain separate and independent [LH88, Zek78]. However, recent anatomical and functional studies imply that magnocellular, parvocellular, and koniocellular pathways intermingle extensively within V1, supporting a more integrated view in which the processing of color, form and motion is multiplexed in cortical signals [SH11, SH05, FZH03, LTL^{+}95].

Over the past few decades, much progress has been made in unraveling a detailed understanding of the organization of intracortical connections. Understanding the precise connectivity patterns between neurons is complicated because of the multiple neuron types that are found within a cortical layer and the different sources of inputs. Here we present a simplified view of the main vertical interlaminar connections (Figure 3.3). Spiny stellate cells of layer 4Cβ project to layers 2-3, where about half their synaptic connections are made [CW96]. They also make numerous synapses in layers 4Cα, and 4A-4B. Cells in layer 4Cα project to all superficial layers and to layer 4A-4B. Although layers 4Cβ and 4Cα project axons primarily to superficial layers, they also have weaker connections with layer 5-6 [Cal98]. In the second stage of intracortical projections, infra- and supragranular layers make recurrent connections. Layers 2-3 provide a connection to layers 5-6. Layer 5-6 neurons, in turn, provide feedback projections to layers 2-3 and layers 4Cβ and 4Cα.

There exist numerous classification schemes of the different cell types found in visual cortex, which vary depending on the properties of cells that are evaluated, e.g., their morphology. Since our focus is on color coding in V1, we will use the classification proposed by Johnson and Shapley [JHS01], based on the ratio of the neurons' peak responses to luminance and equiluminant gratings. The population of cortical cells is divided into three groups: luminance-preferring (LP), color-luminance (CL) and color-preferring (CP) cells. LP cells show a minimal response to equiluminant gratings, but respond well to luminance patterns, CL cells are spatially tuned for equiluminant and also for luminance patterns and CP cells give large responses to equiluminant gratings and little response to luminance gratings. LP cells are roughly 60 % of the total amount of cortical cells, CL cells are 30 % and CP cells are 10 % [SH11, JHS01]. Most LP and CL cells have oriented receptive fields with odd-symmetry: receptive fields formed by two adjacent elongated subregions, ON and OFF, of similar weights. Most CL cells were seen, in fact, to correspond with double-opponent cells [SH11]. Double-opponent cells respond strongly to color patterns and edges, but respond poorly to extended areas of color, or to color patterns of low spatial frequency. The last group, CP cells, is not orientation selective and has subregions that are approximately circular in shape and concentric.

3.2 Previous modeling studies

3.2.1 Types of models used in Computational Neuroscience

Computational Neuroscience provides tools and methods for “characterizing *what* nervous systems do, determining *how* they function, and understanding *why* they operate in particular ways” [DA01]. The answers to each of these questions will give us the different levels of modeling employed in Computational Neuroscience:

- **Descriptive models (*what*)**: specify the transform between the input and the output of the neural system. In the visual system, these models often correspond to convolution and linear filters. They may be based loosely on biophysical, anatomical, and physiological findings, but their primary purpose is to describe phenomena not to explain them.
- **Mechanistic models (*how*)**: describe the lower-level mechanisms used by the neural system to produce a specific response on the basis of known anatomy, physiology, and circuitry.
- **Interpretive models (*why*)**: use computational and information-theoretic principles to investigate the behavioral and cognitive significance of various aspects of a nervous system function.

The models implemented in this work fall into the categories of descriptive and mechanistic models, which will be the focus of the review presented below. Our models are multi-stage models developed with the aim of understanding the properties of some specific visual phenomena. Those stages of the model that play a major role in describing the mechanisms of the target visual phenomena were implemented as mechanistic models. The remaining stages, less relevant, were defined as descriptive models. This is a common strategy used in other large-scale models of the visual system (e.g., the retina input of LGN models is often implemented as a descriptive filter [HHHE16, HT05]).

3.2.2 Models of the retina

The retina is certainly the visual stage that has received most attention from scientists, with numerous models, ranking from detailed models that target a specific physiological property [KMB11, vH05, KR03, SPLD01, BIBJM99, FM97] to large-scale models of the whole retina [WK09, POR09, MRM$^+$07, HW07, HFW02, Hér96, DVDV93].

Most models use linear filters to approximate signal transformations that occur in the successive layers of the retina. The typical example is the first-order low-pass temporal filter employed to simulate synaptic delays and membrane integration of synaptic currents [WK09, vH05]. Multiple distributed low-pass stages occur along the retinal pathway. Moreover, some single cells already integrate several low-pass filters. An example is the phototransduction cascade at photoreceptors, which roughly includes three processing stages: the outer segment transduction cascade, inner segment ion channel interactions and interactions in the cone pedicle [vH05].

The other commonly used linear filter is the Gaussian filter [WK09, BIBJM99], a low-pass spatial filter. Since the early studies of the cat retinal GCs by Enroth-Cugell [ECR66], the Gaussian filter has become the model of the retinal receptive field par excellence. Sensitivity of the antagonistic center-surround receptive field of GCs is often described by difference of two Gaussian kernels (DoG) with different space constants. At single-cell level, a Gaussian kernel is used to approximate the biophysics of spatial synaptic integration through dendrites of retinal cells and also electrical couplings between neighboring cells. The computational operation underlying these biological mechanisms can be interpreted in terms of a spatial averaging of the neural signal.

Some models include more sophisticated mechanisms to describe nonlinear dynamics of retinal cells. A contrast gain control is used to capture the influence of the local contrast of visual stimuli on the transfer properties of the retina [WK09, BIBJM99]. In these models, if the stimulus provides strong excitation for an extended period of time, a negative feedback loop reduces the gain at the input and consequently the response to subsequent stimulation. Other models were also cascaded with negative feedback loops to adjust the photoreceptors' dynamics to the steady illumination level [vH05]. Another type of functions, static nonlinearities, is used to introduce some important signal corrections performed by neurons (e.g. thresholds and saturation). These functions typically perform polynomial, rectification or sigmoidal transformations of the neural signal [WK09].

Realistic biophysical models, closer to the mechanistic approach, employ networks of passive point neurons [HW07, HFW02] or conductance-based neurons with a minimal set of ion currents [POR09]. The dynamics of GCs are often modeled with single-compartment models that include a full repertoire of ion currents [KMB11, FM97] or by means of the Hodgkin-Huxley formalism [KR03].

3.2.3 Models of the lateral geniculate nucleus

The DoG model has also been widely used to describe receptive fields of RCs in dorsal lateral geniculate nucleus [KMS79]. This simple descriptive model was extended to include information about the neuronal circuitry of the LGN, incorporating feedforward inhibition from intrageniculate INs [EH00] and cortical feedback [EP12, PE02]. The extended DoG model was employed to study effects of cortical feedback on relay-cell responses to flashing circular spots and patch-grating stimuli. Other projects have also investigated feedback effects on the spatial response [HT01] and the temporal processing of RCs [NWNE12, YD07, KG98, WNLF98, KW96].

To gain a deeper understanding of the transmission of visual signals from retina to the LGN, some authors have proposed simplified models of the relay-cell response [CHXK08, CHS07]. With these models, it is demonstrated that postsynaptic summation is sufficient to predict the geniculate spike trains under certain conditions, ruling out a major role for presynaptic mechanisms such as synaptic facilitation. A different model of the relay-cell response was developed to capture both tonic and burst firing modes of RCs [SCSR00]. It was later extended, in a minimal thalamic model that also included a reticular neuron, to explain the distinctive properties of thalamic bursting as an effective relay mode [Bab05].

The opposite extreme, in terms of biological detail, is the model by Heiberg and coworkers [HHHE16]. The model includes a biophysically detailed multicompartmental model of an IN [HAH$^+$11] interconnected with five single-compartment RCs. This work investigated the effects of the different inhibitory actions of INs, i.e., triadic inhibition and standard axonal inhibition, on the response properties of RCs. A model based on single-compartment Hodgkin-Huxley neurons was used to implement a realistic hybrid retino-thalamo-cortical pathway mixing biological cells and simulated circuits [BDG$^+$13]. The study in [BUL03] incorporated multicompartmental thalamic cell models to investigate passive properties of LGN cells. Destexhe and coworkers [DCS98, DNUH98] also employed biophysically detailed model neurons in their well-known series of studies of the synchronized oscillations in the thalamus and in the thalamocortical system.

Last but not least, it is worth mentioning the two well-known large-scale models of the mammalian thalamocortical system that were proposed to explain spontaneous activity and the emergence of propagating waves and rhythms (e.g., sleep slow waves) on different scales [IE08, HT05].

3.2.4 Models of the primary visual cortex

The model of V1 presented in this thesis aligns with the network models of macaque primary visual cortex developed by Shapley's research team [CSY16, ZXSS10, TSMS04, MSS03, MSSW00] in terms of the type of neuron model used, integrate-and-fire (IF) conductance-based point neuron, and the care given to choose parameter values that are strictly based on experimental data. These models investigate orientation selectivity and dynamics in layer 4Cα and how recurrent cortical connections cause the network to sharpen its selectivity. Another interesting question these models aim to clarify is how orientation selectivity can emerge from very sparse LGN inputs. Besides the models of the thalamocortical system [IE08, HT05] cited before, another important large-scale spiking network model of V1 that integrates a large body of experimental data is the recent model by Potjans and Diesmann [PD12]. However, none of these latter models are based on data from the primate. We have observed that the major limiting factor that continue to hinder the development of biophysical models of the primate visual system is the scarcity of physiological data from this species.

With the exception of the remarkable modeling work by De Valois and De Valois [DVDV93], there are simply few biological models of color processing specifically tuned to the primate primary visual cortex [SE02, Bil95]. We found, though, some models with application in image processing and computer vision that implement single- and double-opponent receptive fields of color-responsive cells [WS16, GYLL15, YGLL13, GYLL13]. In this context, we can conclude that our cortical model provides an excellent opportunity to gain insights into the principles of color processing in V1.

Chapter 4

Methods

In this Chapter, we overview the different software tools that have been employed for model simulations, methods for automated parameter search and the parallel processing architecture used to accelerate computations. We particularly aim to justify the suitability of every chosen method for our work. We start by reviewing the different simulators and simulation environments used for spiking neurons in Section 4.1. We next review the implementation of our own retina simulation software in Section 4.2. Section 4.3 summarizes the optimization strategy followed for automated model tuning. Finally, the scheme developed for distributed computing in a cluster is described in Section 4.4.

4.1 Simulators of neurons and networks of neurons

Over the last 20 years a growing number of tools have appeared that allow simulations at different scales, from very detailed biophysical representations of individual neurons to large-scale spiking neural networks. Such tools facilitate precise simulations of a given computational paradigm, as well as publishable results in a relatively short amount of time [BRC$^+$07]. These simulation environments have also standardized the definition and documentation of models, making the code more shareable and favoring independent validation by a wider scientific community.

For large-scale network simulations, one does not need to realistically capture the spike generating mechanisms and the effects of ion channels on the neural response, and simpler models, such as the integrate-and-fire (IF) model, are sufficient. This is the paradigm used by NEST [GD07], one of the most popular simulators of large networks of point neurons or neurons with a small number of compartments. NEST has allowed researchers to simulate about 10 % of the human cortex at a resolution of individual neurons and synapses on contemporary supercomputers [JIH$^+$18]. NEST is an open-source simulation platform in widespread use by the neuroscientific community and a core simulator of the Human Brain Project.

We used NEST to implement the whole structure of the model of the primate visual system [MCMP18, MCMP17a]. We evaluated two different conductance-based neuron models, both with synaptic alpha functions. To explain the formation of receptive fields in layer 4Cβ in V1 [MCMP17a], a simple conductance-based IF model (*iaf_cond_alpha*) was sufficient. For the second version of the primate network model [MCMP18], we found that more complex phenomena such as wave propagation in V1 required incorporating additional mechanisms to the neuron dynamics. In this scenario, we employed the adaptive exponential IF model (*aeif_cond_alpha*), which does not increase significantly the complexity of simulation and captures the complex intrinsic properties seen in neurons of the LGN and V1, such as low-threshold spike, regular spiking or fast-spiking [BG05]. Connectivity of the network was implemented by using the Topology Module included in NEST [PE10]. The Topology Module is an interface for creating complex layers of neurons with spatial structure, perfectly suited for modeling the spatial arrangement of the different stages in the early visual system.

At the other end of the spectrum, there exist simulation environments, such as GENESIS [BB12] and NEURON [HC97], which provide the tools for biologically realistic modeling of individual neurons and small networks of neurons. NEURON is, perhaps, the most widely used simulator and it was our choice to develop the model of the dLGN that receives cortical feedback [MCMH$^+$18]. With NEURON, we defined a relatively small network of single-compartment and multicompartment neuron models that represent RCs and INs in the dLGN and a population of orientation-selective layer 6 pyramidal cells. We opted for this type of simulator, instead of NEST, because we were not only interested in studying the network effects of cortical feedback but also in exploration of the lower-level mechanisms behind the effects observed for cortical feedback. With this type of modeling we could analyze the excerpts of membrane potentials for various cells in the circuit and for the different compartments of the IN model, i.e., soma and dendrites, and visualize the sequence of subthreshold events that lead to extra action potentials or suppression of action potentials being fired by RCs.

We also employed the Python package LFPy [LHL$^+$14] for object representations of individual cells. LFPy provides a set of easy-to-use classes for defining cells, synapses and recording electrodes as Python objects. It relies on the NEURON simulation environment to solve the membrane potentials of cells.

4.2 Implementing our own retina simulator

During the ramp-up phase of the HBP, the main task of our research group was to develop a simulation environment where different retina models could be evaluated and that could be interfaced with the Neurorobotics platform, serving as the sensory input of models of higher visual areas. After an extensive review of literature, we found a limited number of software tools that give us the possibility to configure different retina models (e.g., Virtual Retina [WK09]). However, these tools often include ad hoc models whose parameters can be modified but not their retina architecture. Generally, their primary goal is to fit some properties of the retina processing, though, none of them can be fully configured to reproduce different physiological results than those that have been intentionally designed for.

Neural simulators, such as NEST or NEURON, exploit common properties of neurons (e.g. their ionic-selective channels) to provide researchers with a general and unified framework for neural modeling. Following this idea, we made a selection of those algorithms that had been recurrently used in the literature to describe some properties of the retina processing. We implemented a configurable simulator, COREM, that gives the opportunity of using these computational units as basic building blocks to construct different retina models [MCMP$^+$16]. This configurable C++ retina simulation software aims to provide scientists with a rapid prototyping tool for retina modeling, which facilitates the study of low-level visual mechanisms, and to optimize efficiency of all its modules.

Computations of spatiotemporal equations performed by retinal microcircuits are formulated as recursive filters. We also employ OpenMP to gain thread-level parallelism in the Gaussian filter. Unlike a conventional neural simulator, layers of neurons in the retina are handled as images (using CImg library [Tsc12]), with all the benefits that this entails, such as simultaneous access to internal variables of multiple neurons in a SIMD processor. The modular structure of COREM allows for more flexibility of use than other retina simulators. The user can create and connect any number of computational retinal microcircuits by configuring a simulation script that follows a similar syntactic structure of a typical neural-simulator script. Moreover, built-in tools for visual stimulation and data analysis give the possibility to reproduce some of the most common experimental setups used in electrophysiology of the retina (e.g. sinusoidal drifting gratings or uniform white flashes). Integration with models of higher visual areas is easily carried out by simply instantiating COREM as an extension module in the script used for simulation in NEST.

4.3 Genetic algorithm for optimization of model parameters

Neuron models often have multiple parameters and a great number of them are difficult to extract from experimental measures. Additionally, the model response depends often on several parameters and it is complicated to tune manually all of them to fit some physiological response. Parameter optimization is facilitated by automated search methods that minimize an error metric representing differences between simulated and experimental data [VGDSA08]. Traditionally, models of the early visual pathways are either hand-tuned, using a trial-and-error method, or defined in terms of the well-known linear-nonlinear (LN) modeling [WK09, YD07, BÖMM08, HT01]. Although we can also find other models whose parameters are tuned by an optimization algorithm [MÁCCDT+16, CCMÁDT+15, OB12, MBC08, vH05].

In our work [MCMP+17c], we used a genetic algorithm (GA) to facilitate the parameter search of the retina models implemented with COREM and of the large-scale model of the thalamocortical system proposed by Hill and Tononi [HT05]. We chose a GA optimization because of several reasons. A GA is a popular, biologically inspired optimization method that can prevent the search from converging on local minima. In addition, GAs do not need a differentiable mathematical expression, or an estimate, of the objective function, like in gradient methods. Therefore, GAs are more likely to find the global optimum, and require relatively little knowledge of the problem being solved. Although the computation of the fitness function can be time-consuming, the inherently parallel nature of GAs simplifies their implementation on a multiprocessing architecture.

A critical component of the optimization algorithm is the error metric. For the retina models, we were interested in fitting all properties of the temporal response. We have shown that a standard point-by-point comparison of traces (e.g., by using only the mean-squared error, MSE) was insufficient to characterize high-frequency components of the response. We defined a multiobjective fitness function that combines two types of error metrics, the normalized root-mean-square error and a shape error descriptor. We have demonstrated that these new metrics allow the model to capture high-frequency oscillations of the temporal response. Parameters of the large-scale model of the thalamocortical system were fitted by a metric that computes the root-mean-square error between the average and target membrane potentials of the population over given time intervals.

4.4 Distributed computing in a cluster

A single-trial simulation of a large-scale network model is computationally demanding. When we want to search for the optimal set of parameter values or to explore different responses of the model to varying input stimuli, multiple simulations of the model are required and their computations may be unfeasible for a conventional desktop computer. To illustrate this, I will provide the following example. One evaluation of Hill-Tononi's thalamocortical system model by the GA fitness function takes up to 180 s using an Intel Core i7-3630QM CPU. When 512 individuals are evaluated along 100 generations (51200 evaluations in total), the GA optimization would be completed after 2560 h using a single processor. To address this drawback, we developed a parallel processing architecture in a computer cluster based on the MPI interface [GLS99] that distributes model simulations across different processes. For the previous example, the fitness functions of 512 individuals would be computed in parallel, with 512 processes running in 512 CPUs, and the GA would be executed in only 5 h.

Distributed computing allows the use of multiple computers simultaneously and enables larger simulations. One critical aspect of simulations of our models is the memory usage, which can increase up to 10 GB as a result largely of the storage of synaptic connections. We chose an MPI distributed-memory parallelization based on the Python library mpi4py [DPKC11], in which we map every process to one CPU, exploiting most memory resources of every computation node. The two computer clusters employed for this work are the Alhambra supercomputer of the University of Granada [Alh18] and the Stallo supercomputer of the National High Performance Computing Consortium (NOTUR) in Norway [Sta18].

To distribute every simulation to the different computation nodes we used a well-known master-slave configuration whereby a root process evenly splits the number of simulations and scatters them to the rest of processes. All processes then compute in parallel the model responses of the assigned simulations. Once all simulations are completed, the root node gathers results from all processes and store them to hard disk.

Chapter 5

Results

With the exception of Section 5.5, which covers the model of the primate visual system (submitted for publication), the preceding Sections provide an overview of the main results obtained in each publication. Further information can be found in the annexed articles (Appendix A, Appendix B and Appendix C).

5.1 COREM: A configurable retina simulation environment

The software of COREM [MCMP$^+$16] was developed within the context of the HBP. The main task of our research group was to implement a simulation tool where different retina models could be evaluated and that offered an interface with the HBP Neurorobotics platform, so that it could serve as the sensory input of models of other brain areas. Most modeling studies of the retina have been more focused on fitting specific physiological data rather than extrapolating results beyond a particular model. Even those models that show some level of configurability [WK09] are often ad hoc models whose parameters can be modified but not their retina architecture.

On the contrary, neural simulators, such as NEST or NEURON, exploit common properties of neurons (e.g. their ionic-selective channels) to provide researchers with a general and unified framework for neural modeling. Following this idea, we made a selection of those computational algorithms that had been recurrently used in the literature to describe some properties of the retina processing (Figure 5.1). The user can create and connect any number of these computational units to construct different retina models. COREM provides scientists with a rapid prototyping tool for retina modeling where computations of spatiotemporal equations were optimized by means of recursive filtering and multithreading. We also include built-in tools for visual stimulation and data analysis that give the possibility to reproduce some of the most common experimental setups used in electrophysiology of the retina (e.g. sinusoidal drifting gratings or uniform white flashes). Integration with models of higher visual areas is easily carried out by simply instantiating COREM as an extension module in the script used for simulation in NEST.

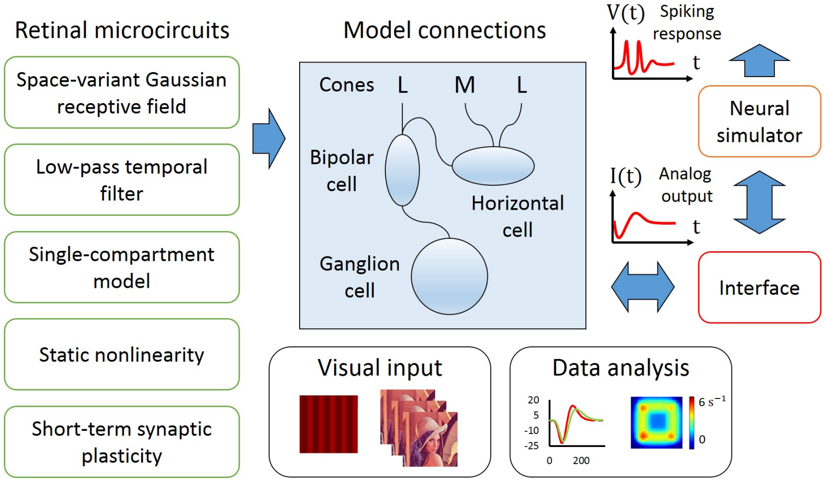

Figure 5.1: Schematic view of the simulation platform COREM connected to a spiking neural network simulator. The user can select and connect different retinal microcircuits through a retina script, and also configure the type of visual input and the method for analysis of simulation results. During simulation, while COREM sends data of the analog presynaptic current of ganglion cells, the ganglionar spiking response is reproduced by the spiking neural network simulator.

The development of COREM is a research result by itself. The other type of result presented here corresponds to the evaluation of COREM in terms of its potential to generate different retina models that can capture diverse properties of the retina processing. We constructed three different retina models that describe some well-known properties of the retina processing (see Fig. 5 in Appendix A), adaptation to the mean light intensity and temporal contrast and differential motion sensitivity, and fitted them to published electrophysiological recordings. Our proposed models were adapted from some relevant models described in the literature, but they present some new features and in themselves constitute novel models.

We demonstrated that these models accurately fit different experimental results [MCMP+16]. For instance, our model of photoreceptors and horizontal cells reproduce adaptation to the mean light intensity in response to uniform white pulses at different Weber contrasts, background luminances and as a function of the stimulus drifting frequency (Figs. 6 and 7 in Appendix A). A different retina model accurately predicts temporal contrast adaptation by capturing all adaptive features of temporal filtering and the static nonlinearity in the linear-nonlinear (LN) analysis (Fig. 8 in Appendix A). Finally, we also fitted the neural behavior of Object Motion Sensitive GCs for a jittering stimulus that approximates fixational eye movements (Fig. 10 in Appendix A).

Simulation frameworks that unify different computational theories, as COREM does, facilitate gaining a general understanding of the visual function of the retina, linking together representations at different levels of abstraction.

5.2 Connecting COREM with the Neurorobotics platform of the HBP

The HBP Neurorobotics Platform is a web-based environment that allows scientists to connect brain models to detailed simulations of robot bodies and environments and to use the resulting neurorobotic systems for in silico experimentation [Neu18]. To illustrate the capabilities of the platform during the ramp-up phase of the HBP, some case-study examples were developed. COREM was used in a experiment of visual tracking that embedded a color-opponent retina model on the iCub humanoid robot [FVA+17]. The retina model was fed by the sequence of camera images from the simulated robot, which was tracking a green target on a red background, and provided, as an output, analog values representing the intensity of presynaptic currents of GCs. These currents were later integrated by 1280 IF neurons located at a subsequent stage, within the simulated brain model of the robot. This brain model was able to correctly detect a moving target and to generate motor commands for the eye that make the robot performs visual tracking of the moving target.

5.3 Genetic algorithm for automated parameter search

Neuronal models often have multiple parameters that are difficult to estimate manually. In our work [MCMP^{+}17c], we proposed a GA optimization as an effective method for automated parameter search of large-scale models of the visual system pathway. We applied our optimization framework to two different models of the visual system. The first one is a model of cone photoreceptors and horizontal cells that reproduces adaptation to the mean light intensity in the retina. It was configured using the simulation platform COREM. The second model is an implementation of the large-scale thalamocortical system developed by Hill and Tononi [HT05].

Neural records of cells in the visual system are often analyzed in terms of the cell's receptive field and its temporal response. We have shown that a standard point-by-point comparison of traces (e.g., by using only the mean-squared error) was insufficient to characterize high-frequency components of the temporal response of a example retina model (see Fig. 1 in Appendix B). This type of data requires a fine point-by-point comparison of response traces between the simulated output and the recorded data in order to understand all possible mechanisms that modulate the visual response. To address this challenge, we defined a multiobjective fitness function that combines two types of error metrics, the normalized root-mean-square error and a shape error descriptor.

Two extreme solutions to the multiobjective optimization were shown in Fig. 3 in Appendix B. High-frequency oscillations are seen to be better captured by the minimum shape-error solution of the Pareto-optimal front, particularly within the first 100 ms of the 100 td response. However, this solution presents also significant deviations from the target data in some specific points. On the contrary, the other solution has a smaller square error but does not reproduce all high-frequency features of the data. By analyzing this type of results we can modify the model specifications and reconsider the initial hypotheses about the mechanisms that shape the visual response.

Parameters of the large-scale model of the thalamocortical system were fitted by an error metric that compares the average and target membrane potentials of populations over given time intervals. We used the target membrane potentials estimated from results of the modeling study of this system [HT05]. The GA optimization allowed us to bring the model of the thalamocortical system into a stable parameter regime where it reproduces qualitatively the neural behavior of the original model (see Figs. 4 and 5 in Appendix B).

5.4 Biophysical network modeling of the dLGN circuit

This work was developed in collaboration with the research group at the Centre for Integrative Neuroplasticity, CINPLA (University of Oslo) [CIN18]. We constructed a biophysically detailed model of the dLGN circuit to study the effects of cortical feedback on spatial response properties of RCs [MCMH^{+}18]. The network model consists of two-dimensional grids of synaptically connected dLGN neurons (RCs and INs) and cortical neurons (orientation-selective layer-6 simple cells) of ON and OFF receptive-field arrangements (Fig. 1 in Appendix C).

The main focus of the study was exploration of the effects of cortical feedback on the spatial responses of RCs to flashing-spot and patch-grating stimuli. However, before studying the effects of cortical feedback on the RC response, we evaluated the feedforward response of the different cell types in the network model when the cortical feedback is deactivated. The main result here is that the spatiotemporal receptive-field profiles of cortical cells were seen to resemble the experimentally-observed receptive field for a "separable simple cell" (Fig. 4 in Appendix C). We further computed two receptive-field measures: an overlap index assessing the spatial segregation of subregions within the receptive field and a push-pull index determining the relative weight of the antagonistic response to stimuli of opposite contrast, and confirmed that they were compatible with what has been observed for cortical simple cells.

After exploring the feedforward response of the different cell types in the network model, we then moved on to investigate how cortical feedback affects the spatial response properties of RC cells. We considered two different arrangements of synaptic feedback from the ON and OFF zones in the visual cortex to the dLGN: phase-reversed ("push-pull") and phase-matched ("push-push"), as well as different spatial extents of the corticothalamic projection pattern. We primarily employed the so-called area-response curves, a commonly used measure of visual responses for cells in the early stages of the visual system. Our simulation results support that a phase-reversed arrangement provides a more effective way for cortical feedback to provide the increased center-surround antagonism seen in experiments both for flashing spots and, even more prominently, for patch gratings, as shown in Figs. 10 and 14 in Appendix C. An additional effect of the phase-reversed feedback is the shrinking of the stimulus size that gives the maximum response in the area-response curves, clearly observed for the phase-reversed feedback, but largely absent for phase-matched feedback (Figs. 10 and 14 in Appendix C). When comparing the different spatial divergences of the feedback, the 2 × 2 feedback pattern was seen to be more effective in increasing surround suppression in the RC response than the 1 × 1 (Figs. 16-20 in Appendix C), which is in accordance with anatomical observations of the spatial spread of corticothalamic axons.

The feedback-induced increase in the center-surround antagonism of RCs may be understood as a top-down phenomenon that dynamically sharpens the spatial focus of the receptive field and increase its spatial resolution.

5.5 A conductance-based network model of the primate visual system

The last research work of this Thesis corresponds to the biologically realistic implementation of a network model of the primate visual system (retina, LGN and V1) with the focus on studying color mechanisms at the different stages of the visual pathway. The results of this work are included in the two journal articles submitted for publication [MCMP18, MCMP17a]. Here, we will review the main properties of the model and present our main simulation results.

The network model consists of two-dimensional grids of neurons that represent the retina, LGN and layers 2-3, 4Cβ and 5-6 in V1. The architectures of the LGN and V1 are shown in the left diagram of Figure 5.2. The representation of the multilayered retina model can be found in [MCMP$^+$17b]. Each layer is scaled to span a patch of 2° × 2° or a patch of 3° × 3° of the foveal visual field and contains 40 × 40 neurons or 60 × 60 neurons respectively. The cortical magnification factor of a foveal region in V1 ($< 2^\circ$) is estimated to be between 4 and 16 $mm/^\circ$ [CYR13, SWT07, DSVB81]. Assuming the most conservative estimate of 4 $mm/^\circ$, a 2° × 2° patch in the fovea of our model V1 would correspond to 64 mm^2 of striate cortical surface, and a 3° × 3° patch, would be 144 mm^2 of striate cortical surface.

In the LGN, every RC and IN receive as input the spike trains from retinal GCs (more details about the retina model used to generate the spike train input can be found in [MCMP$^+$17b]). INs, in turn, inhibit both RCs and other INs (Figure 5.2). In primate, there are about as many RCs as GCs and there is an approximate one-to-one anatomical mapping from retina to RCs [HWSM15, SKAT96]. As a

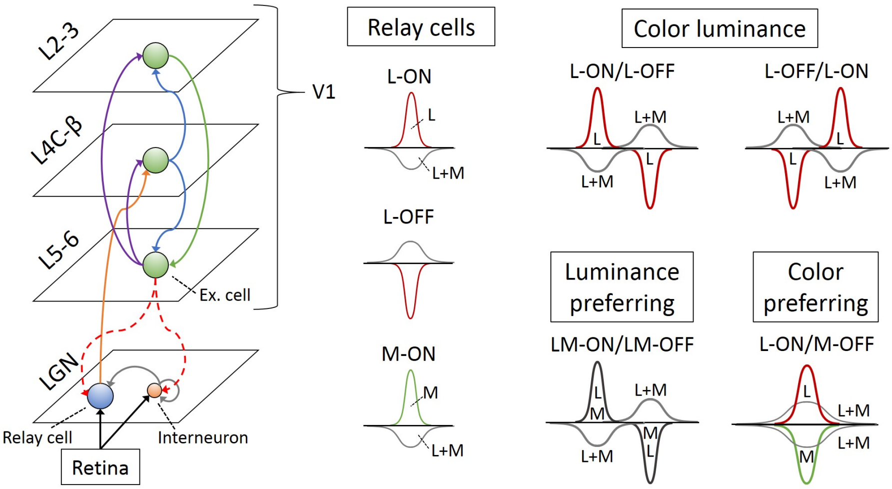

Figure 5.2: Schematic of the circuit model and spatial profiles of receptive fields of LGN RCs and some example subpopulations of cortical cells. The diagram of the circuit model depicts the main connections of the network: retinal inputs to RCs and INs, inhibitory connections from INs, thalamocortical connections (from RCs to layer 4Cβ cells), vertical interlaminar connections in V1 and corticothalamic connections (from layer 5-6 cells to LGN cells). Horizontal intralaminar connections in V1 (both excitatory and inhibitory) are not shown. The spatial profiles of receptive fields are composed of subregions (subregions above the black line are excitatory and below are inhibitory). Within each subregion, it is indicated the type of cone input received by the subregion, L- or M-cone, or a mixture of both. Figure adapted from [MCMP18].

result, the receptive-field properties of GCs and RCs are similar and display the classical center-surround antagonistic structure where a narrow excitatory center is surrounded by a wider inhibitory surround (ON-center cells) or a narrow inhibitory center is surrounded by a wider excitatory surround (OFF-center cells) (see receptive-field profiles in Figure 5.2). Combining the different alternatives, i.e., the type of cone that drives the receptive-field center and the type of response, ON or OFF, there are 4 possible receptive fields of RCs in the model: L-ON, L-OFF, M-ON and M-OFF.

RCs project to layer 4Cβ neurons in V1, where the thalamic information is transmitted to other layers of the cortical circuitry. Figure 5.2 shows the vertical interlaminar connections included in the model network of V1, which were configured based on the simplified circuit model of V1 proposed by Callaway [Cal98]. Layer 4Cβ neurons project axons primarily to layer 2-3, but also to layer 5-6. Layer 2-3 neurons in turn project to layer 5-6. Layer 5-6 neurons provide feedback projections to layers 2-3 and layer 4Cβ. The model also includes the corticothalamic connection from cells in layer 5-6 to LGN cells, both RCs and INs.

Cortical cells are classified based on their physiological response to chromatic and achromatic patterns [JHS01]. The population of cortical cells is divided into three groups: luminance-preferring, color-luminance and color-preferring cells. LP cells give a minimal response to equiluminant gratings, but respond well to luminance patterns, CL cells are spatially tuned for both equiluminant and luminance patterns and CP cells show large responses to equiluminant gratings and little response to luminance gratings. In the last version of the model [MCMP18], LP cells are 64 % of the total amount of cortical cells, CL cells are 29 % and CP cells are 7 %, in agreement with experimental data of V1 cells [SH11].

Spatial profiles of cortical receptive fields are shown on the right in Figure 5.2. LP and CL cells have oriented receptive fields with odd-symmetry: receptive fields formed by two adjacent elongated subregions, ON and OFF, of similar weights [SH11, JHS04]. The cross-section spatial profiles of these two subregions, as implemented in our model, are depicted in Figure 5.2. Receptive fields of CL cells have subregions that are fed only by a single type of RC. For example, the L-ON/L-OFF receptive field has a left subregion that receives input from L-ON RCs and a right subregion that receives input from L-OFF RCs. LP receptive-fields have subregions that merge inputs from two types of RCs of the same sign. CP cells are not orientation selective and have subregions that are approximately circular in shape and concentric [JHS08]. The receptive-field centers of CP cells receive inputs from L- and M- cones that are of opposite sign. Unlike LGN cells, receptive fields of CP cells may be designated as Type II [SH11] because the spatial spread of center and surround are roughly identical.

Two different conductance-based neuron models were employed for representing spiking neurons. To explain the formation of receptive fields in layer 4Cβ in V1 [MCMP17a], a simple conductance-based IF model (*iaf_cond_alpha*) was sufficient. For the second version of the primate network model [MCMP18], we found that more complex phenomena such as wave propagation in V1 required incorporating additional mechanisms to the neuron dynamics. In this scenario, we employed the adaptive exponential IF model (*aeif_cond_alpha*), which does not increase significantly the complexity of simulation and captures the complex intrinsic properties seen in neurons of the LGN and V1, such as low-threshold spike, regular spiking or fast-spiking [BG05].

Next we focus on simulation results obtained with the network model. In the first article [MCMP17a], we exhaustively evaluated the model response against well-established chromatic and achromatic visual stimuli (disk- and ring-shaped light flashes, spatially uniform squares and sine-wave gratings of varying spatial frequency). Of particular importance are the model responses to the different kinds of grating patterns, as shown for some representative neuron types in Figure 5.3. Spatial frequency tuning curves have been widely used to understand the neuronal basis of color mechanisms [LSHS12, CMPD11, JHS08, JHS01]. Parvocellular LGN cells multiplex luminance information at high spatial frequencies and chromatic information at low spatial frequencies [KB01]. As shown for the L-ON RC in Figure 5.3, the response to chromatic gratings is low-pass in shape but the response to luminance gratings is band-pass. In agreement with physiological data from parvocellular cells near the fovea [LSHS12], the luminance response of model cells shows a peak at about 3 cpd. Their responses to L- and M-cone-isolating gratings are also consistent with the responses measured experimentally to cone-isolating gratings: almost low-pass in shape but with a 180-degree phase difference at low spatial frequencies (not shown here), indicating opponency.

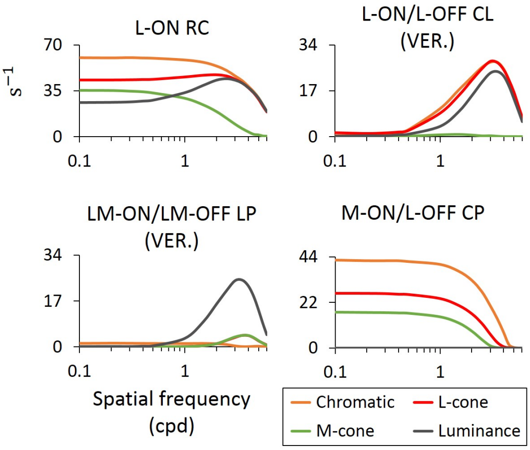

Figure 5.3: Spatial frequency tuning curves of neurons situated in the center of each grid using four different kinds of grating patterns: luminance, chromatic equiluminant red/green, and M- or L-cone-isolating gratings. Figure adapted from [MCMP17a].

Spatial frequency tuning curves of cortical cells in Figure 5.3 are in conformity with the responses described by Johnson et al. [JHS08, JHS01]. LP cells show little or no response to chromatic gratings, but respond well to luminance gratings. The response to the luminance grating is band-pass in shape, with a peak at 3-4 cpd that is not significantly different from the range of values reported [JHS01] for LP cells (2-3 cpd). CL cells give comparable responses to both luminance and chromatic gratings. The preferred spatial frequency of these cells is also in the range 3-4 cpd. CP cells give large responses to chromatic gratings (low-pass in shape) and no response to luminance gratings. A qualitative evaluation of the degree of similarity between simulated and experimental responses can be made by visual comparison with Fig. 1 in the referenced paper [JHS01].

In the second article [MCMP18], we investigated V1 population responses to chromatic and achromatic surfaces of different sizes (1° and 2°) and compared our simulation results with the findings of a recent neuroimaging study [ZZSS15]. According to this study, V1 population responses to chromatic and achromatic surfaces remain both edge-enhanced throughout the stimulus presentation but only achromatic surfaces elicit a neuronal *filling-in* response of the center. We replicated the conditions of their experiment and observed similar properties of the population responses.

Intracortical interactions between the different types of cortical populations play a major role in shaping the population-average response. The populations of oriented cells that respond to edges, LP and CL cells, represent the largest percentage of cortical cells (more than 90 % in our model). Therefore, for the achromatic square, the summed response of these two populations results in a more pronounced edge response of the population average that, in turn, favors a gradual horizontal propagation of the signal from the edges to center. The chromatic square activates solely the CL population at the edges, which is not sufficient to evoke a strong neuronal *filling-in* of the center.

Chapter 6

Conclusions

In this Thesis we have presented, by using the format of “group of publications”, novel computational tools and models of the early visual system that could help the Neuroscience community to gain insight into the neural mechanisms underlying the early processing of visual information. The objectives and contributions of this Thesis were presented in Chapter 1. Here we summarize the main contributions of this work adding some concluding remarks (Section 6.1). Future work is described in Section 6.2.

6.1 Main contributions

We have developed a configurable software platform that facilitates the implementation of retina models at different abstraction levels, from single-cell to large-scale levels. We have also investigated the spatial effects of cortical feedback on the relay-cell response by means of a biophysically detailed network model of the LGN. Color mechanisms were explored by using a comprehensive network model of the first stages in the primate parvocellular pathway, which represent the retina, the LGN and a simplified version of the multilayered structure of V1. In parallel, different optimization strategies based on genetic algorithm were investigated to fit parameters of some of the models proposed in this work.

In general terms, compared to other biological models for vision, our models make the following contributions:

- They are large-scale realistic implementations whose parameters were carefully tuned based on physiological and anatomical data. In this manner, we ensure that our models are reliable enough to validate hypotheses raised on the basis of experimental findings.

- They generalize the computational basis of the visual processing, rather than fitting the model response to a single experimental result. While many of the proposed vision models share common computational stages, previous efforts have been more focused on fitting specific experimental observations rather than generalizing the model beyond a particular result. We believe that a general and unified modeling framework may facilitate bridging the gap between lower level mechanisms and a coherent functional description of the visual system.

- They achieve the best tradeoff between complexity to describe functionality and biological accuracy. Thus, when designing a new model we have always tried to find the appropriate level of abstraction necessary to capture most properties of the neural response.

- For the purpose of independent validation and further scientific exploration, these models were implemented using well-established simulation tools, such as NEST [NES18], and all the code projects have been released as open source software [Git18]. The software was designed for easy use and to be interfaced with other well-established simulation tools used by the Neuroscience community. An important goal achieved here was the integration of our retina simulation platform within the Neurorobotics Platform of the HBP.

The software has been implemented using C++ and Python as programming languages. One of our goals when designing this software has been to optimize efficiency of all its modules. An example of this optimization effort is reflected in computations of spatiotemporal equations performed by the space-variant Gaussian receptive field and the low-pass temporal filter in COREM. Both modules are formulated as recursive filters and, also, the Gaussian filter is based on OpenMP to gain thread-level parallelism. We have also implemented a parallel processing architecture in a computer cluster based on the MPI interface, as described previously (4.4). To generate all simulation results presented in this Thesis, we have spent approximately more than 500000 CPU hours in the Stallo supercomputer [Sta18].

6.2 Future work

The most interesting future application of the present work would be to further explore color mechanisms in V1. In particular, brightness-color interactions seen in V1 have recently drawn attention to the role which the different cortical cell types can play in shaping color information. The interaction between brightness and color can cause that the color appearance of an object changes when viewing the object against surrounds of different brightness. It has been shown that brightness and color interact strongly already within V1 by using chromatic visual-evoked potentials [XOC$^+$15]. The main finding is that brightness-color interactions take place at the edges of the surface, where LP cells may produce an amount of inhibition proportional to the level of luminance contrast. A promising next application of our model of the primate visual system would be to explore its response properties to color surfaces when the luminance of the surround is changed and to evaluate whether the model can capture the brightness-color interactions observed in V1.

Another interesting topic for a future study would be to investigate the applicability of this model in other perceptual phenomena of *filling-in*. Perceptual *filling-in* occurs in a variety of situations [Kom06]: when there are deficits of visual inputs, when steady fixation is maintained, or by using some well-known illusions (e.g., *colour spreading*). Neurophysiological and neuroimaging studies have shown that in most of these situations, early visual areas are activated. Experimentation with the present model might be of great help to answer the important question on whether the different phenomena of *filling-in* share common mechanisms.

Other model that can be further investigated is the biophysically detailed network model of the LGN. There are many aspects of the thalamocortical and corticothalamic circuits that have been disregarded in the present model and it would be worth studying their influence on the relay-cell response. For example, our LGN model assumes static synapses while a number of studies have observed short-term plasticity in different synapses of the thalamocortical circuit. Short-term depression has been seen at the retinogeniculate [TS98] and geniculocortical [BF05] synapses, as well as in the feedback connection from cortex to INs [AYH11]. In contrast, the feedback connection from cortex to RCs appears to be facilitating [TS98]. Such plasticity opens up for an even richer dynamical repertoire of the circuit, and would be an interesting topic for a future study.

Further in the LGN model, there are several neural mechanisms that our simplified circuit of cortical orientation tuning does not account for, such as recurrent cortical excitation or horizontal inhibitory connections [FM00], which can amplify a weak orientation bias. Stimuli presented at non-preferred orientations do not suppress cortical response of the model to the background rate as observed experimentally in some cells [SF82]. However, we can take advantage of the experience gained with the model of the primate visual system, which incorporates recurrent intracortical connections and horizontal inhibitory connections, to introduce a stronger orientation selectivity of cortical cells and see whether it affects the feedback-induced changes in the relay-cell response.

Chapter 7

Conclusiones

En esta Tesis se han presentado, utilizando la modalidad de “agrupación de publicaciones”, nuevos modelos y herramientas computacionales de las primeras etapas del sistema visual con objeto de ayudar a la comunidad Neurocientífica a obtener un mayor conocimiento de los mecanismos neuronales subyacentes al procesamiento de la información visual. Los objetivos y contribuciones de esta Tesis han sido expuestos en el Capítulo 2. En este capítulo nos limitamos a resumir las principales contribuciones del trabajo añadiendo algunas observaciones finales (Sección 7.1). El trabajo futuro se describe en la Sección 7.2.

7.1 Principales aportaciones

Se ha desarrollado una plataforma software configurable que facilita la implementación de modelos de retina a diferentes niveles de abstracción, desde el nivel unicelular a niveles de red de gran escala. También hemos investigado los efectos del “feedback” de corteza visual en la respuesta espacial de las RCs usando un modelo del LGN biofísicamente detallado. Los mecanismos de color han sido investigados en base a un modelo completo de las primeras etapas del camino parvocelular del primate, que representa la retina, el LGN y una versión simplificada de la estructura multi-capas de V1. En paralelo, diferentes estrategias de optimización basadas en algoritmo genético han sido investigadas para ajustar los parámetros de algunos de los modelos propuestos en este trabajo.

En términos generales, comparados con otros modelos biológicos de visión, nuestros modelos aportan las siguientes contribuciones:

- Son implementaciones realistas de gran escala cuyos parámetros han sido cuidadosamente ajustados basándose en datos fisiológicos y anatómicos. De esta forma, nos aseguramos que nuestros modelos son lo suficientemente fiables para validar hipótesis planteadas en base a resultados experimentales.
- Generalizan los fundamentos de computación del procesamiento visual, en vez de ajustar la respuesta del modelo a un único resultado experimental. Aunque muchos de los modelos de visión propuestos comparten etapas computacionales similares, se ha prestado más atención a ajustar el modelo a datos experimentales específicos en vez de generalizar el modelo más allá de un resultado concreto. Pensamos que los esfuerzos de investigación deben buscar un marco de modelado general y unificado que relacione los conocimientos que tenemos de los mecanismos neuronales de bajo nivel y la posibilidad de generar una descripción funcional coherente y cuantitativa del sistema visual.
- Alcanzan un buen compromiso entre la complejidad en el diseño del modelo y su precisión biológica. Es decir, a la hora de diseñar nuestros modelos hemos intentado siempre alcanzar el nivel apropiado de abstracción necesario para reproducir la mayoría de las propiedades de la respuesta neuronal.
- Para que puedan ser validados de forma independiente y se pueda seguir avanzando en su investigación, los modelos han sido implementados usando herramientas de simulación estandarizadas, como lo es NEST [NES18], y todo el código de los proyectos ha sido publicado como software de código abierto [Git18]. El software ha sido diseñado para un uso sencillo y para ser conectado con otras herramientas de simulación estándar en la comunidad Neurocientífica. Un éxito rotundo en este ámbito ha sido la integración de nuestra plataforma de simulación de modelos de retina con la Plataforma de Neurorobótica del HBP.

El software ha sido implementado haciendo uso de C++ y Python como lenguajes de programación. Uno de nuestros objetivos al diseñar este software ha sido optimizar la eficiencia de todos sus módulos. Un ejemplo del esfuerzo de optimización realizado se encuentra en los cálculos de las ecuaciones espacio-temporales llevadas a cabo por el filtro Gaussiano con variación espacial y el filtro paso-baja temporal de COREM. Ambos módulos han sido formulados como filtros recursivos y, además, el filtro Gaussiano hace uso de OpenMP para conseguir paralelismo a nivel de hebra. Se ha implementado también una arquitectura de procesamiento en paralelo en cluster basada en la interfaz MPI, como se ha descrito previamente (4.4). Para generar todos los resultados de simulación presentados en esta Tesis, hemos usado aproximadamente más de 500000 horas de cómputo en CPU en el supercomputador Stallo [Sta18].

7.2 Trabajo futuro

La aplicación futura más interesante del presente trabajo sería explorar en mayor detalle los mecanismos de color en V1. En particular, las interacciones color-brillo observadas en V1 han atraído recientemente la atención respecto al papel que los distintos tipos de células corticales puedan desempeñar en la formación de la señal de color. La interacción entre el color y el brillo puede dar lugar a que la apariencia de color de un objeto cambie cuando el objeto se está viendo rodeado de entornos de diferente brillo. Se ha demostrado que el color y el brillo interactúan ya de forma marcada en V1 haciendo uso de potenciales visuales evocados [XOC$^+$15]. El descubrimiento principal es que las interacciones color-brillo tienen lugar en los bordes de las superficies, donde las células que responden preferentemente a la luminancia producen una cantidad de inhibición proporcional al nivel de contraste en luminancia. Una aplicación futura de nuestro modelo del sistema visual del primate consistiría en explorar las propiedades de la respuesta a las superficies de color cuando la luminancia del entorno que las rodea cambia y evaluar así si el modelo es capar de reproducir las interacciones color-brillo observadas en V1.

Otro tema interesante para un estudio futuro sería la investigación de la aplicabilidad de este modelo a otros fenómenos perceptuales de “filling-in”. El “filling-in” perceptual ocurre en diversas situaciones [Kom06]: cuando hay un déficit de entradas visuales, cuando se mantiene la vista fija en un punto, o usando ilusiones ópticas bien conocidas (e.g., “colour spreading”). Estudios neurofisiológicos y de “neuroimagen” han mostrado que en la mayoría de estas situaciones, las áreas tempranas de procesamiento visual se activan. La experimentación usando el modelo presente podría ser de gran ayuda para responder a la importante pregunta de si los diferentes fenómenos de “filling-in” comparten mecanismos comunes.

Otro modelo con el que se podría continuar la investigación es el modelo biofísicamente detallado del LGN ya que hay numerosos aspectos de los circuitos talamocortical y corticotalámico que han sido obviados en la versión presente y sería interesante estudiar cómo su inclusión en el modelo influiría en la respuesta de las RCs. Por ejemplo, nuestro modelo del LGN asume que todas las sinapsis son estáticas, sin embargo un número de estudios han constatado que existe plasticidad de tipo “short-term” en diferentes sinapsis del circuito talamocortical. Se ha observado depresión sináptica en las sinapsis retinogeniculadas [TS98] y geniculocorticales [BF05], así como en las conexiones de “feedback” desde corteza a las INs [AYH11]. Por el contrario, la conexión de “feedback” de corteza a las RCs parece ser de tipo facilitadora [TS98]. Las distintas combinaciones de plasticidad sináptica abren un mayor repertorio de posibilidades para el diseño del circuito, y sería un tema interesante de estudio futuro.

Siguiendo con el modelo del LGN, hay distintos mecanismos neuronales que nuestro modelo simplificado de respuesta a la orientación en corteza visual no ha tenido en cuenta, como son las conexiones recurrentes excitatorias o las conexiones horizontales inhibitorias [FM00], que pueden amplificar una respuesta inicial a la orientación débil. Los estímulos que se han presentado en orientaciones no óptimas no han conseguido suprimir la respuesta cortical del modelo hasta el nivel de respuesta espontánea tal y como se ha observado experimentalmente en algunas células [SF82]. Sin embargo, podemos aprovechar la experiencia adquirida con el modelo del sistema visual del primate, que incorpora conexiones recurrentes excitatorias intracorticales y conexiones horizontales inhibitorias, para dotar a las células corticales de una mayor selectividad a la orientación y observar si esto afecta a los cambios inducidos por la señal de “feedback” en la respuesta de las RCs.

Bibliography

[AFR+97] P Arcelli, C Frassoni, MC Regondi, S De Biasi, and R Spreafico. Gabaergic neurons in mammalian thalamus: a marker of thalamic complexity? *Brain research bulletin*, 42(1):27–37, 1997.

[Alh18] Alhambra supercomputer, 2018. URL: `http://alhambra.ugr.es`.

[AU03] Henry J Alitto and W Martin Usrey. Corticothalamic feedback and sensory processing. *Current opinion in neurobiology*, 13(4):440–445, 2003.

[AYH11] Sigita Augustinaite, Yuchio Yanagawa, and Paul Heggelund. Cortical feedback regulation of input to visual cortex: role of intrageniculate interneurons. *The Journal of physiology*, 589(12):2963–2977, 2011.

[Bab05] Baktash Babadi. Bursting as an effective relay mode in a minimal thalamic model. *Journal of computational neuroscience*, 18(2):229–243, 2005.

[BB12] James M Bower and David Beeman. *The book of GENESIS: exploring realistic neural models with the GEneral NEural SImulation System.* Springer Science & Business Media, 2012.

[BDG+13] Sébastien Béhuret, Charlotte Deleuze, Leonel Gomez, Yves Frégnac, and Thierry Bal. Cortically-controlled population stochastic facilitation as a plausible substrate for guiding sensory transfer across the thalamic gateway. *PLoS computational biology*, 9(12):e1003401, 2013.

[BF05] C Elizabeth Boudreau and David Ferster. Short-term depression in thalamocortical synapses of cat primary visual cortex. *Journal of Neuroscience*, 25(31):7179–7190, 2005.

[BG05] Romain Brette and Wulfram Gerstner. Adaptive exponential integrate-and-fire model as an effective description of neuronal activity. *Journal of neurophysiology*, 94(5):3637–3642, 2005.

[BIBJM99] Michael J Berry II, Iman H Brivanlou, Thomas A Jordan, and Markus Meister. Anticipation of moving stimuli by the retina. *Nature*, 398(6725):334, 1999.

[Bil95] Vincent A Billock. Cortical simple cells can extract achromatic information from the multiplexed chromatic and achromatic signals in the parvocellular pathway. *Vision research*, 35(16):2359–2369, 1995.

[BÖMM08] Stephen A Baccus, Bence P Ölveczky, Mihai Manu, and Markus Meister. A retinal circuit that computes object motion. *Journal of Neuroscience*, 28(27):6807–6817, 2008.

[Bra92] Julie R Brannan. *Applications of parallel processing in vision*, volume 86. Elsevier, 1992.

[BRC+07] Romain Brette, Michelle Rudolph, Ted Carnevale, Michael Hines, David Beeman, James M Bower, Markus Diesmann, Abigail Morrison, Philip H Goodman, Frederick C Harris, et al. Simulation of networks of spiking neurons: a review of tools and strategies. *Journal of computational neuroscience*, 23(3):349–398, 2007.

[BU11] Farran Briggs and W Martin Usrey. Corticogeniculate feedback and visual processing in the primate. *The Journal of physiology*, 589(1):33–40, 2011.

[BUL03] Adam M Briska, Daniel J Uhlrich, and William W Lytton. Computer model of passive signal integration based on whole-cell in vitro studies of rat lateral geniculate nucleus. *European Journal of Neuroscience*, 17(8):1531–1541, 2003.

[Cal98] Edward M Callaway. Local circuits in primary visual cortex of the macaque monkey. *Annual review of neuroscience*, 21(1):47–74, 1998.

[Cal05] Edward M Callaway. Structure and function of parallel pathways in the primate early visual system. *The Journal of physiology*, 566(1):13–19, 2005.

[CCMÁDT+15] Rubén Crespo-Cano, Antonio Martínez-Álvarez, Ariadna Díaz-Tahoces, Sergio Cuenca-Asensi, José Manuel Ferrández, and Eduardo Fernández. On the automatic tuning of a retina model by using a multi-objective optimization genetic algorithm. In *International Work-Conference on the Interplay Between Natural and Artificial Computation*, pages 108–118. Springer, 2015.

[CDP+09] Joanna D Crook, Christopher M Davenport, Beth B Peterson, Orin S Packer, Peter B Detwiler, and Dennis M Dacey. Parallel on and off cone bipolar inputs establish spatially coextensive receptive field structure of blue-yellow ganglion cells in primate retina. *Journal of Neuroscience*, 29(26):8372–8387, 2009.

[CHS07] Matteo Carandini, Jonathan C Horton, and Lawrence C Sincich. Thalamic filtering of retinal spike trains by postsynaptic summation. *Journal of vision*, 7(14):20–20, 2007.

[CHXK08] Alexander Casti, Fernand Hayot, Youping Xiao, and Ehud Kaplan. A simple model of retina-lgn transmission. *Journal of computational neuroscience*, 24(2):235–252, 2008.

[CIN18] CINPLA. university of Oslo, 2018. URL: `http://www.mn.uio.no/ibv/english/research/sections/fyscell/cinpla/`.

[CMPD11] Joanna D Crook, Michael B Manookin, Orin S Packer, and Dennis M Dacey. Horizontal cell feedback without cone type-selective inhibition mediates “red–green” color opponency in midget ganglion cells of the primate retina. *Journal of Neuroscience*, 31(5):1762–1772, 2011.

[CSY16] Logan Chariker, Robert Shapley, and Lai-Sang Young. Orientation selectivity from very sparse lgn inputs in a comprehensive model of macaque v1 cortex. *Journal of Neuroscience*, 36(49):12368–12384, 2016.

[CW96] Edward M Callaway and Anne K Wiser. Contributions of individual layer 2–5 spiny neurons to local circuits in macaque primary visual cortex. *Visual neuroscience*, 13(5):907–922, 1996.

[CYR13] Tristan A Chaplin, Hsin-Hao Yu, and Marcello GP Rosa. Representation of the visual field in the primary visual area of the marmoset monkey: Magnification factors, point-image size, and proportionality to retinal ganglion cell density. *Journal of Comparative Neurology*, 521(5):1001–1019, 2013.

[DA01] Peter Dayan and Laurence F Abbott. *Theoretical neuroscience*, volume 806. Cambridge, MA: MIT Press, 2001.

[Dac00] Dennis M Dacey. Parallel pathways for spectral coding in primate retina. *Annual review of neuroscience*, 23(1):743–775, 2000.

[DCS98] Alain Destexhe, Diego Contreras, and Mircea Steriade. Mechanisms underlying the synchronizing action of corticothalamic feedback through inhibition of thalamic relay cells. *Journal of neurophysiology*, 79(2):999–1016, 1998.

[DNUH98] Alain Destexhe, Mike Neubig, Daniel Ulrich, and John Huguenard. Dendritic low-threshold calcium currents in thalamic relay cells. *Journal of Neuroscience*, 18(10):3574–3588, 1998.

[DPD$^+$00] Dennis Dacey, Orin S Packer, Lisa Diller, David Brainard, Beth Peterson, and Barry Lee. Center surround receptive field structure of cone bipolar cells in primate retina. *Vision research*, 40(14):1801–1811, 2000.

[DPKC11] Lisandro D Dalcin, Rodrigo R Paz, Pablo A Kler, and Alejandro Cosimo. Parallel distributed computing using python. *Advances in Water Resources*, 34(9):1124–1139, 2011.

[DSVB81] BM Dow, AZ Snyder, RG Vautin, and R Bauer. Magnification factor and receptive field size in foveal striate cortex of the monkey. *Experimental brain research*, 44(2):213–228, 1981.

[DVDV93] Russell L De Valois and Karen K De Valois. A multi-stage color model. *Vision research*, 33(8):1053–1065, 1993.

[ECR66] Christina Enroth-Cugell and John G Robson. The contrast sensitivity of retinal ganglion cells of the cat. *The Journal of physiology*, 187(3):517–552, 1966.

[EH00] Gaute T Einevoll and Paul Heggelund. Mathematical models for the spatial receptive-field organization of nonlagged x-cells in dorsal lateral geniculate nucleus of cat. *Visual Neuroscience*, 17(6):871–885, 2000.

[EP12] Gaute T Einevoll and Hans E Plesser. Extended difference-of-gaussians model incorporating cortical feedback for relay cells in the lateral geniculate nucleus of cat. *Cognitive neurodynamics*, 6(4):307–324, 2012.

[FM97] JF Fohlmeister and RF Miller. Impulse encoding mechanisms of ganglion cells in the tiger salamander retina. *Journal of neurophysiology*, 78(4):1935–1947, 1997.

[FM00] David Ferster and Kenneth D Miller. Neural mechanisms of orientation selectivity in the visual cortex. *Annual review of neuroscience*, 23(1):441–471, 2000.

[FVA$^+$17] Egidio Falotico, Lorenzo Vannucci, Alessandro Ambrosano, Ugo Albanese, Stefan Ulbrich, Juan Camilo Vasquez Tieck, Georg Hinkel, Jacques Kaiser, Igor Peric, Oliver Denninger, Nino Cauli, Murat Kirtay, Arne Roennau, Gudrun Klinker, Axel Von Arnim, Luc Guyot, Daniel Peppicelli, Pablo Martínez-Cañada, Eduardo Ros, Patrick Maier, Sandro Weber, Manuel Huber, David Plecher, Florian Röhrbein, Stefan Deser, Alina Roitberg, Patrick van der Smagt, Rüdiger Dillman, Paul Levi, Cecilia Laschi, Alois C. Knoll, and Marc-Oliver Gewaltig. Connecting artificial brains to robots in a comprehensive simulation framework: The neurorobotics platform. *Frontiers in neurorobotics*, 11:2, 2017.

[FZH03] Howard S Friedman, Hong Zhou, and Rüdiger Heydt. The coding of uniform colour figures in monkey visual cortex. *The Journal of physiology*, 548(2):593–613, 2003.

[GD07] Marc-Oliver Gewaltig and Markus Diesmann. Nest (neural simulation tool). *Scholarpedia*, 2(4):1430, 2007.

[Git18] Github repository, 2018. URL: `https://github.com/pablomc88`.

[GLS99] William Gropp, Ewing Lusk, and Anthony Skjellum. *Using MPI: portable parallel programming with the message-passing interface*, volume 1. MIT press, 1999.

[GYLL13] Shaobing Gao, Kaifu Yang, Chaoyi Li, and Yongjie Li. A color constancy model with double-opponency mechanisms. In *Computer Vision (ICCV), 2013 IEEE International Conference on*, pages 929–936. IEEE, 2013.

[GYLL15] Shao-Bing Gao, Kai-Fu Yang, Chao-Yi Li, and Yong-Jie Li. Color constancy using double-opponency. *IEEE transactions on pattern analysis and machine intelligence*, 37(10):1973–1985, 2015.

[HAH$^+$11] Geir Halnes, Sigita Augustinaite, Paul Heggelund, Gaute T Einevoll, and Michele Migliore. A multi-compartment model for interneurons in the dorsal lateral geniculate nucleus. *BMC neuroscience*, 12(1):P222, 2011.

[HBP18] Human Brain Project (HBP), 2018. URL: `https://www.humanbrainproject.eu/en`.

[HC97] Michael L Hines and Nicholas T Carnevale. The neuron simulation environment. *Neural computation*, 9(6):1179–1209, 1997.

[Hér96] Jeanny Hérault. A model of colour processing in the retina of vertebrates: From photoreceptors to colour opposition and colour constancy phenomena. *Neurocomputing*, 12(2-3):113–129, 1996.

[HFW02] Matthias H Hennig, Klaus Funke, and Florentin Wörgötter. The influence of different retinal subcircuits on the nonlinearity of ganglion cell behavior. *Journal of Neuroscience*, 22(19):8726–8738, 2002.

[HHHE16] Thomas Heiberg, Espen Hagen, Geir Halnes, and Gaute T Einevoll. Biophysical network modelling of the dlgn circuit: Different effects of triadic and axonal inhibition on visual responses of relay cells. *PLoS computational biology*, 12(5):e1004929, 2016.

[HT01] Fernand Hayot and Daniel Tranchina. Modeling corticofugal feedback and the sensitivity of lateral geniculate neurons to orientation discontinuity. *Visual neuroscience*, 18(6):865–877, 2001.

[HT05] Sean Hill and Giulio Tononi. Modeling sleep and wakefulness in the thalamocortical system. *Journal of neurophysiology*, 93(3):1671–1698, 2005.

[HW59] David H Hubel and Torsten N Wiesel. Receptive fields of single neurones in the cat's striate cortex. *The Journal of physiology*, 148(3):574–591, 1959.

[HW62] David H Hubel and Torsten N Wiesel. Receptive fields, binocular interaction and functional architecture in the cat's visual cortex. *The Journal of physiology*, 160(1):106–154, 1962.

[HW07] Matthias H Hennig and Florentin Wörgötter. Effects of fixational eye movements on retinal ganglion cell responses: A modelling study. *Frontiers in computational neuroscience*, 1:2, 2007.

[HWSM15] Judith A Hirsch, Xin Wang, Friedrich T Sommer, and Luis M Martinez. How inhibitory circuits in the thalamus serve vision. *Annual review of neuroscience*, 38:309–329, 2015.

[IE08] Eugene M Izhikevich and Gerald M Edelman. Large-scale model of mammalian thalamocortical systems. *Proceedings of the national academy of sciences*, 105(9):3593–3598, 2008.

[JAA$^+$12] Helen E Jones, Ian M Andolina, Bashir Ahmed, Stewart D Shipp, Jake TC Clements, Kenneth L Grieve, Javier Cudeiro, Thomas E Salt, and Adam M Sillito. Differential feedback modulation of center and surround mechanisms in parvocellular cells in the visual thalamus. *Journal of Neuroscience*, 32(45):15946–15951, 2012.

[JHS01] Elizabeth N Johnson, Michael J Hawken, and Robert Shapley. The spatial transformation of color in the primary visual cortex of the macaque monkey. *Nature neuroscience*, 4(4):409, 2001.

[JHS04] Elizabeth N Johnson, Michael J Hawken, and Robert Shapley. Cone inputs in macaque primary visual cortex. *Journal of Neurophysiology*, 91(6):2501–2514, 2004.

[JHS08] Elizabeth N Johnson, Michael J Hawken, and Robert Shapley. The orientation selectivity of color-responsive neurons in macaque v1. *Journal of Neuroscience*, 28(32):8096–8106, 2008.

[JIH$^+$18] Jakob Jordan, Tammo Ippen, Moritz Helias, Itaru Kitayama, Mitsuhisa Sato, Jun Igarashi, Markus Diesmann, and Susanne Kunkel. Extremely scalable spiking neural network simulation code: from laptops to exascale computers. *Frontiers in Neuroinformatics*, 12:2, 2018.

[KB01] Ehud Kaplan and Ethan Benardete. The dynamics of primate retinal ganglion cells. In *Progress in brain research*, volume 134, pages 17–34. Elsevier, 2001.

[KFN18] Helga Kolb, Eduardo Fernández, and Ralph Nelson. Webvision: The organization of the retina and visual system, 2018. URL: `http://webvision.med.utah.edu/`.

[KG98] Kyle L Kirkland and George L Gerstein. A model of cortically induced synchronization in the lateral geniculate nucleus of the cat: a role for low-threshold calcium channels. *Vision research*, 38(13):2007–2022, 1998.

[KMB11] Tatiana Kameneva, Hamish Meffin, and Anthony N Burkitt. Modelling intrinsic electrophysiological properties of on and off retinal ganglion cells. *Journal of computational neuroscience*, 31(3):547–561, 2011.

[KMS79] EHUD Kaplan, SERGIU Marcus, and Y Tat So. Effects of dark adaptation on spatial and temporal properties of receptive fields in cat lateral geniculate nucleus. *The Journal of physiology*, 294(1):561–580, 1979.

[Kom06] Hidehiko Komatsu. The neural mechanisms of perceptual filling-in. *Nature reviews neuroscience*, 7(3):220, 2006.

[KR03] Kerry J Kim and Fred Rieke. Slow na+ inactivation and variance adaptation in salamander retinal ganglion cells. *Journal of Neuroscience*, 23(4):1506–1516, 2003.

[Kre05] Jan Kremers. *The primate visual system: a comparative approach.* John Wiley & Sons, 2005.

[KVE92] James J Knierim and David C Van Essen. Visual cortex: cartography, connectivity, and concurrent processing. *Current Opinion in Neurobiology*, 2(2):150–155, 1992.

[KW96] J Köhn and Florentin Wörgötter. Corticofugal feedback can reduce the visual latency of responses to antagonistic stimuli. *Biological cybernetics*, 75(3):199–209, 1996.

[LH88] Margaret Livingstone and David Hubel. Segregation of form, color, movement, and depth: anatomy, physiology, and perception. *Science*, 240(4853):740–749, 1988.

[LHL$^+$14] Henrik Lindén, Espen Hagen, Szymon Leski, Eivind S Norheim, Klas H Pettersen, and Gaute T Einevoll. Lfpy: a tool for biophysical simulation of extracellular potentials generated by detailed model neurons. *Frontiers in neuroinformatics*, 7:41, 2014.

[LMG10] Barry B Lee, Paul R Martin, and Ulrike Grünert. Retinal connectivity and primate vision. *Progress in retinal and eye research*, 29(6):622–639, 2010.

[LSHS12] Barry B Lee, Robert M Shapley, Michael J Hawken, and Hao Sun. Spatial distributions of cone inputs to cells of the parvocellular pathway investigated with cone-isolating gratings. *JOSA A*, 29(2):A223–A232, 2012.

[LTL$^+$95] AG Leventhal, KG Thompson, D Liu, YIFENG Zhou, and SJ Ault. Concomitant sensitivity to orientation, direction, and color of cells in layers 2, 3, and 4 of monkey striate cortex. *Journal of Neuroscience*, 15(3):1808–1818, 1995.

[MÁCCDT$^+$16] Antonio Martínez-Álvarez, Rubén Crespo-Cano, Ariadna Díaz-Tahoces, Sergio Cuenca-Asensi, José Manuel Ferrández Vicente, and Eduardo Fernández. Automatic tuning of a retina model for a cortical visual neuroprosthesis using a multi-objective optimization genetic algorithm. *International journal of neural systems*, 26(07):1650021, 2016.

[Mas01] Richard H Masland. The fundamental plan of the retina. *Nature neuroscience*, 4(9):877, 2001.

[Mas12] Richard H Masland. The neuronal organization of the retina. *Neuron*, 76(2):266–280, 2012.

[MBC08] Valerio Mante, Vincent Bonin, and Matteo Carandini. Functional mechanisms shaping lateral geniculate responses to artificial and natural stimuli. *Neuron*, 58(4):625–638, 2008.

[MCMH+18] Pablo Martínez-Cañada, Milad Hobbi Mobarhan, Geir Halnes, Marianne Fyhn, Christian Morillas, Francisco Pelayo, Gaute T Einevoll, et al. Biophysical network modeling of the dlgn circuit: Effects of cortical feedback on spatial response properties of relay cells. *PLoS computational biology*, 14(1):e1005930, 2018.

[MCMP+16] Pablo Martínez-Cañada, Christian Morillas, Begoña Pino, Eduardo Ros, and Francisco Pelayo. A computational framework for realistic retina modeling. *International journal of neural systems*, 26(07):1650030, 2016.

[MCMP17a] Pablo Martínez-Cañada, Christian Morillas, and Francisco Pelayo. A neuronal network model of the primate visual system: Color mechanisms in the retina, LGN and V1. *International Journal of Neural Systems. Submitted for publication*, 2017.

[MCMP+17b] Pablo Martínez-Cañada, Christian Morillas, Francisco Pelayo, et al. A conductance-based neuronal network model for color coding in the primate foveal retina. In *International Work-Conference on the Interplay Between Natural and Artificial Computation*, pages 63–74. Springer, 2017.

[MCMP+17c] Pablo Martínez-Cañada, Christian Morillas, Hans E Plesser, Samuel Romero, Francisco Pelayo, et al. Genetic algorithm for optimization of models of the early stages in the visual system. *Neurocomputing*, 250:101–108, 2017.

[MCMP18] Pablo Martínez-Cañada, Christian Morillas, and Francisco Pelayo. A neuronal network model of the primate visual system: Coding of color surfaces. *Journal of Computational Neuroscience. Submitted for publication*, 2018.

[Mic88] Charles R Michael. Retinal afferent arborization patterns, dendritic field orientations, and the segregation of function in the lateral geniculate nucleus of the monkey. *Proceedings of the National Academy of Sciences*, 85(13):4914–4918, 1988.

[Min18] Ali A Minai. Computational neuroscience: A brief overview. 2018.

[MMMW+14] Luis M Martinez, Manuel Molano-Mazón, Xin Wang, Friedrich T Sommer, and Judith A Hirsch. Statistical wiring of thalamic receptive fields optimizes spatial sampling of the retinal image. *Neuron*, 81(4):943–956, 2014.

[MRM+07] Christian A Morillas, Samuel F Romero, Antonio Martínez, Francisco J Pelayo, Eduardo Ros, and Eduardo Fernández. A design framework to model retinas. *Biosystems*, 87(2-3):156–163, 2007.

[MSS03] David McLaughlin, Robert Shapley, and Michael Shelley. Large-scale modeling of the primary visual cortex: influence of cortical architecture upon neuronal response. *Journal of Physiology-Paris*, 97(2-3):237–252, 2003.

[MSSW00] David McLaughlin, Robert Shapley, Michael Shelley, and Dingeman J Wielaard. A neuronal network model of macaque primary visual cortex (v1): Orientation selectivity and dynamics in the input layer 4cα. *Proceedings of the National Academy of Sciences*, 97(14):8087–8092, 2000.

[NES18] NEST simulator, 2018. URL: `http://www.nest-simulator.org/`.

[Neu18] HBP neurorobotics platform, 2018. URL: `https://neurorobotics.net/`.

[NJ90] Scott Nawy and Craig E Jahr. Suppression by glutamate of cgmp-activated conductance in retinal bipolar cells. *Nature*, 346(6281):269, 1990.

[NWNE12] Eivind S Norheim, John Wyller, Eilen Nordlie, and Gaute T Einevoll. A minimal mechanistic model for temporal signal processing in the lateral geniculate nucleus. *Cognitive Neurodynamics*, 6(3):259–281, 2012.

[OB12] Yusuf Ozuysal and Stephen A Baccus. Linking the computational structure of variance adaptation to biophysical mechanisms. *Neuron*, 73(5):1002–1015, 2012.

[PD12] Tobias C Potjans and Markus Diesmann. The cell-type specific cortical microcircuit: relating structure and activity in a full-scale spiking network model. *Cerebral cortex*, 24(3):785–806, 2012.

[PE02] HE Plesser and GT Einevoll. Linear mechanistic models for the dorsal lateral geniculate nucleus of cat probed using drifting-grating stimuli. *Network: Computation in Neural Systems*, 13(4):503–530, 2002.

[PE10] Hans Ekkehard Plesser and Håkon Enger. Nest topology user manual. 2010.

[POR09] Rodrigo Publio, Rodrigo F Oliveira, and Antonio C Roque. A computational study on the role of gap junctions and rod ih conductance in the enhancement of the dynamic range of the retina. *PLoS One*, 4(9):e6970, 2009.

[Rod65] Robert W Rodieck. Quantitative analysis of cat retinal ganglion cell response to visual stimuli. *Vision research*, 5(12):583–601, 1965.

[SCM93] AM Sillito, J Cudeiro, and PC Murphy. Orientation sensitive elements in the corticofugal influence on centre-surround interactions in the dorsal lateral geniculate nucleus. *Experimental Brain Research*, 93(1):6–16, 1993.

[SCSR00] Gregory D Smith, Charles L Cox, S Murray Sherman, and John Rinzel. Fourier analysis of sinusoidally driven thalamocortical relay neurons and a minimal integrate-and-fire-or-burst model. *Journal of Neurophysiology*, 83(1):588–610, 2000.

[SE02] Denis Schluppeck and Stephen A Engel. Color opponent neurons in v1: a review and model reconciling results from imaging and single-unit recording. *Journal of Vision*, 2(6):5–5, 2002.

[SF82] G Sclar and RD Freeman. Orientation selectivity in the cat's striate cortex is invariant with stimulus contrast. *Experimental brain research*, 46(3):457–461, 1982.

[SG01] S Murray Sherman and Ray W Guillery. *Exploring the thalamus.* Elsevier, 2001.

[SH05] Lawrence C Sincich and Jonathan C Horton. The circuitry of v1 and v2: integration of color, form, and motion. *Annu. Rev. Neurosci.*, 28:303–326, 2005.

[SH11] Robert Shapley and Michael J Hawken. Color in the cortex: single- and double-opponent cells. *Vision research*, 51(7):701–717, 2011.

[She79] S Murray Sherman. The functional significance of x and y cells in normal and visually deprived cats. *Trends in Neurosciences*, 2:192–195, 1979.

[SJ02] Adam M Sillito and Helen E Jones. Corticothalamic interactions in the transfer of visual information. *Philosophical Transactions of the Royal Society B: Biological Sciences*, 357(1428):1739–1752, 2002.

[SKAT96] Peter D Spear, Charlene BY Kim, Aneeq Ahmad, and Bryony W Tom. Relationship between numbers of retinal ganglion cells and lateral geniculate neurons in the rhesus monkey. *Visual neuroscience*, 13(1):199–203, 1996.

[SKSN08] Josefin Snellman, Tejinder Kaur, Yin Shen, and Scott Nawy. Regulation of on bipolar cell activity. *Progress in retinal and eye research*, 27(4):450–463, 2008.

[SPLD01] Vivianne C Smith, Joel Pokorny, Barry B Lee, and Dennis M Dacey. Primate horizontal cell dynamics: an analysis of sensitivity regulation in the outer retina. *Journal of Neurophysiology*, 85(2):545–558, 2001.

[Sta18] Stallo supercomputer, 2018. URL: `http://hpc-uit.readthedocs.io/en/latest/stallo/stallo.html`.

[SWT07] Mark M Schira, Alex R Wade, and Christopher W Tyler. Two-dimensional mapping of the central and parafoveal visual field to human visual cortex. *Journal of neurophysiology*, 97(6):4284–4295, 2007.

[TS98] JP Turner and TE Salt. Characterization of sensory and corticothalamic excitatory inputs to rat thalamocortical neurones in vitro. *The Journal of Physiology*, 510(3):829–843, 1998.

[Tsc12] David Tschumperlé. The cimg library. In *IPOL 2012 Meeting on Image Processing Libraries*, pages 4–pp, 2012.

[TSMS04] Louis Tao, Michael Shelley, David McLaughlin, and Robert Shapley. An egalitarian network model for the emergence of simple and complex cells in visual cortex. *Proceedings of the National Academy of Sciences*, 101(1):366–371, 2004.

[UA15] W Martin Usrey and Henry J Alitto. Visual functions of the thalamus. *Annual review of vision science*, 1:351–371, 2015.

[VGDSA08] Werner Van Geit, Erik De Schutter, and Pablo Achard. Automated neuron model optimization techniques: a review. *Biological cybernetics*, 99(4-5):241–251, 2008.

[vH05] Hans van Hateren. A cellular and molecular model of response kinetics and adaptation in primate cones and horizontal cells. *Journal of vision*, 5(4):5–5, 2005.

[Wil89] James R Wilson. Synaptic organization of individual neurons in the macaque lateral geniculate nucleus. *Journal of Neuroscience*, 9(8):2931–2953, 1989.

[WK09] Adrien Wohrer and Pierre Kornprobst. Virtual retina: a biological retina model and simulator, with contrast gain control. *Journal of computational neuroscience*, 26(2):219–249, 2009.

[WNLF98] F Wörgötter, E Nelle, B Li, and K Funke. The influence of corticofugal feedback on the temporal structure of visual responses of cat thalamic relay cells. *The Journal of physiology*, 509(3):797–815, 1998.

[WS16] Qi Wang and Michael W Spratling. Contour detection in colour images using a neurophysiologically inspired model. *Cognitive Computation*, 8(6):1027–1035, 2016.

[WVS$^+$11] Xin Wang, Vishal Vaingankar, Cristina Soto Sanchez, Friedrich T Sommer, and Judith A Hirsch. Thalamic interneurons and relay cells use complementary synaptic mechanisms for visual processing. *Nature neuroscience*, 14(2):224, 2011.

[XOC$^+$15] Dajun Xing, Ahmed Ouni, Stephanie Chen, Hinde Sahmoud, James Gordon, and Robert Shapley. Brightness–color interactions in human early visual cortex. *Journal of Neuroscience*, 35(5):2226–2232, 2015.

[YD07] Nada Yousif and Mike Denham. The role of cortical feedback in the generation of the temporal receptive field responses of lateral geniculate nucleus neurons: a computational modelling study. *Biological cybernetics*, 97(4):269–277, 2007.

[YGLL13] Kaifu Yang, Shaobing Gao, Chaoyi Li, and Yongjie Li. Efficient color boundary detection with color-opponent mechanisms. In *Computer Vision and Pattern Recognition (CVPR), 2013 IEEE Conference on*, pages 2810–2817. IEEE, 2013.

[Zek78] Semir M Zeki. Functional specialisation in the visual cortex of the rhesus monkey. *Nature*, 274(5670):423, 1978.

[ZUL99] JJ Zhu, DJ Uhlrich, and WW Lytton. Burst firing in identified rat geniculate interneurons. *Neuroscience*, 91(4):1445–1460, 1999.

[ZXSS10] Wei Zhu, Dajun Xing, Michael Shelley, and Robert Shapley. Correlation between spatial frequency and orientation selectivity in v1 cortex: implications of a network model. *Vision research*, 50(22):2261–2273, 2010.

[ZZSS15] Shay Zweig, Guy Zurawel, Robert Shapley, and Hamutal Slovin. Representation of color surfaces in v1: edge enhancement and unfilled holes. *Journal of Neuroscience*, 35(35):12103–12115, 2015.

Appendix A

International Journal of Neural Systems, Vol. 0, No. 0 (2015) 1–18
© World Scientific Publishing Company

A COMPUTATIONAL FRAMEWORK FOR REALISTIC RETINA MODELING

Pablo Martínez-Cañada, Christian Morillas, Begoña Pino, Eduardo Ros and Francisco Pelayo*
Department of Computer Architecture and Technology. CITIC-UGR
University of Granada, Spain
{*pablomc,cmg,bpino,eros,fpelayo*} *@ugr.es*

Computational simulations of the retina have led to valuable insights about the biophysics of its neuronal activity and processing principles. A great number of retina models have been proposed to reproduce the behavioral diversity of the different visual processing pathways. While many of these models share common computational stages, previous efforts have been more focused on fitting specific retina functions rather than generalizing them beyond a particular model. Here we define a set of computational retinal microcircuits that can be used as basic building blocks for the modeling of different retina mechanisms. To validate the hypothesis that similar processing structures may be repeatedly found in different retina functions, we implemented a series of retina models simply by combining these computational retinal microcircuits. Accuracy of the retina models for capturing neural behavior was assessed by fitting published electrophysiological recordings that characterize some of the best-known phenomena observed in the retina: adaptation to the mean light intensity and temporal contrast, and differential motion sensitivity. The retinal microcircuits are part of a new software platform for efficient computational retina modeling from single-cell to large-scale levels. It includes an interface with spiking neural networks that allows simulation of the spiking response of ganglion cells and integration with models of higher visual areas.

Keywords: computational retina modeling; large-scale retina model; single-cell retina model; retina simulator; visual adaptation; contrast adaptation; adaptation to the mean light intensity; object motion sensitive cells; space-variant Gaussian filter; low-pass temporal filter; single-compartment model; static nonlinearity; short-term plasticity; spiking neural networks.

1. Introduction

Although the retina is one of the most extensively studied neural circuits in the visual system, from the first findings by Cajal[1] up to the present day, many aspects of retinal connectivity are still controversial and certain functional mechanisms are not entirely clear [2–5]. Retinal cells connect in different and complex neural structures that provide a wide repertoire of visual functions. Numerous computational models have been proposed to accurately predict the different retina functionalities on the response to artificial and natural visual patterns. However, the aim has been to perfectly describe the retina behavior observed in a specific physiological experiment rather than extrapolating results. On the contrary, neural simulation tools such as NEST[6], NEURON[7], BRIAN[8] or GENESIS[9], exploit common properties of neurons (e.g., their ionic-selective channels) to provide researchers with a general and unified framework for neural modeling that facilitates the study of the underlying neural mechanisms.

A remarkable amount of research has also pur-

---

[*] Corresponding author.

sued a generalization of common features of retina processing and unification of different retina models [10–18]. However, these are often ad hoc models whose parameters can be modified but not their retina architecture. Generally, their primary goal is to propose a functional model of the whole retina, though, none of the previously cited models can be fully configured to reproduce different physiological experiments than those they have been intentionally designed for.

We present a new framework for computational retina modeling that is based on interconnection of basic processing modules to reproduce different retina behaviors. Our work addresses the following issues with the ultimate purpose of validating, by computational simulations, the hypothesis that a few retinal structures may be repeatedly involved in different retina functions:

- *Computational retinal microcircuits.* There exist sufficient examples of single neural structures that play quite different roles in the retina processing to motivate the generalization of basic retinal building blocks[3]. We implemented a set of computational retinal microcircuits at different abstraction levels that have been recurrently used in the literature for modeling different stages of the retina. We show that different retina models can then be simulated by creating and combining these circuits to form different retina architectures. To the best of our knowledge, this idea, inspired by neural simulators, of computational retinal microcircuits as basic building blocks is a novel concept in retina modeling.
- *Functional and biologically accurate models.* Although we employed more detailed processing microcircuits (e.g., a single-compartment model) in some retina stages to better fit electrophysiological recordings, our main objective was to provide functional models and descriptions as simple as possible to describe the retina phenomena. Moreover, the focus of this framework is on generalizing and summarizing the computational basis of retina modeling, and therefore this premise goes against any specificity in the model description. In spite of the constraints that such an approach raises, we achieved a remarkable level of biological accuracy, comparable to some of the most accurate retina models proposed heretofore [19; 20].
- *Association of every retina stage with a plausible biological mechanism.* Amongst models of retinal processing as a whole, some of them focus on a more functional modeling of every retina stage [10; 12] and other models include some stages that have a stronger relationship to biophysical properties, while some fixed processing behaviors are assumed for the rest[19; 15]. Some of the latter models use multi-state kinetic modules that group together different components of the retina behavior (e.g., fast and slow components of temporal contrast adaptation) and may blur the understanding of the biological mechanisms underlying different retina stages[19]. In contrast, the retina models we developed using the computational retinal microcircuits, connect every retina stage with a plausible biological mechanism in accordance with other authors [11].
- *Retina simulation software interfaced with spiking neural networks.* To provide researchers with a simulation tool that reflects all these concepts, we developed a new software platform for efficient computational retina modeling, called COREM. Computations of spatiotemporal equations performed by retinal microcircuits take advantage of recursive filtering techniques and multithreading. COREM uses a time-driven simulation approach to update functions that describe neuron membrane potential and synaptic currents. An interface with spiking neural network simulators allows generation of the spiking response of ganglion cells. The retina model can be easily loaded in the script of the neural network simulator as an extension module, facilitating its connection to models of higher visual areas, such as the Lateral Geniculate Nucleus (LGN) and the visual cortex.

2. Computational retinal microcircuits

In spite of the wide variety of existing retinal cells (there are more than 50 clearly distinct cell types) some neural circuits are encountered repeatedly in many different retina behaviors[3]. This suggests functionality arises from connectivity of the neural network and not so significantly from features of every individual cell. Moreover, after an extensive review of the literature about retina modeling, we observed that some computational algorithms have been repeatedly used to explain different properties of the retina processing (e.g., a Gaussian filter to characterize the receptive field of a cell, as discussed below).

We made a selection of 5 computational microcircuits (Fig. 1) that can be combined to reproduce single-cell and large-scale retina models at different abstraction levels. They can be classified as block-structured models, block-compartment models and single-compartment models according to the scheme proposed by Guo *et al.*[4]. With this set of microcircuits our aim was to summarize the basic principles of the retina modeling and embrace some of the most significant algorithms proposed in the literature, without going into depth on the description of the neural morphology.

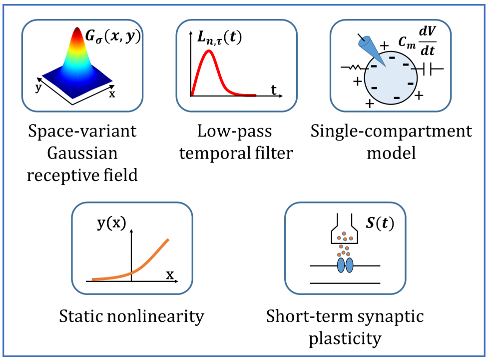

Fig. 1. Computational retinal microcircuits that are used as basic building blocks within COREM. They consist of one spatial processing module, a space-variant Gaussian filter, two temporal modules, a low-pass temporal filter and a single-compartment model, a configurable time-independent nonlinearity and a STP function.

2.1. *Space-variant Gaussian receptive field*

Since the early studies of the cat retinal ganglion cells by Enroth-Cugell [21], the Gaussian filter has become the model of the retinal receptive field par excellence. Sensitivity of the antagonistic center-surround receptive field of ganglion cells is often described by a Difference of two Gaussian kernels, called DOG, with different space constants. However, some cells show a more complex receptive structure than a simple DOG model and different combinations of Gaussian filters are proposed to capture the neural response more accurately[22–24].

At single-cell level, a Gaussian kernel is used to approximate the biophysics of spatial synaptic integration through dendrites of retinal cells and also electrical couplings between neighboring cells. The computational operation underlying these biological mechanisms can be interpreted in terms of a spatial averaging of the neural signal. The mathematical formulation is a two-dimensional isotropic Gaussian filter, $G_\sigma(x, y)$, of space constant σ.

To counterbalance the low density of cells in the periphery of the retina, the receptive field of cells increases with eccentricity. This retina property is modeled by a space-variant Gaussian filtering scheme that gradually blurs out details as the radial distance to the fovea increases (as shown in Fig. 2).

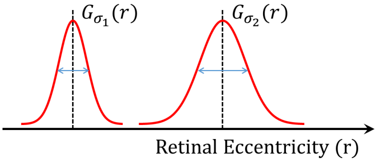

Fig. 2. Increase in kernel size of the Gaussian filter that simulates the change of the receptive field with eccentricity. Coefficients are recurrently computed at each pixel by using a Deriche's recursive filtering adapted to the space-variant case by Tan *et al.*[25]. Amplitude and phase distortion at the right boundary of the image is fixed by including the algorithmic modification by Triggs *et al.*[26].

The traditional convolution algorithm has to deal with two implementation issues: first, a Gaussian convolution is a computationally expensive operation that critically limits the performance of the simulator and, on the other side, in a space-variant approach the convolution kernel is different at each pixel. Our software performs a Deriche's recursive filtering[27; 28], which approximates the Gaussian kernel, and has been extended to the space-variant case described by Tan *et al.*[25].

Other retina simulators[11] also include a space-variant Deriche's filtering although a second order smoothing function[27] is preferred to reduce the processing time over a more realistic Gaussian approximation. In addition, the inherent amplitude and phase distortion produced by this type of recursive filtering at the right boundary of the image is fixed by embodying the corrected version by Triggs *et al.*[26]. When running the simulation in a multicore computer we also take advantage of the fact that every row and every column of the image are processed independently and can be executed in different threads to parallelize simulations.

2.2. *Low-pass temporal filters*

Low-pass temporal filters have been often used to model synaptic delays and temporal membrane integration of synaptic currents[29; 15; 20; 30; 11; 31]. The standard equation describing the impulse response of a low-pass filter with time constant τ is:

$$L_\tau(t) = \frac{\exp(-t/\tau)}{\tau} \tag{1}$$

Multiple distributed low-pass stages occur along the retinal pathway. Moreover, some single cells already integrate several low-pass filters. An example is the phototransduction cascade at photoreceptors, which roughly includes three processing stages: the outer segment transduction cascade, inner segment ion channel interactions and interactions in the cone pedicle. A cascade of low-pass filters can be expressed in a compact format:

$$L_{n,\tau}(t) = \frac{(nt)^n \exp(-nt/\tau)}{(n-1)!\tau^{n+1}} \tag{2}$$

If $t > 0$, and zero otherwise (causal filters). Temporal low-pass filters also use a recursive approach. We decided to employ an implementation of temporal filters that is based on the Infinite Impulse Response (IIR) approach by Virtual Retina[11], which requires less memory and calculations than a similar Finite Impulse Response (FIR) filter. In this type of filtering, preceding output values, $Y(k-i)$, are used in the calculation of the new output values, $Y(k)$, at the current time step k:

$$Y(k) = \sum_j b_j X(k-j) - \sum_i a_i Y(k-i) \tag{3}$$

where $X(k-j)$ are the preceding input values. Coefficients a_i and b_j are calculated for each filter according to the equations provided in the above-mentioned publication[11].

2.3. *Single-compartment model*

Single-compartment models such as the classic Hodgkin-Huxley model[32] neglect the neuron's spatial structure and focus entirely on how its various ionic currents modulate the subthreshold response[33]. Thus, spatial description of a neuron is simplified to a point neuron and its membrane potential represented by a single variable, V. The basic equation for a single-compartment model is[34; 35]:

$$C_m \frac{dV(t)}{dt} = \sum_i I_i(t) + \sum_j g_j(t)(E_j - V(t)) \tag{4}$$

where C_m is the membrane capacitance, $I_i(t)$ represent external currents (e.g., electrode currents or synaptic inputs), $g_j(t)$ are conductances of ionic channels (including a leak conductance) and E_j their reversal potentials. Provided that the simulation step Δt is sufficiently small, numerical integration of the single-compartment model is approximated by the Euler method[34; 36]:

$$V(t+\Delta t) = V_\infty + (V(t) - V_\infty)\exp(-\Delta t/\tau_V) \tag{5}$$

with

$$V_\infty = \frac{\sum_j g_j(t)E_j + \sum_i I_i(t)}{\sum_j g_j(t)} \tag{6}$$

and

$$\tau_V = \frac{C_m}{\sum_j g_j(t)} \tag{7}$$

Most of the interesting electrical properties of neurons arise from nonlinearities associated with changes of membrane conductances over time[34]. Models of membrane conductances describe the probability that a channel is in an open, ion-conducting state at any given time. This probability, formulated in terms of gating equations, depends on the time course of membrane potential (for a voltage-dependent conductance), the presence or absence of a neurotransmitter (for a synaptic conductance), or other factors such as the concentration of calcium (for a calcium-dependent conductance).

Our interest in modeling membrane conductances lies in their functional properties to implement intrinsic and inter-cell mechanisms of feedback that allow gain control of the neural signal. Therefore, a rapid increase in the membrane potential of a cell, as an example, would elicit a proportional rise in the value of a voltage-dependent conductance $g_j(t)$, which would produce the consequent decrease of the neural gain $dV(t)/dt$ (Eq. 4). In the same manner, $g_j(t)$ defines the time constant τ_V of the single-compartment model and accounts for adaptive changes of the dynamics in the cell processing (Eq. 7). A gain control serves a dual purpose by adapting the dynamic range of the visual pathway, avoiding response saturation, and protecting the cell from quick and large synaptic currents that could damage its internal structure.

Besides our implementation, which provides a description of this feedback mechanism based on changes in membrane conductances, many other retina models also use a feedback component to explain neural gain control in early stages of the visual system. This mechanism is sometimes also called shunting inhibition, divisive feedback or neural normalization[37]. There are several models that reproduce the phenomenon of contrast gain control in the retina[38; 11; 15], LGN[39], and primary visual cortex[40]. Other models also include a feedback loop to simulate adaptation to the mean light intensity[41; 20] or directional selectivity to motion [42; 43]. We can also find models in silicon of gain controls that reproduce wide-field motion-sensitive neurons[44].

2.4. *Static nonlinearity*

Some common time-independent transformations of the neural signal, such as polynomial, rectification or sigmoidal transformations (Fig. 3), are accounted for by a configurable static nonlinearity. A static nonlinearity captures the input-output relationship between synaptic input of a neuron and its postsynaptic response. They are used to introduce some important signal corrections performed by neurons (e.g., thresholds and saturation) into accurate estimates of neural responses[34; 45].

A static nonlinearity is one of the two different processing stages described by the well-known Linear-Nonlinear (LN) analysis[46–50]. In this scheme, the input stimulus is convolved with a linear temporal filter and the result is transformed by a static nonlinearity to the neuron's response. The linear filter represents the temporal relationship between the stimulus and the neuron's response, whereas the nonlinearity represents the instantaneous mapping between the filtered stimulus and the response.

Within the different transformations implemented, a rectification function prevents the predicted neural response (and the firing rate in the case of ganglion cells) from becoming negative:

$$y_{x>thr}(x) = ax + c \tag{8}$$

If needed, a saturating nonlinearity can be included, and a sigmoidal function is often used for this purpose:

$$y(x) = \frac{b}{1+\exp(-ax+c)} \tag{9}$$

Other polynomial transformations, used to model, for example, convex functions of a contrast feedback mechanism[11], are defined by:

$$y(x) = ax^b + c \tag{10}$$

in which, a, b and c are configurable parameters that can be tuned to fit a specific neural transformation.

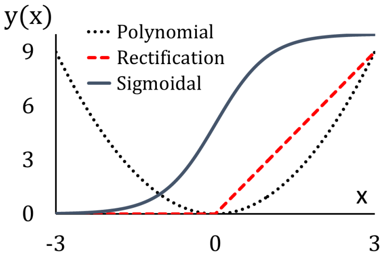

Fig. 3. Functions that represent the main nonlinearities that can be configured in COREM: polynomial, rectification and sigmoidal (apart from the other two nonlinearities not cited in the text but also implemented: threshold function and a piecewise function). Parameters of these functions and x values have been arbitrarily chosen to provide a graphical example.

2.5. *Dynamic nonlinearity with short-term synaptic plasticity*

Short-term plasticity (STP) refers to a phenomenon in which synaptic strength changes over time in a way that reflects the history of presynaptic activity and it lasts from milliseconds to tens of seconds[51; 34; 52]. There are two types of STP, with opposite effects on synaptic efficacy, which are known as short-term depression and short-term facilitation. The main type of adaptation observed in the retina is depression (although another forms of plasticity are also reported[31]) and it is caused by depletion of neurotransmitter release when a strong input stimulus is maintained over time.

Our main motivation to implement a plasticity microcircuit lies in recent findings hypothesizing that depression at the bipolar-to-ganglion cell's synapse is responsible for retinal adaptation to contrast[53–55] and object motion[56]. We propose a STP function that modulates the baseline of the bipolar cell's output response, at the bipolar-to-ganglion cell's synapse. It mainly affects the static nonlinearity of the LN analysis by shifting its offset and accounts for the two different forms of adaptation studied for contrast and object motion, fast (smaller than 100 ms) and slow (in the range of a few seconds).

To reproduce fast adaptation timescale, our STP model implements a simple updating rule based on cell's presynaptic activity, which is used in spiking network models and has been adapted to the analog neural processing of the retina[34]. Assuming the input function is normalized to have zero mean, the offset $S(t)$ is continuously augmented an amount proportional to the variance of the input:

$$S(t) = S(t) + k_f(k_s(t)|input(t)| - S(t)) \tag{11}$$

where k_f is a parameter that specifies the fast adaptation rate and $k_s(t)|input(t)|$, with $k_s(t)$ the slow adaptation term (explained below), limits the maximum value the offset can reach. The term $|input(t)|$ provides a rectified measure of the input synaptic activity.

Over the period of slow adaptation, the baseline shows an exponential decay and recovery for steady input patterns of high and low contrast respectively[48; 55; 57]. The slow recovery of the membrane offset following high contrast stimulation is often called prolonged membrane after-hyperpolarization (AHP). Synaptic depression explains slow adaptation, not only in the retina but also in the visual cortex[58; 59]. We adapted the basic first-order differential equation that is widely used in neural dynamics to describe transitions between different neural states (e.g., active and inactivated states in the four-state system by Ozuysal and Baccus[19]). Slow system transitions during prolonged periods of low and high contrast are governed then by the following equation:

$$k_s(t+\Delta t) = k_\infty(t) + (k_s(t) - k_\infty(t))\exp(-\Delta t/\tau_s) \tag{12}$$

where τ_s is the temporal constant of the slow adaptation mechanism and $k_\infty(t)$ is inversely modulated by the input activity scaled by a plasticity factor k_d:

$$k_\infty(t) = \frac{k_d}{|input(t)|} \tag{13}$$

3. Overview of COREM

The retinal microcircuits described above are implemented in COREM, a configurable C++ retina simulation software. Our two goals when designing COREM have been to provide scientists with a rapid prototyping tool for retina modeling, which facilitates the study of low-level visual mechanisms, and to optimize efficiency of all its modules. An example of this optimization effort is reflected in computations of spatiotemporal equations performed by the space-variant Gaussian receptive field and the low-pass temporal filter. Both modules are formulated as recursive filters and, besides, we employ OpenMP to gain thread-level parallelism in the Gaussian filter (see Section 2 for further details). On the other hand, unlike a conventional neural simulator, layers of neurons in the retina are handled as images (using CImg library[60]), with all the benefits that this entails, such as simultaneous access to internal variables of multiple neurons in a SIMD processor.

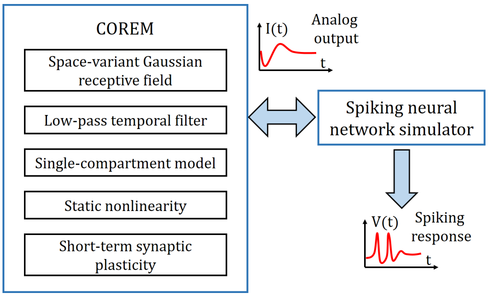

Fig. 4. Interface of COREM with a spiking neural network simulator. While COREM sends data of the analog presynaptic current of ganglion cells, the ganglionar spiking response is reproduced by the spiking neural network simulator.

The modular structure of COREM allows for more flexibility of use than other retina simulators[10; 11]. The user can create and connect any number of computational retinal microcircuits by configuring a simulation script that follows a similar syntactic structure of the neural simulator scripts. Computational retinal microcircuits do not represent specific neuron types but rather basic retina operations that can be combined to reproduce the behavior of single neurons or networks of neurons. We formulated these units in this manner to endow the simulation software with a higher configurability that allows implementation of different retina models. Moreover, built-in tools for visual stimulation and data analysis give the possibility to reproduce some of the most common experimental setups used in electrophysiology of the retina (e.g., sinusoidal drifting gratings or uniform white flashes). Visual stimulus functions, as well as methods for data analysis, were implemented according to the descriptions given in publications referenced in Section 4.

Equations of neuron dynamics are updated in a time-driven fashion consistent with the analog processing architecture inherent to the retina. COREM does not provide retinal microcircuits to explicitly generate the spiking response of ganglion cells. Instead, an interface with spiking neural network simulators allows bidirectional communication with them to simulate firing mechanisms (see Figure 4). Thus, when connecting COREM with a spiking neural network simulator, simulation is driven by the latter one, which periodically sends update requests and receives data of the analog presynaptic current of ganglion cells. Ganglion cells can be simulated as simple integrate-and-fire or more complex models of spiking neurons[62] in the neural network simulator. Integration with models of higher visual areas is therefore carried out by simply instantiating COREM as an extension module in the script of the neural network simulator.

4. Simulation results of electrophysiological experiments

To show the potential of the proposed framework, we constructed three different retina models that describe some well-known properties of the retina processing (see Figure 5), and we fitted them to published electrophysiological recordings. Our contribution in this aspect has been to adapt and combine some representative models proposed in the literature so that they can be implemented using the computational microcircuits described in Section 2.

Consistent with the premise of repeatability in the retina processing pathway[3], our retina models comprise some processing steps that are common to all of them. For example, a divisive feedback loop is present in many stages of different models, such as the inner segment of the cell's model for adaptation to the mean light intensity in Figure 5A, and bipolar cells of the contrast gain control shown in Figure 5B.

Inspired by the numerous approaches that have been proposed for describing the different retina functions, these retina models provide a simple but biologically realistic description of the retina processing. We wanted them to be sufficiently representative and general with the aim of including most of the concepts that characterize retina computations.

4.1. *Adaptation to the mean light intensity*

The visual system routinely copes with the problem of processing the high dynamic range of light intensities in natural environments by regulating sensitivity to light at early stages of visual processing. This dynamic range is obtained mainly by gain control mechanisms that adjust the cell's dynamics to the steady illumination level. Although post-receptor adaptation has been also reported, the outer retina is suggested to be the major locus for adaptation to the mean light intensity[30; 63; 64]. We simplified and adapted the molecular model of cones and horizontal cells proposed by van Hateren[20] to fit electrophysiological data obtained from horizontal cells of the macaque retina[30].

4.1.1. *Model of cones and horizontal cells*

Figure 5A shows a model of the cone photoreceptor, which comprises the outer segment (phototransduction and calcium feedback) and the inner segment, coupled to a horizontal cell's feedback mechanism. The first stage reproduces the temporal low-pass filtering followed by a static nonlinearity of phototransduction by cones. A cascade of first-order low-pass filters is commonly used as initial stage in different models of retinal light adaptation to approximate the retina response when the mean light level is low[65; 41; 30; 66]. In other words, this initial low-pass filtering is the low-light limit of the temporal frequency response.

By contrast, when the mean light level increases, gain at low frequencies is inversely proportional to the mean light level. Divisive feedback[20; 65; 41] and feedforward[67; 63] gain controls have been proposed to shape this adaptation phenomenon. Some authors noted that feedback gain controls tend to be too slow to account for measured cell's response[63]. However, it was demonstrated that an inhibitory feedback split into three stages, calcium feedback, inner segment and horizontal cell's feedback, gives a remarkable

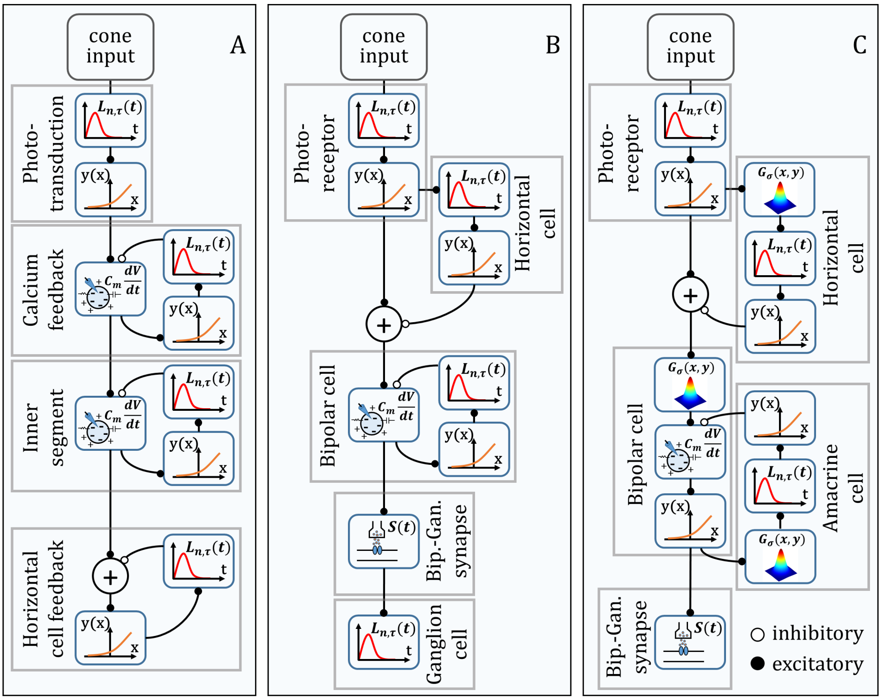

Fig. 5. Retina models implemented by connection of the retinal microcircuits described in Section 2. They reproduce adaptation to the mean light intensity (A) and to temporal contrast (B), and differential motion sensitivity (C). Interconnections are either sign preserving (excitatory, black circles) or sign inverting (inhibitory, white circles). A circle with the plus sign (+) represents linear addition of neural signals. Feedback mechanisms formed by a single-compartment model, a static nonlinearity and a low-pass temporal filter connect the input from the preceding retina stage to the current port ($I_i(t)$ in Eq. 4) and the feedback branch to the conductance port ($g_j(t)$ in Eq. 4). Thus, conductance of the single-compartment model is modulated by the feedback signal. Cone inputs correspond to the transformation that maps the input visual stimuli to the cone spectral sensitivities by using the Hunt-Pointer-Estevez (HPE) matrix [61]. For these experiments, the type of cone (L, M or S) is not specified because a spatially uniform achromatic stimulus is employed.

good fitting and better reflects the inherent biology of photoreceptors and horizontal cells[20].

While formal definition of some of the different feedback loops proposed in our retina models includes a calcium-dependent mechanism (e.g., the calcium feedback in the model presented here or the intrinsic adaptive mechanism at bipolar cell level in Figure 5B), we have implemented them using a single-compartment model and a feedback conductance that resembles a voltage-gated conductance. Calcium- and voltage-dependent conductances can be roughly described by the same set of equations, although physiological interpretation of their parameters is different[34; 35]. In a calcium-dependent system, the adaptive conductance would depend on the concentration of calcium inside the neuron instead of a direct relationship with its membrane potential. Calcium-activated channels are opened by increases in concentration of intracellular calcium occurring during synaptic transmission. Thus, a rise of calcium influx produces an increase of the calcium-dependent conductance that feedbacks the current neural state and results in a similar gain control of the neural system.

In the model, the calcium feedback pathway consists of a low-pass filter with a small time constant (5 ms) and a polynomial static nonlinearity that modulates strong feedback by using an exponent of value 4 (both time constant and exponent values are comparable to τ_c and n_c in the model by van Hateren[20]).

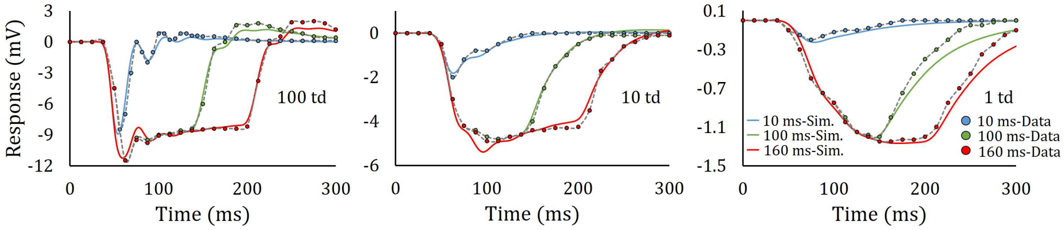

Fig. 6. Simulation results for the model of adaptation to the mean light intensity (color solid lines) and electrophysiological recordings (color markers) obtained from horizontal cells of the macaque retina[30]. Data points have been sampled from Figure 6 in the publication[30]. Input stimuli are spatially uniform white pulses of 10, 100, and 160 ms at a fixed Weber contrast of 8 and background illuminances of 1, 10 and 100 trolands. All pulses start at 0 ms. A gray dashed line has been used to interpolate electrophysiological data and improve visualization.

Much of the adaptation process is rapidly driven by the calcium feedback, which is mainly responsible for reducing the response gain. The inner segment feedback has a higher time constant and an exponent of value 2 to follow up finer adaptation features (e.g., resonant oscillations in the impulse response, represented in Fig. 6). A linear subtractive scheme is used for the horizontal feedback shown in the last stage of Figure 5A.

While modeling similar feedback architectures for the inner segment and horizontal cells, we have largely simplified the circuitry proposed by van Hateren[20] and slightly modified their roles in the adaptation process. A divisive feedback loop, such as the inner segment feedback, can be easily tuned to produce high-frequency oscillations, which represents a simpler design approach. On the other hand, a linear subtractive scheme at the horizontal cell's level, which doesn't include complex nonlinear components, is consistent with the slow linear inhibition performed by horizontal cells and implemented also in the rest of retina models.

4.1.2. *Responses to pulses*

Figure 6 shows simulated and measured responses to uniform white pulses of 10, 100, and 160 ms at a fixed Weber contrast of 8 and background illuminances of 1, 10 and 100 trolands (td). The model fittings (red, green and blue solid lines) were made to all stimulus conditions simultaneously, and are generally quite good approximations, considering the wide range of stimulus conditions. Details of multiobjective parameter fitting of the model are given in appendix A.

It is possible to identify the main stages of the model responsible for various aspects of the response shapes. The calcium feedback plays a key role in gain control, preventing the response from scaling proportionally with the background luminance. It may be noted that high-frequency oscillations due to the inner segment feedback, shown at the onset and removal of the stimulus, are more prominent for a 100 td background and nearly imperceptible for the 1 td background. At low mean light intensities the inner segment cannot produce a strong feedback and its effects are less prominent, compared to the previous stage, because of the lower value of the exponent in the static nonlinearity. Slow decrease in the steady response and rebounds after stimulus removal are motivated by the linear horizontal cell's feedback.

4.1.3. *Responses to sinusoidal gratings*

By using the same model parameters of the previous experiment, a new stimulus is simulated to represent sensitivity as a function of frequency and background illuminance (see Figure 7). For each background illuminance, temporal frequency of a low-contrast sinusoidal grating, at three different background illuminances (10, 100 and 1000 td) is progressively increased and the response amplitude divided by the background illuminance to calculate sensitivity (in mV/td) at different frequencies.

The model captures the main features of the experimentally measured response[30] and simulated responses resemble those obtained in other models[20]: a decrease of responsivity as a function of the background level for low frequencies, and asymptotic convergence at high frequencies; an increase of the cutoff frequency as a function of background level; and a resonance peak at higher frequencies, particularly visible at the 100 and 1000 td background levels.

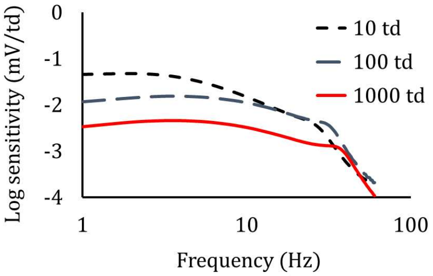

Fig. 7. Logarithm of the amplitude sensitivity of the simulated model (in mV/td) plotted as a function of the grating frequency for different background illuminances (10, 100 and 1000 td). Physiological recordings are not included in this figure because authors[30] do not provide an averaged inter-cell response that could be used as optimization target. Our results reproduce remarkably well all features of the neural behavior (e.g., cutoff frequency) and simulated values are within the range of measured values for the different cells.

4.2. *Fast and slow temporal contrast adaptation*

Adaptation to the variance of light intensities is known as temporal contrast adaptation. After a change in contrast, retinal cells express at least two adaptive mechanisms: a fast change in the response occurs within the first tens of milliseconds and a slow component over some tens of seconds following the contrast switch[48; 46; 68]. When the stimulus environment changes from a low to high variance, temporal filtering quickly accelerates, sensitivity decreases, and the average response increases. For a high-contrast pattern maintained over time, a slow decay in the average response is produced that opposes the fast change in the cell's baseline. Upon a decrease in contrast, all these changes reverse direction. The time constants for slow adaptation are asymmetric, with the baseline decaying faster in high contrast than it rises in low contrast[48; 19].

Contrast adaptation originates in bipolar cells and neither photoreceptors nor horizontal cells are involved in the process [69; 46]. Some experiments have shown that contrast adaptation effects are still present under physiological blockade of amacrine synapses, ruling out a critical role for amacrine cells in driving contrast adaptation [69; 47]. Slow adaptation mechanisms are apparently driven by prolonged reduction of glutamate release at the bipolar-to-ganglion synapse[53–55]. Gain of spike generation at the level of ganglion cells adapts to contrast by slow inactivation of voltage-dependent Na^+ channels[70; 48]. Recordings in bipolar cells suggested that another intrinsic gain control mechanism lies in the bipolar cell dendrites and depends on calcium feedback[47; 54].

Our goal was to accurately predict intracellular recordings of ganglion cell's membrane potential[19] by capturing all adaptive features of temporal filtering and the static nonlinearity in the LN analysis. Gain control in the subthreshold response of ganglion cells originates from gain control of its excitatory bipolar cell inputs[69]. We implemented an intrinsic mechanism for gain control at the level of bipolar cells, which can account for most of the fast-onset contrast adaptation[46; 47], and another mechanism of STP at the bipolar-to-ganglion synapse[55].

4.2.1. *Retina model*

Figure 5B shows a whole retina model that accounts for fast and slow contrast gain control. The first stage is a linear subtraction at the Outer Plexiform Layer (OPL) to represent the well-known opposition between the center of the receptive field, driven by photoreceptors, and the surround signal transmitted by horizontal cells. In the time domain, a biphasic impulse response results from subtraction of photoreceptor signal and its delayed version by horizontal cells, and this is the characteristic temporal shape observed throughout all retina stages. We decided to implement this OPL model, rather than using a predefined linear filter[19], because each of its components has direct connection with biological mechanisms. Note that the center-surround structure at OPL is repeated for the other retina models in Figure 5 but including spatial filtering modules (i.e., Gaussian filters) that have been omitted here since they are not relevant for the processing of a spatially uniform stimulus.

Bipolar cells implement a contrast gain control based on a divisive feedback loop[11; 39; 15; 38] and may be associated with the calcium-dependent mech-

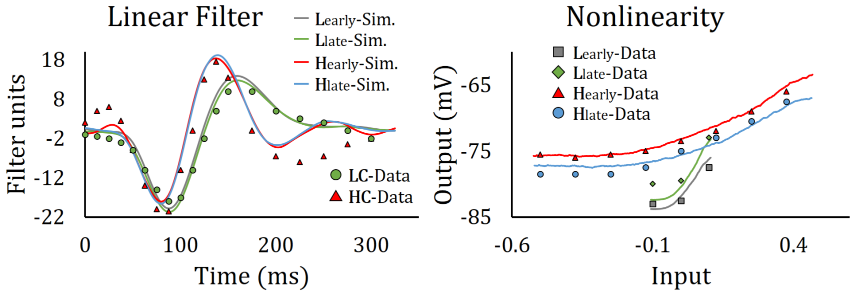

Fig. 8. LN analysis of the simulated response of the model for contrast adaptation (solid lines) fit to intracellular recordings (color markers) of salamander ganglion cells[19]. Data points have been sampled from Figure 3 in the publication[19]. Four different contrast intervals are considered in the average of measurements: L_{early} corresponds to the first 10 seconds after a low contrast step and L_{late} to the period from 10 to 20 seconds after a low contrast step. H_{early} and H_{late} are defined similarly for a high contrast step. LC refers indistinctly to L_{early} and L_{late}. Similarly for HC. They are used in the linear filter because measured curves over the contrast periods are identical. The input stimulus is an alternating spatially uniform sequence of high and low contrast periods of 20 s. Values of the sequence are chosen every 5 ms, which corresponds to the simulation step, from a Gaussian probability distribution with normalized mean intensity 0.5. Contrast, defined as the quotient between standard deviation and mean intensity of the Gaussian distribution, was 0.1 for low contrast patterns and 0.5 for high contrast patterns. We have followed the correlation method described by Baccus and Meister[46] to generate results of the LN analysis.

anism observed in the bipolar cell dendrites[47]. Neural state of bipolar cells is driven by the local measure of contrast provided by the OPL signal. The feedback pathway rectifies and amplifies the current neural signal of bipolar cells to continuously modify an adaptive conductance of the single-compartment model, in a similar manner to other approaches for contrast adaptation[11; 39]. An increase of the adaptive conductance has the double effect on bipolar cells of reducing its neural gain $dV(t)/dt$ (Eq. 4) and decreasing the temporal constant τ_V (Eq. 7). Thus, a stimulus switch to high contrast decreases sensitivity and accelerates temporal filtering of bipolar cells.

Most of retina models for contrast gain control do not reproduce all adaptive features of the static nonlinearity in the LN anlysis[11; 39; 38; 15]. By introducing a STP at the bipolar synaptic terminal our goal was to reproduce offset changes in the bipolar cell's response. The main effects that are modeled by the STP module are a fast increase in the response to the onset of high contrast adaptation, slow decay of the response for a maintained high-contrast pattern and the consequent membrane AHP recovery afterwards.

4.2.2. *LN analysis of ganglion cell's membrane potential*

Figure 8 compares the LN analysis of simulation results and intracellular recordings of salamander ganglion cells[19]. We have presented results of a preliminary version of this retina model in Ref. 71, 72. Here, parameters of the model in Figure 5B have been optimized for fitting simultaneously to both the linear filter and the static nonlinearity (see appendix A). The model captures fast adaptation changes in the temporal filter: a high contrast step decreases the time to peak with a consequent acceleration of the neural dynamics, and makes the temporal response more differentiating. Fast adaptation changes are also observed in the static nonlinearity by a decrease of the sensitivity, which is defined as the average slope of the nonlinearity, and a quick depolarizing offset, as measured by the increase of the average value. Slow adaptation mainly affects the offset of the static nonlinearity, by decreasing it during a high contrast period and motivating its slow recovery after a switch to low contrast (Figure 9).

Experimentally we observed that gain control at bipolar cells can be understood as a push-pull mechanism between the OPL biphasic signal and feedback response. A weak feedback would result in a perfect fit of the OPL biphasic shape (characterized by the first negative peak and maximum value of the linear filter within the first 150 ms in Figure 9) and a complete removal of the second minimum reflected in the measured data (after 200 ms). By contrast, an increase in the feedback signal would worsen approximation of the first negative peak and pull the response after 150 ms towards this second minimum. Since both minimum values of the linear filter cannot be perfectly fit simultaneously we present a trade-off solution by a multiobjective optimization that slightly deviates from measures of late values in the high-contrast curve but produces a fairly well fitting of the rest of curves.

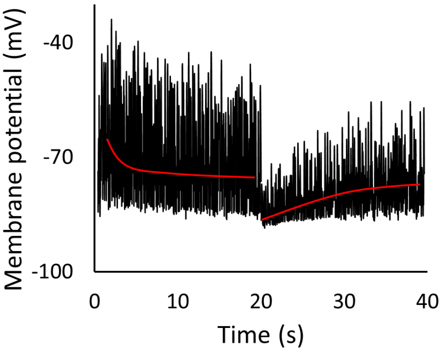

Fig. 9. Simulated membrane potential of ganglion cells over time. In this figure, the first 20 s correspond to a high contrast period and the following 20 s to a low contrast period. The red solid line approximates the offset of the neural response. The contribution of two distinct temporal components, fast and slow, to the onset of high contrast adaptation is suggested by asymmetric time courses of the different contrast periods. Fast adaptation changes are more significant for an increase in contrast, which results in a peak of the membrane potential after a contrast switch (at 0 s). A slow decay in the membrane potential is produced afterwards. By contrast, when a low contrast step occurs (at 20 s), AHP restores the baseline and opposes previous changes. This figure has been adapted from Figure 3 in a previous publication[71].

One of the most detailed retina models for contrast adaption, which also reproduces all adaptive features, has been proposed by Ozuysal and Baccus[19]. In their model, the late values of the high-contrast are approximated by a flat response of the system (Figure 3 of the publication[19]), whereas our model shows somehow a tendency to reproduce this rebound of the measured neural response. Strong oscillations of the high contrast curve do not represent the neural response of all cells measured but they often appear in cells that strongly adapt to contrast[73; 46]. We could hypothesize that another adaptive mechanism (e.g., a second feedback stage with different time constants), which activates for high contrast stimuli, could account for this negative rebound.

4.3. *Object motion sensitive (OMS) cells*

The visual task of detecting objects moving within a scene is not a trivial task. Image motion on the retina can be produced by two different reasons. One is the movement of objects in the scene. The other results from self-motion, such as translation when walking or movements of the head, and eye movements, large gaze-shifting eye movements and the incessant fixational eye movements.

To detect moving objects, a type of ganglion cells, referred as object motion sensitive cells (OMS), distinguish differential motion, between the receptive field center and surround, from the global retinal image drift[74; 56; 75]. An OMS ganglion cell remains silent under global motion of the entire image but fires when the image patch in its receptive field moves differently from the background. To accommodate all kinds of observer motion, this selectivity for differential motion does not depend on direction of motion, nor the image pattern, only on the speed.

4.3.1. *Retina model*

Our retina model (Figure 5C) is a computational implementation of previous models[74; 75] that includes as a novelty the STP microcircuit at the ganglion cell's synaptic input to produce differential motion adaptation. In this model, ganglion cells pool neural signals within its receptive field from many retinal structures formed by the bipolar cell's processing pipeline shown in Figure 5C (the Gaussian filter at ganglion cell's synapse is not represented in this figure). One can identify two key components that modulate the OPL biphasic response from photoreceptors and horizontal cells and account for differential motion detection in the subthreshold response of ganglion cells. The first one is formed by spatial pooling of rectified responses of bipolar cells. It ex-

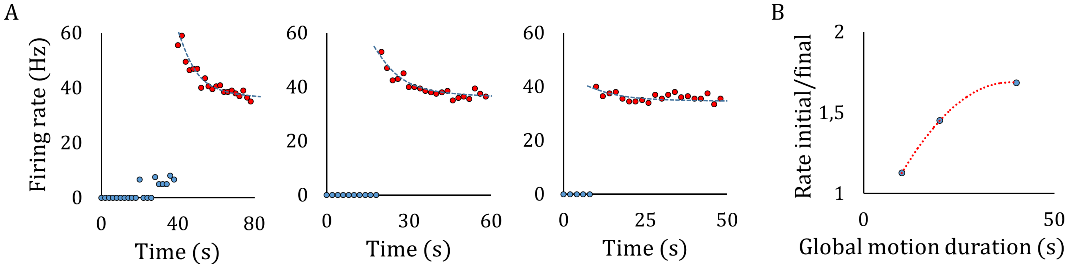

Fig. 10. (A) Simulated firing rates of OMS cells in response to a jittering grating alternating between 40 s of differential motion (red markers) and a varying interval of global motion (blue markers). A dashed blue line interpolates simulated values for the differential motion interval. Global motion corresponds to the first 40 s in the first graph, 20 s in the second and 10 s in the last graph. (B) Firing rate at the onset of differential motion divided by the final value of this interval, plotted as a function of the preceding duration of global motion (B). The jittered gratings consisted of black and white bars with a spatial periodicity of 0.57 degrees of retina visual angle. The object region (a circle) was 1.14 degrees in diameter and the whole retina surface simulated encompassed 5.7 degrees. The jitter trajectory was generated by stepping the background and object gratings periodically in 1D every 15 ms with a step size of 0.029 degrees, synchronously for global motion and asynchronously for differential motion. The retina model is connected with NEST[6] to simulate leaky integrate-and-fire ganglion cells and generate the spike train data. Parameters of the model have been tuned manually to approximate the neural behavior, assuming firing rates which would be registered for a single trial, of Figure 2 in the publication by Ölveczky *et al.*[56].

plains the fact that OMS cells respond to gratings much finer than the receptive field center, and independently of the phase of the grating[76].

The second important computational property of the OMS circuit arises in this model from background inhibition, possibly driven by polyaxonal amacrine cells, of the central region of the ganglion receptive field. Both the excitatory signal from bipolar cells and inhibition from amacrine cells are delivered to ganglion cells in a sparse sequence of transient pulses, which correlate with shifts of a jittering motion stimulus. Thus, if the background trajectory matches the object trajectory in the center of the receptive field, inhibition and excitation synchronize and the OMS ganglion cell remains silent.

The retina model adds a STP microcircuit at the synapse from bipolar to ganglion cell. Based on the same concept of slow contrast adaptation discussed above, the STP microcircuit reproduces differential motion adaptation by synaptic depression. Therefore, during continued exposure to differential motion, the firing rate of OMS cells exponentially decreases with average time constants in the range 2-20 s[56]. A similar asymmetry is also found in time constants of global and differential motion adaptation. Recovery from differential motion adaptation occurs more slowly, with an average time constant of 52 s.

4.3.2. *Recovery from differential motion adaptation*

A jittering grating has been used to reproduce the experimental setup that simulates fixational eye movements[74; 56; 75]. This grating stimulus divides the image region into an object region covering mainly the ganglion cells receptive field center and a peripheral large background region covering the rest of the retina. Both the background and the object gratings jittered periodically with the same statistics, either coherently (global motion), simulating a stationary background scanned by eye movements, or with different trajectories (differential motion).

Figure 10A shows firing rates of OMS cells in response to this stimulus alternating between 40 s of differential motion and a varying interval of global motion. Our simulation results reproduce the neural tendency of cells registered by Ölveczky *et al.*[56]: slow exponential decay for differential motion and changes in the onset of differential motion after different intervals of global motion. The OMS response at the onset of differential motion presents its maximum value when the time interval of global motion is closer to the average time constant of 52 s and the neuron has enough time to recover its membrane baseline (Figure 10B). Longer intervals of global motion do not significantly increase the OMS response at the onset of differential motion.

5. Conclusions

We have presented a new framework for realistic computational retina modeling that is based on three main contributions: definition of a set of computational retinal microcircuits that can be used as basic building blocks, use thereof to develop retina models that reproduce some of the most characteristic retina functionalities, and implementation of an efficient and configurable retina simulation tool called COREM.

Parameters of the different retina models were optimized to fit published electrophysiological recordings. Our model of photoreceptors and horizontal cells reproduce adaptation to the mean light intensity in response to uniform white pulses at different Weber contrasts, background luminances and as a function of the stimulus drifting frequency. A different retina model accurately predicts temporal contrast adaptation by capturing all adaptive features of temporal filtering and the static nonlinearity in the LN analysis. Finally, we also fitted the neural behavior of OMS ganglion cells for a jittering stimulus that approximates fixational eye movements.

On the other side, we have already published preliminary results[77] of models that implement different retina architectures in the red-green pathway. A retina circuit that reproduces the coextensive receptive field structure in the blue-yellow pathway[78] is currently being developed as well. Both models of the chromatic pathways can be implemented in terms of the computational retinal microcircuits. While our retina models fulfill the goal of this study, future work will require validating these models against new physiological data. Model validation will provide us with a measure of how accurate these models are to predict outcome values for previously unseen data.

Retina models proposed in the literature are often ad hoc models whose parameters can be modified but not their connection scheme. The modular structure of COREM allows for more flexibility of use than other retina simulators[10; 11]. The user can configure different retina architectures through a simulation script that follows a similar syntactic structure of the neural simulator scripts. Following the example of neural simulators, the computational retinal microcircuits implemented in COREM unify different concepts found in the literature and represent some of the most recurrently used algorithms for retina modeling.

With this framework, we have shown by computational simulations that a single processing structure can be plausibly involved in the processing pathway of different retina behaviors. This goes in line with the evidence (see Ref. 37 for a review) that the brain performs a set of canonical neural computations to solve similar problems across different brain regions. A clear example is the feedback mechanism which we have recurrently used to perform gain control (also called divisive normalization) of the neural signal.

While we now have a good understanding of most of the constituent cell types in the retina and some general ideas of their connectivity, computational operations performed by the retina remain as an open research topic. Unified frameworks of different computational theories proposed for the retina modeling are valuable tools that can facilitate future studies in this area.

Acknowledgments

This work has been supported by the Human Brain Project (FET project 604102), Spanish National Grants TIN2013-47069-P and TIN2012-32039, projects P11-TIC-7983 and P11-TIC-8120 of Junta of Andalucia (Spain), co-financed by the European Regional Development Fund (ERDF), and the Spanish Government PhD scholarship FPU13/01487. We used the supercomputer Alhambra of University of Granada for parallel processing of the genetic algorithm optimization.

Appendix A Multiobjective parameter fitting

A multiobjective genetic algorithm automatically optimizes parameters of the retina models for adaptation to the mean light intensity and temporal contrast. A general evolutionary search was configured whereby the random initial population of solutions is evolved by applying uniform crossover and Gaussian mutation operators in combination with a well-known multiobjective selection algorithm (NSGA-II[79]).

Different error functions have been proposed to optimize parameters of neuron models and for model assessment[80–82]. We can distinguish three types of error functions commonly used in neuron model optimization: feature-based, point-by-point comparison of voltage traces and multi-objective functions. To fit the temporal response of our models, we employ a multiobjective function that combines two type of metrics based on point-by-point comparison of voltage traces, the normalized root-mean-square error (NRMSE) and a shape error descriptor.

The first error metric, the (NRMSE) is used to estimate the scale distance between simulated values (y_i) and physiological values (x_i):

$$NRMSE = \frac{\sqrt{\sum_i (y_i - x_i)^2/n}}{y_{max} - y_{min}} \tag{A.1}$$

for vectors of length n. A second error metric, which computes the shape error, is based on local measures of angles between line segments of the simulated curve (v_1) and physiological results (v_2):

$$angle_j(v_1, v_2) = arccosine\left(\frac{v_1 \cdot v_2}{\|v_1\|\|v_2\|}\right)/\pi \tag{A.2}$$

where j is the number of segments. Thus, the first fitness function evaluated by NSGA-II accumulates the NRMSE for the k responses to optimize simultaneously:

$$fitness_1 = \sum_k (NRMSE_k) \tag{A.3}$$

A regularization term is also included, as a second fitness function, to account for shape errors between simulated and physiological results, which are determinant, for instance, in the response oscillations shown in Figure 6:

$$fitness_2 = \sum_k (shape_k) \tag{A.4}$$

where $shape_k$ is an algorithm that computes the sum of the angular errors (according to Eq. A.2) for all segments of the curve k.

Appendix B Model parameters

Best fits of parameters found for the different retina models are shown below.

- *Adaptation to the mean light intensity:* $\tau_{photo} = 20.0\ ms$, $n_{photo} = 2.0$, $a_{photo} = -0.1$, $b_{photo} = 1.0$, $c_{photo} = 0.0$, $C_{calcium} = 1.0\ \mu F/cm^2$, $E_{calcium} = 0.0$, $\tau_{calcium} = 5.0\ ms$, $n_{calcium} = 2.0$, $a_{calcium} = 1.5$, $b_{calcium} = 4.0$, $c_{calcium} = -1.0$, $C_{inner} = 1.0\ \mu F/cm^2$, $E_{inner} = 0.0$, $\tau_{inner} = 10.0\ ms$, $n_{inner} = 3.0$, $a_{inner} = 1000.0$, $b_{inner} = 2.0$, $c_{inner} = -2.0$, $threshold_{inner} = -0.1$, $\tau_{horizontal} = 55.0\ ms$, $n_{horizontal} = 1.0$, $a_{horizontal} = 230.0$, $b_{horizontal} = 20.0$, $c_{horizontal} = 4.0$.
- *Fast and slow temporal contrast adaptation:* $\tau_{photo} = 75.7\ ms$, $n_{photo} = 9.7$, $a_{photo} = -1.0$, $b_{photo} = 1.0$, $c_{photo} = 0.0$, $\tau_{horizontal} = 45.5\ ms$, $n_{horizontal} = 6.4$, $a_{horizontal} = 1.0$, $b_{horizontal} = 1.0$, $c_{horizontal} = 0.83$, $C_{bipolar} = 1.2\ \mu F/cm^2$, $E_{bipolar} = 0.0$, $a_{bipolar} = 66.8$, $b_{bipolar} = 1.0$, $c_{bipolar} = 4.2$, $\tau_{feedback} = 31.0\ ms$, $n_{feedback} = 5.0$, $a_{feedback} = 70.8$, $b_{feedback} = 2.0$, $c_{ganglion} = 6.6$, $a_{ganglion} = 0.5$, $b_{ganglion} = 1.0$, $c_{ganglion} = -95.0$, $k_{(f)ganglion} = 0.5$, $\tau_{(s)ganglion} = 12000\ ms$, $k_{(d)ganglion} = 6.0$.
- *Object motion sensitive (OMS) cells:* $\tau_{photo} = 30.0\ ms$, $n_{photo} = 5.0$, $a_{photo} = -1.0$, $b_{photo} = 1.0$, $c_{photo} = 0.0$, $\tau_{horizontal} = 20.0\ ms$, $n_{horizontal} = 10.0$, $a_{horizontal} = 1.0$, $b_{horizontal} = 1.0$, $c_{horizontal} = 0.0$, $\sigma_{horizontal} = 0.05°$, $C_{bipolar} = 1.0\ \mu F/cm^2$, $E_{bipolar} = 0.0$, $a_{bipolar} = 10.0$, $b_{bipolar} = 1.0$, $c_{bipolar} = 0.0$, $threshold_{bipolar} = 0.0$, $\sigma_{bipolar} = 0.05°$, $\tau_{amacrine} = 5.0\ ms$, $n_{amacrine} = 0.0$, $a_{amacrine} = 30.0$, $b_{amacrine} = 2.0$, $c_{amacrine} = 2.0$, $\sigma_{amacrine} = 0.3°$, $a_{ganglion} = 1.0$, $b_{ganglion} = 2.0$, $c_{ganglion} = 0.0$, $\sigma_{ganglion} = 0.1°$, $k_{(f)ganglion} = 0.1$, $\tau_{(s)ganglion} = 10000\ ms$, $k_{(d)ganglion} = 0.05$.

References

1. S. R. y Cajal, *La rétine des vertébrés* (Typ. de Joseph van In & Cie., 1893).
2. B. B. Lee, P. R. Martin and U. Grünert, Retinal connectivity and primate vision, *Progress in retinal and eye research* **29**(6) (2010) 622–639.
3. T. Gollisch and M. Meister, Eye smarter than scientists believed: neural computations in circuits of the retina, *Neuron* **65**(2) (2010) 150–164.
4. T. Guo, D. Tsai, S. Bai, J. W. Morley, G. J. Suaning, N. H. Lovell and S. Dokos, Understanding the retina: A review of computational models of the retina from the single cell to the network level, *Critical Reviews in Biomedical Engineering* **42**(5) (2014).
5. M. Carandini, J. B. Demb, V. Mante, D. J. Tolhurst, Y. Dan, B. A. Olshausen, J. L. Gallant and N. C. Rust, Do we know what the early visual system does?, *The Journal of Neuroscience* **25**(46) (2005) 10577–10597.
6. M.-O. Gewaltig and M. Diesmann, Nest (neural simulation tool), *Scholarpedia* **2**(4) (2007) p. 1430.
7. M. L. Hines and N. T. Carnevale, The neuron simulation environment, *Neural computation* **9**(6) (1997)

1179–1209.

8. D. F. Goodman and R. Brette, The brian simulator, *Frontiers in neuroscience* **3**(2) (2009) p. 192.
9. J. M. Bower and D. Beeman, *The book of GENESIS: exploring realistic neural models with the GEneral NEural SImulation System* (Springer Science & Business Media, 2012).
10. A. Benoit, A. Caplier, B. Durette and J. Hérault, Using human visual system modeling for bio-inspired low level image processing, *Computer Vision and Image Understanding* **114**(7) (2010) 758–773.
11. A. Wohrer and P. Kornprobst, Virtual retina: a biological retina model and simulator, with contrast gain control, *Journal of computational neuroscience* **26**(2) (2009) 219–249.
12. J. Hérault and B. Durette, Modeling visual perception for image processing, *Computational and Ambient Intelligence*, (Springer, 2007), pp. 662–675.
13. C. A. Morillas, S. F. Romero, A. Martínez, F. J. Pelayo, E. Ros and E. Fernández, A design framework to model retinas, *Biosystems* **87**(2) (2007) 156–163.
14. K. Zaghloul, K. Boahen *et al.*, Optic nerve signals in a neuromorphic chip i: Outer and inner retina models, *Biomedical Engineering, IEEE Transactions on* **51**(4) (2004) 657–666.
15. J. v. van Hateren, L. Rüttiger, H. Sun and B. Lee, Processing of natural temporal stimuli by macaque retinal ganglion cells, *The Journal of neuroscience* **22**(22) (2002) 9945–9960.
16. J. Hérault, A model of colour processing in the retina of vertebrates: From photoreceptors to colour opposition and colour constancy phenomena, *Neurocomputing* **12**(2) (1996) 113–129.
17. R. L. De Valois and K. K. De Valois, A multi-stage color model, *Vision research* **33**(8) (1993) 1053–1065.
18. Z. Li, Different retinal ganglion cells have different functional goals, *International Journal of Neural Systems* **3**(03) (1992) 237–248.
19. Y. Ozuysal and S. A. Baccus, Linking the computational structure of variance adaptation to biophysical mechanisms, *Neuron* **73**(5) (2012) 1002–1015.
20. H. van Hateren, A cellular and molecular model of response kinetics and adaptation in primate cones and horizontal cells, *Journal of vision* **5**(4) (2005) p. 5.
21. C. Enroth-Cugell and J. G. Robson, The contrast sensitivity of retinal ganglion cells of the cat, *The Journal of physiology* **187**(3) (1966) 517–552.
22. B. B. Lee, R. M. Shapley, M. J. Hawken and H. Sun, Spatial distributions of cone inputs to cells of the parvocellular pathway investigated with cone-isolating gratings, *JOSA A* **29**(2) (2012) A223–A232.
23. O. S. Packer and D. M. Dacey, Receptive field structure of h1 horizontal cells in macaque monkey retina, *Journal of Vision* **2**(4) (2002) p. 1.
24. R. A. Young, The gaussian derivative model for spatial vision: I. retinal mechanisms, *Spatial vision* **2**(4) (1987) 273–293.
25. S. Tan, J. L. Dale and A. Johnston, Performance of three recursive algorithms for fast space-variant gaussian filtering, *Real-Time Imaging* **9**(3) (2003) 215–228.
26. B. Triggs and M. Sdika, Boundary conditions for young-van vliet recursive filtering, *Signal Processing, IEEE Transactions on* **54**(6) (2006) 2365–2367.
27. R. Deriche, Fast algorithms for low-level vision, *Pattern Analysis and Machine Intelligence, IEEE Transactions on* **12**(1) (1990) 78–87.
28. R. Deriche, Recursively implementating the gaussian and its derivatives, *Research Report (Inria-00074778)* (1993).
29. M. J. Berry, I. H. Brivanlou, T. A. Jordan and M. Meister, Anticipation of moving stimuli by the retina, *Nature* **398**(6725) (1999) 334–338.
30. V. C. Smith, J. Pokorny, B. B. Lee and D. M. Dacey, Primate horizontal cell dynamics: an analysis of sensitivity regulation in the outer retina, *Journal of Neurophysiology* **85**(2) (2001) 545–558.
31. D. B. Kastner and S. A. Baccus, Coordinated dynamic encoding in the retina using opposing forms of plasticity, *Nature neuroscience* **14**(10) (2011) 1317–1322.
32. A. L. Hodgkin and A. F. Huxley, A quantitative description of membrane current and its application to conduction and excitation in nerve, *The Journal of physiology* **117**(4) (1952) 500–544.
33. A. V. Herz, T. Gollisch, C. K. Machens and D. Jaeger, Modeling single-neuron dynamics and computations: a balance of detail and abstraction, *science* **314**(5796) (2006) 80–85.
34. P. Dayan and L. Abbott, Theoretical neuroscience: computational and mathematical modeling of neural systems, *Journal of Cognitive Neuroscience* **15**(1) (2003) 154–155.
35. B. Hille *et al.*, *Ion channels of excitable membranes* (Sinauer Sunderland, MA, 2001).
36. D. Sterratt, B. Graham, A. Gillies and D. Willshaw, *Principles of computational modelling in neuroscience* (Cambridge University Press, 2011).
37. M. Carandini and D. J. Heeger, Normalization as a canonical neural computation, *Nature Reviews Neuroscience* **13**(1) (2012) 51–62.
38. J. D. Victor, The dynamics of the cat retinal x cell centre., *The Journal of Physiology* **386**(1) (1987) 219–246.
39. V. Mante, V. Bonin and M. Carandini, Functional mechanisms shaping lateral geniculate responses to artificial and natural stimuli, *Neuron* **58**(4) (2008) 625–638.
40. M. Carandini, D. J. Heeger and J. A. Movshon, Linearity and normalization in simple cells of the macaque primary visual cortex, *The Journal of Neuroscience* **17**(21) (1997) 8621–8644.
41. K. Purpura, D. Tranchina, E. Kaplan and R. M.

Shapley, Light adaptation in the primate retina: analysis of changes in gain and dynamics of monkey retinal ganglion cells, *Visual neuroscience* **4**(01) (1990) 75–93.

42. V. Torre and T. Poggio, A synaptic mechanism possibly underlying directional selectivity to motion, *Proceedings of the Royal Society of London. Series B. Biological Sciences* **202**(1148) (1978) 409–416.
43. F. R. Amthor and N. M. Grzywacz, Nonlinearity of the inhibition underlying retinal directional selectivity, *Visual neuroscience* **6**(03) (1991) 197–206.
44. R. R. Harrison and C. KocH, An analog vlsi inplementation of a visual interneuron: Enhanced sensory processing through biophysical modeling, *International Journal of Neural Systems* **9**(05) (1999) 391–395.
45. R. A. Silver, Neuronal arithmetic, *Nature Reviews Neuroscience* **11**(7) (2010) 474–489.
46. S. A. Baccus and M. Meister, Fast and slow contrast adaptation in retinal circuitry, *Neuron* **36**(5) (2002) 909–919.
47. F. Rieke, Temporal contrast adaptation in salamander bipolar cells, *The Journal of Neuroscience* **21**(23) (2001) 9445–9454.
48. K. J. Kim and F. Rieke, Temporal contrast adaptation in the input and output signals of salamander retinal ganglion cells, *The Journal of Neuroscience* **21**(1) (2001) 287–299.
49. D. Chander and E. Chichilnisky, Adaptation to temporal contrast in primate and salamander retina, *The Journal of Neuroscience* **21**(24) (2001) 9904–9916.
50. K. A. Zaghloul, K. Boahen and J. B. Demb, Different circuits for on and off retinal ganglion cells cause different contrast sensitivities, *The Journal of Neuroscience* **23**(7) (2003) 2645–2654.
51. R. S. Zucker and W. G. Regehr, Short-term synaptic plasticity, *Annual review of physiology* **64**(1) (2002) 355–405.
52. M. Tsodyks and S. Wu, Short-term synaptic plasticity, *Scholarpedia* **8**(10) (2013) p. 3153.
53. B. Suh and S. A. Baccus, Building blocks of temporal filters in retinal synapses, *PLoS Biol* **12**(10) (2014) p. e1001973.
54. D. L. Beaudoin, M. B. Manookin and J. B. Demb, Distinct expressions of contrast gain control in parallel synaptic pathways converging on a retinal ganglion cell, *The Journal of physiology* **586**(22) (2008) 5487–5502.
55. M. B. Manookin and J. B. Demb, Presynaptic mechanism for slow contrast adaptation in mammalian retinal ganglion cells, *Neuron* **50**(3) (2006) 453–464.
56. B. P. Ölveczky, S. A. Baccus and M. Meister, Retinal adaptation to object motion, *Neuron* **56**(4) (2007) 689–700.
57. J. B. Demb, Functional circuitry of visual adaptation in the retina, *The Journal of physiology* **586**(18) (2008) 4377–4384.
58. F. S. Chance, S. B. Nelson and L. F. Abbott, Synaptic depression and the temporal response characteristics of v1 cells, *The Journal of neuroscience* **18**(12) (1998) 4785–4799.
59. M. Carandini, D. J. Heeger and W. Senn, A synaptic explanation of suppression in visual cortex, *The Journal of Neuroscience* **22**(22) (2002) 10053–10065.
60. D. Tschumperlé, The cimg library, *IPOL 2012 Meeting on Image Processing Libraries*, 2012, pp. 4–pp.
61. O. Estévez, On the fundamental data-base of normal and dichromatic colour vision, PhD thesis, University of Amsterdam (1979).
62. S. Ghosh-Dastidar and H. Adeli, Spiking neural networks, *International Journal of Neural Systems* **19**(04) (2009) 295–308.
63. B. B. Lee, D. M. Dacey, V. C. Smith and J. Pokorny, Dynamics of sensitivity regulation in primate outer retina: The horizontal cell network, *Journal of Vision* **3**(7) (2003) p. 5.
64. F. A. Dunn, M. J. Lankheet and F. Rieke, Light adaptation in cone vision involves switching between receptor and post-receptor sites, *Nature* **449**(7162) (2007) 603–606.
65. D. Tranchina, J. Gordon and R. Shapley, Retinal light adaptation-evidence for a feedback mechanism, *Nature* **310**(5975) (1984) 314–316.
66. V. C. Smith, J. Pokorny, B. B. Lee and D. M. Dacey, Sequential processing in vision: The interaction of sensitivity regulation and temporal dynamics, *Vision research* **48**(26) (2008) 2649–2656.
67. D. A. Clark, R. Benichou, M. Meister and R. A. da Silveira, Dynamical adaptation in photoreceptors (2013).
68. J. B. Demb, Multiple mechanisms for contrast adaptation in the retina, *Neuron* **36**(5) (2002) 781–783.
69. D. L. Beaudoin, B. G. Borghuis and J. B. Demb, Cellular basis for contrast gain control over the receptive field center of mammalian retinal ganglion cells, *The Journal of neuroscience* **27**(10) (2007) 2636–2645.
70. K. J. Kim and F. Rieke, Slow na+ inactivation and variance adaptation in salamander retinal ganglion cells, *The Journal of neuroscience* **23**(4) (2003) 1506–1516.
71. P. Martínez-Cañada, C. Morillas, S. Romero and F. Pelayo, Modeling retina adaptation with multiobjective parameter fitting, *Advances in Computational Intelligence*, (Springer, 2015), pp. 175–184.
72. P. Martínez-Cañada, C. Morillas, B. Pino and F. Pelayo, Towards a generic simulation tool of retina models, *Artificial Computation in Biology and Medicine*, (Springer, 2015), pp. 47–57.
73. K. A. Zaghloul, K. Boahen and J. B. Demb, Contrast adaptation in subthreshold and spiking responses of mammalian y-type retinal ganglion cells, *The Journal of neuroscience* **25**(4) (2005) 860–868.
74. B. P. Ölveczky, S. A. Baccus and M. Meister, Segregation of object and background motion in the retina, *Nature* **423**(6938) (2003) 401–408.
75. S. A. Baccus, B. P. Ölveczky, M. Manu and M. Meis-

ter, A retinal circuit that computes object motion, *The Journal of Neuroscience* **28**(27) (2008) 6807–6817.

76. J. B. Demb, K. Zaghloul, L. Haarsma and P. Sterling, Bipolar cells contribute to nonlinear spatial summation in the brisk-transient (y) ganglion cell in mammalian retina, *The Journal of neuroscience* **21**(19) (2001) 7447–7454.
77. P. Martínez-Cañada, C. Morillas, J. L. Nieves, B. Pino and F. Pelayo, First stage of a human visual system simulator: The retina, *Computational Color Imaging*, (Springer, 2015), pp. 118–127.
78. J. D. Crook, C. M. Davenport, B. B. Peterson, O. S. Packer, P. B. Detwiler and D. M. Dacey, Parallel on and off cone bipolar inputs establish spatially coextensive receptive field structure of blue-yellow ganglion cells in primate retina, *The Journal of Neuroscience* **29**(26) (2009) 8372–8387.
79. N. Srinivas and K. Deb, Muiltiobjective optimization using nondominated sorting in genetic algorithms, *Evolutionary computation* **2**(3) (1994) 221–248.
80. W. Van Geit, E. De Schutter and P. Achard, Automated neuron model optimization techniques: a review, *Biological cybernetics* **99**(4-5) (2008) 241–251.
81. J. C. da Silva Martins, Computational models, neuronal metrics and system identification in bioelectronic vision, PhD thesis (2012).
82. S. Druckmann, Y. Banitt, A. Gidon, F. Schürmann, H. Markram and I. Segev, A novel multiple objective optimization framework for constraining conductance-based neuron models by experimental data, *Frontiers in neuroscience* **1**(1) (2007) p. 7.

Appendix B

This is a preprint. Link to the DOI of the published manuscript: https://doi.org/10.1016/j.neucom.2016.08.120

Genetic algorithm for optimization of models of the early stages in the visual system

Pablo Martínez-Cañada[a,*], Christian Morillas[a], Samuel Romero[a], Hans E. Plesser[b], Francisco Pelayo[a]

[a] *CITIC, Department of Computer Architecture and Technology, University of Granada, Spain*
[b] *Department of Mathematical Sciences and Technology, Norwegian University of Life Sciences, Norway*

Abstract

Automated parameter search methods are commonly used to optimize neuron models. A more challenging task is to fit models of neural systems since the model response is determined by both intrinsic properties of neurons and the neural wiring and architecture of the network. Neural records of cells in the visual system are often analyzed in terms of the cell's receptive field and its temporal response. This type of data requires a finer point-by-point comparison of response traces between the simulated output and the recorded data. To address these issues, we applied a genetic algorithm optimization in conjunction with a multiobjective fitness function and a population-based error metric. Two different models of the early stages in the visual system were fitted to electrophysiological recordings and results from a modeling study, respectively. The first one is a model of cone photoreceptors and horizontal cells that reproduces adaptation to the mean light intensity in the retina. A multiobjective fitness function based on the normalized root-mean-square error (NRMSE) and a shape error descriptor captures high-frequency oscillations in the impulse response to uniform white flashes. The second one is a large-scale model of the thalamocortical system that accounts for the slow rhythms observed during sleep. An

---

[*] Corresponding author

Email addresses: `pablomc@ugr.es` (Pablo Martínez-Cañada), `cmg@ugr.es` (Christian Morillas), `sromero@ugr.es` (Samuel Romero), `hans.ekkehard.plesser@nmbu.no` (Hans E. Plesser), `fpelayo@ugr.es` (Francisco Pelayo)

error metric of the population neural activity is used in this case. We argue that the optimization framework proposed in this paper could serve as an useful tool for parameter fitting of neuron models and large-scale models in the visual pathway.

Keywords: Genetic algorithm, multiobjective parameter fitting, neural system optimization, retina model, thalamocortical system

1. Introduction

Neuron models often have many parameters that are difficult to estimate manually. Parameter optimization is facilitated by automated search methods that minimize an error metric representing differences between simulated and experimental data[1, 2, 3, 4, 5, 6]. Traditionally, models of the early visual pathways, referred to the retina, Lateral Geniculate Nucleus (LGN) and primary visual cortex (V1), are hand-tuned, using a trial-and-error method. No automated optimization method is present and, if any, it is not described in their respective publications[7, 8, 9, 10, 11, 12]. Although some of the model parameters are constrained experimentally, yet some of them cannot be measured by simple electrophysiological methods, specially when the model is complex and its response described by a large number of parameters. However, there are some important exceptions here. In the retina model proposed by Ozuysal and Baccus[13], multiple initial points are used by a nonlinear programming solver to converge to different local optima and then choose the best solution. Besides, a function that computes the error of the estimated membrane potential across the time and frequency domains, allows capturing both slow shifts in potential and high-frequency fluctuations. Mante et al.[14] optimized independently each stage of their LGN model in a multi-step fitting process based on the mean-squared error (MSE). In the photoreceptor model by van Hateren[15], the parameter fitting is based on linear programming for minimizing the root-mean-square deviation (RMSD) between model responses and measurements. In simultaneous-response fitting, the RMSD of the highest responses are multiplied by a scaling factor to prevent biased results.

A genetic algorithm (GA)[16] is a popular, biologically inspired optimization method that can prevent the search from converging on local minima. In addition, GAs do not need a mathematical model, or an estimate, of the objective function, like in gradient methods. Therefore, GAs are more likely to find the global optimum, and require relatively little knowledge of the problem being solved. Although computation of the fitness function can be time-consuming, the inherently parallel nature of GAs simplifies the implementation of a multiprocessing architecture. In this paper, a GA optimization is shown to be an effective solution that facilitates parameter search of neural models with a minimal configuration setup.

The second critical component of the optimization algorithm is the error metric. We can distinguish three types of error metrics commonly used in neuron model optimization: feature-based, point-by-point comparison of response traces and multi-objective functions[1]. In experiments that study the visual processing pathway, neurons are often stimulated by synthetic input patterns (e.g., sinusoidal drifting gratings) and their neural outputs characterized by changes produced in their receptive fields and temporal responses[17, 18, 19, 20]. Fitting every feature of this type of responses is crucial to understand the mechanisms involved in the visual function and, as discussed in Section 2.2, a standard point-by-point comparison of traces (e.g., by using only the MSE) is insufficient to characterize high-frequency components of the neural signal. Here, we describe a multiobjective fitness function that combines two types of error metrics, the normalized root-mean-square error (NRMSE) and a shape error descriptor. Our approach captures high-frequency oscillations of the temporal response and overcomes also the problem of rescaling the data to prevent biased results.

Parameters of the large-scale model of the thalamocortical system were fitted by a feature-based error metric that compares the average membrane potential of the population in specific time intervals. We used the target membrane potentials estimated from results of the modeling study of this system. The GA optimization allowed us to bring the model of the thalamocortical system into a stable parameter regime where it reproduces qualitatively the neural behavior of the original model.

2. Methods

2.1. Genetic algorithm optimization

Genetic algorithms have shown to be an effective method for constraining conductance-based compartmental models[2, 3, 21]. In brief, a genetic algorithm is a search heuristic wherein a population of candidate solutions (called individuals) is iteratively evolved toward better solutions. In each iteration (generation), a fitness function assesses deviations of the results generated by individuals in the population from the target data. The most fit individuals are selected from the current population and their values modified, according to the well-known genetic operators of crossover and mutation, to form a new generation. The algorithm is iterated until a maximum number of generations has been produced, or a satisfactory fitness level has been reached for the population.

In our implementation, an individual is an array of real numbers that represent parameters of the simulation model to be optimized. These parameters are constrained to be within a biological range (e.g., time constants are between 1 and 100 ms). We use two different selection operators, tournament selection for single-objective optimization, which has several benefits over alternative selection methods[22], and one of the most commonly used Pareto optimization algorithm, NSGA-II[23]. The genetic operator selected for crossover is uniform crossover. Different operators were tested (such as one-point and two-point crossover algorithms) but we found no difference in results, only in the convergence speed of the genetic algorithm. Similarly, in the chosen Gaussian mutation operator, different values of μ and σ were evaluated, observing some slight differences in the convergence rate. The genetic algorithm is implemented by using the Python library DEAP[24].

Evaluation of the fitness function for each individual represents the bottleneck in the processing of the genetic algorithm. In order to overcome this drawback, we implemented a parallel processing architecture in a computer cluster based on the MPI interface[25] that distributes evaluation of individuals across different processes. In particular, we use the MPI specification included in the Python library *mpi4py*[26]. A master-slave configuration selects a root process that evenly splits the population every generation and scatters data to the rest of processes. Once all individuals assigned to each process are evaluated, the root node gathers individual fitnesses from all processes and resumes the evolutionary algorithm.

2.2. Error metrics and fitness functions

2.2.1. Multiobjective optimization

When comparing point-by-point voltage traces of the simulated model response and target data, a mere MSE-based metric may provide misleading results (as illustrated in the example of Fig. 1). In this figure, the temporal response of a fictional neuron is generated (labeled as *data*) and compared with the temporal responses of two different models (*model 1* and *model 2*), handmade as well. A MSE-based metric (NRMSE) and an shape error descriptor, detailed below, are computed between data and model responses, shown in Table 1. Although the voltage trace of *model 1* reproduces better the target oscillatory behavior, its NRMSE is higher when compared with *model 2* because of an offset difference. It is therefore necessary to add a second metric that considers also the shape of responses, where the information of high-frequency components lies. In other fields, as in hyperspectral imaging, the joint effect of these two types of metrics has been also employed to accurately compare spectral data in terms of shape and offset[27, 28].

We define the NRMSE as:

$$NRMSE = \frac{\sqrt{\sum_i (data_i - model_i)^2/n}}{data_{max} - data_{min}} \tag{1}$$

The error is computed between n samples of target data ($data_i$) and model response ($model_i$), and normalized within the data range ($data_{max} - data_{min}$).

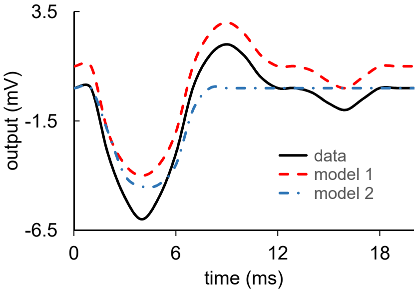

Figure 1: Example that illustrates the different values provided by the two error metrics implemented in the multiobjective optimization, NRMSE and shape error, computed between the handmade responses of two arbitrary models (*model 1* and *model 2*) and recorded *data*.

Table 1: NRMSEs and shape errors obtained for models in Fig. 1.

	model 1	**model 2**
NRMSE	0.1404	0.1104
Shape error	0.0114	0.1487

Error normalization to the data range prevents biased results in simultaneous-response fitting for different input stimuli.

We also introduce a shape error metric that is calculated by averaging angular differences between line segments that connect target and model samples:

$$shape_{error} = \min_{s} \left(\frac{\sum_i \left(arccosine \left(\frac{\vec{a_i} \cdot \vec{b_{i,s}}}{\|\vec{a_i}\| \|\vec{b_{i,s}}\|} \right) / \pi \right)}{n-1} \right) \qquad (2)$$

every line segment i connecting data samples is defined as a vector $\vec{a_i}$ wherein coordinates along the x-axis refer to the time (or spatial) axis, and along the y-axis to the target response: $\vec{a_i} = (t_{i+1} - t_i, data_{i+1} - data_i)$. Similarly, the y-axis of the vector $\vec{b_{i,s}}$ is referred to the model response: $\vec{b_{i,s}} = (t_{i+1+s} - t_{i+s}, model_{i+1+s} - model_{i+s})$. Since an exact shape matching of model and data responses may be considerably difficult to achieve, a more flexible approach is selected so that we allow a small shift of the traces in the x-axis by s positions when computing the error. The minimum error for all shifts is selected as the final shape error. A shift of ±1 was fixed for our simulations. We apply this metric to monotonically increasing functions, e.g., temporal series and spatial responses, so that the *arccosine* is always positive within the range $[0, \pi]$ and, thus, the shape error is normalized as well.

These two metrics are integrated in the multiobjective optimization algorithm as follows: given that there are M responses to optimize simultaneously, corresponding to k different input stimuli, the two fitness functions are simply formulated as average sums of the NRMSE and shape errors, respectively, for all responses:

$$fitness_{multobj1} = \sum_{k} (NRMSE_k)/M \tag{3}$$

$$fitness_{multobj2} = \sum_{k} (Shape_k)/M \tag{4}$$

2.2.2. Single-objective optimization

On the other hand, parameters of the large-scale model of the thalamocortical system were fitted by a feature-based error metric that compares the average neural responses of the population in specific time intervals. Our goal for this model was to bring it into a stable parameter regime where it reproduces qualitatively the simulation results of the original publication. We found that a single-objective optimization is sufficient to fit the target membrane potentials estimated from the original study.

The following fitness function computes the RMSE between the average membrane potential of the simulated population in a time interval t, $V_{sim}(t)$, and the target average membrane potential, $V_{tar}(t)$:

$$fitness_{singobj} = \frac{\sum_{l} \sqrt{\sum_{t} (V_{tar}(t) - V_{sim}(t))^2 / T}}{L} \tag{5}$$

where T is the total number of time intervals. For a multi-layered model, responses of L neural layers (from $l = 1$ to L) are optimized simultaneously by averaging as well this error across them. We achieved a reasonably good fit of our model by simply using the average membrane potential of the population. Nevertheless, different feature-based error metrics (e.g., after-hyperpolarizing potential or firing rate[1, 2]) can be easily embedded in our single-objective optimization scheme to consider other properties that may be more discriminative depending on the target data.

2.3. Models of the early stages in the visual system

The above-described optimization framework was applied to models of the retina cones and horizontal cells and the thalamocortical system (shown in Fig. 2). The first model was implemented using COREM[29, 30, 31], a software platform that provides a set of computational retinal microcircuits that can be used as basic building blocks for the modeling of different retina mechanisms. We simplified and adapted the molecular model of cones and horizontal cells proposed by van Hateren[15] to fit electrophysiological data obtained from horizontal cells of the macaque retina[19]. There are 22 parameters distributed across the three principal stages of the model: outer segment (phototransduction and calcium feedback), inner segment and horizontal cell's feedback mechanism. Photoreceptors' neural response to uniform white flashes of different time length was recorded at a fixed Weber contrast of 8 and varying background illuminance. The model fittings were made to nine stimulus conditions simultaneously (resulting from all possible combinations of three different time lengths and three background light intensities), which means a value of $M = 9$ in Eqs. 3 and 4. We applied the multiobjective optimization approach to fit a target set of temporal impulse responses. Further details on the model are provided in reference [29].

The second model is an implementation of the thalamocortical system developed by Hill and Tononi[32] using NEST 2.8.0[33]. This is a large-scale model that encompasses portions of two cortical visual areas and associated thalamic and reticular thalamic nuclei, with thousands of model neurons that incorporate

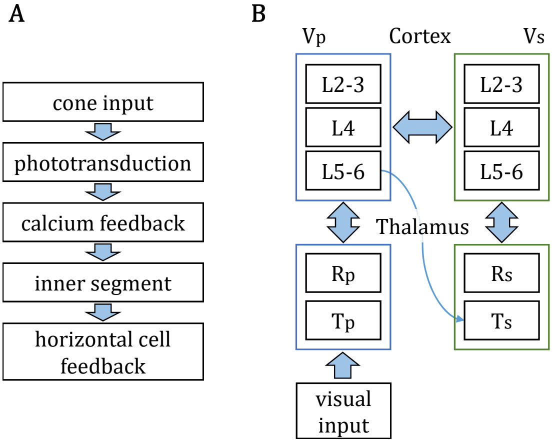

Figure 2: Schematic of the two models. A: Model of the retina cones and horizontal cells. B: Thalamocortical system. The primary visual area includes a 3-layered cortical area (Vp), reticular nucleus (Rp) and dorsal thalamus (Tp). The secondary visual area is formed by its associated cortical area (Vs), reticular nucleus (Rs) and dorsal thalamus (Ts). Implemented according to the system developed by Hill and Tononi[32].

both intrinsic and synaptic currents. It accounts for transition from wakefulness to sleep and the generation of the slow oscillation. We decided to maintain the same network configuration (e.g., synaptic masks, kernels and weights) as in the original model so that only peak conductances of intrinsic ion channels are optimized, allowing to countervail slight deviations in the model output as a result of using different simulators. We studied how the increase in the potassium leak conductance and the four intrinsic conductances can drive the transition from the waking mode to the sleep mode. This transition is simulated in two time-discrete steps: initial peak conductances are first set to half of their values for the waking mode, temporal simulation advances for 400 ms and then these peak values are set to the final values maintained during the waking mode. Therefore, there is a total of 10 parameters to optimize: initial and end peak conductance values. For this purpose, we applied the single-objective optimization to fit the average membrane potential of the different neural layers.

The model neuron of the thalamocortical system is a single-compartment spiking neuron incorporating Hodgkin-Huxley currents:

$$I_{channel} = g_{peak} m^N h (V - E_{channel}) \qquad (6)$$

where g_{peak} is the maximal conductance of the channel, m and h determine its activation and inactivation respectively, V is the membrane potential and $E_{channel}$ is the reversal potential for the given channel. The factor N allows the activation to occur on a different order than inactivation. Optimization is conducted on the following intrinsic channels: persistent sodium current ($I_{Na(p)}$), pacemaker current (I_h), low-threshold calcium current (I_T) and depolarization-activated potassium current (I_{DK}), in addition to the potassium leak conductance (see reference [32] for further details on these conductances).

3. Results

3.1. Model of the retina cones and horizontal cells

We experimented with different combinations of the following GA parameters: number of generations, population size, crossover and mutation rates. In Fig. 3, we plot optimization results when the GA is configured with 200 generations, 800 individuals in the population and crossover and mutation rates of 0.5 and 0.3, respectively. Under other conditions, the GA does not converge or its convergence rate is lower. Evolution of the hypervolume shows that approximately after 50 generations the GA converges to an optimal solution. However, a slightly better tune of model parameters is found when the hypervolume rises again after 160 generations, decreasing to a greater extent the shape error.

Two extreme solutions of the Pareto front are also shown as an example of results reached by emphasizing one or the other error metric. High-frequency oscillations are better captured by the solution depicted at the bottom of the figure, where the shape error is minimum, particularly within the first 100 ms of the 100 td response. However, this solution presents also significant offset

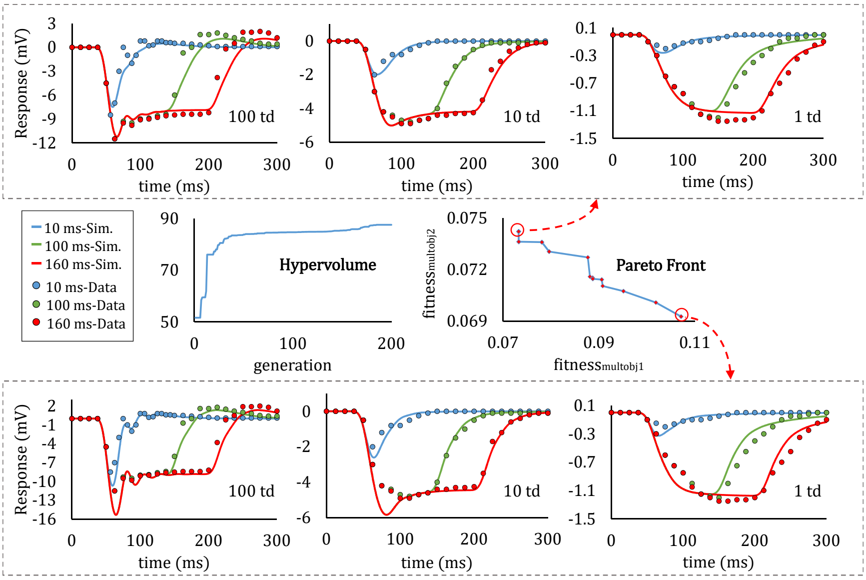

Figure 3: Results of the multiobjective optimization applied to the model of the retina cones and horizontal cells. Evolution of the hypervolume over generations and the estimated Pareto front are shown in the center of the figure. Two extreme solutions of the Pareto front are depicted at the top (minimum NRMSE) and bottom (minimum shape error). They represent simulation results of the model (color solid lines) and electrophysiological recordings (color markers) obtained from horizontal cells of the macaque retina[19]. Data points have been sampled from Figure 6 in the publication[19]. Input stimuli are spatially uniform white flashes of 10, 100, and 160 ms at a fixed Weber contrast of 8 and background illuminances of 1, 10 and 100 trolands (td). All flashes start at 0 ms.

errors in some specific points (observe the minimum value of the 100 and 10 td responses). On the other hand, the solution at the top of the figure limits this high-frequency behavior but the squared-error is minimized for all samples. Intermediate solutions provide a trade-off between these two error functions.

3.2. Thalamocortical system

In this model, the transition from the waking mode to the sleep mode (see Fig. 4) comes about by increasing the potassium leak conductance and the four intrinsic conductances. The single-objective fitness function (Eq. 5) averages the error across the 5 populations shown in Fig. 4 A and the following 5 time intervals: wakefulness (from 0 to 200 ms), transition to the sleep mode (from 200 to 600 ms), first oscillation of the sleep mode (from 600 to 1100 ms), down-state (from 1100 ms to 1600 ms) and second oscillation (from 1600 to 2100 ms). During the first time interval, peak conductances are set to a initial value (g_I) and afterwards, in the second time interval, they are modified to half of their maximum values in the sleep mode. From the third time interval on, conductances take their maximum value (g_E). Although conductances were fitted only to the first 2100 ms, the model remains stable afterward for an extended period of time showing that the fit is reasonably robust.

We used the target average membrane potentials shown in Table 2. Average membrane potentials of the up- and down-states of the cortical layers are -58 and -75 mV respectively, according to values provided in reference [32]. Other values are interpolated by visual inspection of results published by Hill and Tononi[32].

The GA is configured with 100 generations, 512 individuals in the population and crossover and mutation rates of 0.5 and 0.3, respectively. Optimal peak conductances are: potassium leak conductance g_{KL}, between 1.0 (initial value) and 2.2 (end value); persistent sodium current $I_{Na(p)}$, 1.0 and 5.0; pacemaker current I_h, 0.01 and 4.61; low-threshold calcium current I_T, 0.97 and 2.07; and depolarization-activated potassium current I_{DK}, 0.17 and 2.27.

With the increase in the potassium leak conductance (its peak value goes from 1.0 to 2.2) the network enters the hyperpolarized state of around -75 mV. The 3 primary active intrinsic currents underlying the up- and down-states in cortical neurons are I_h, $I_{Na(p)}$ and I_{DK}, as shown in Fig. 5. These 3 currents experience a significant increase during the sleep mode compared to the waking mode. I_h is hyperpolarization-activated, shifting the membrane potential

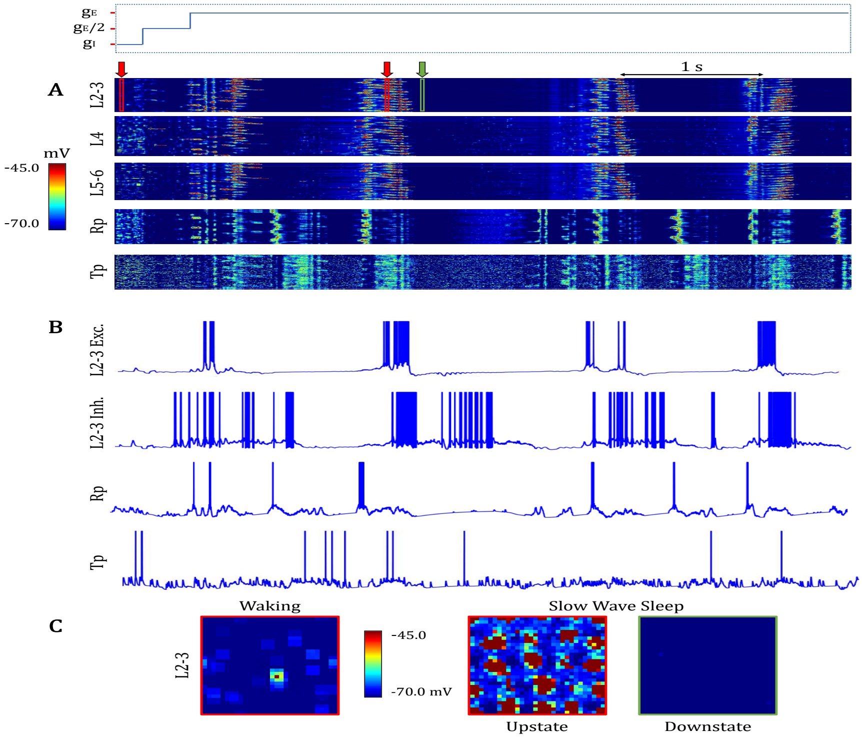

Figure 4: Simulation of the transition from the waking mode to the sleep mode in the thalamocortical visual system (see Fig. 4 in the reference publication[32]) with the optimal set of parameters found by the single-objective optimization. g_I and g_E are the initial and end values of intrinsic conductances. A: membrane potential rasters of 100 neighboring cells in the primary visual area over 5.1 s (cortical layers L2-3, L4 and L5-6, and reticular nucleus cells (Rp) and thalamocortical neurons (Tp)). B: membrane potential traces from excitatory and inhibitory cells in cortical layer L2-3, Rp and Tp. C: topographical activity plots show the average membrane potential during wakefulness (green), and the upstate and downstate of the slow oscillations in the sleep mode (green and red). Red and green boxes (in A) during the waking mode and the sleep mode indicate the time window (10 ms) of the averaged activity.

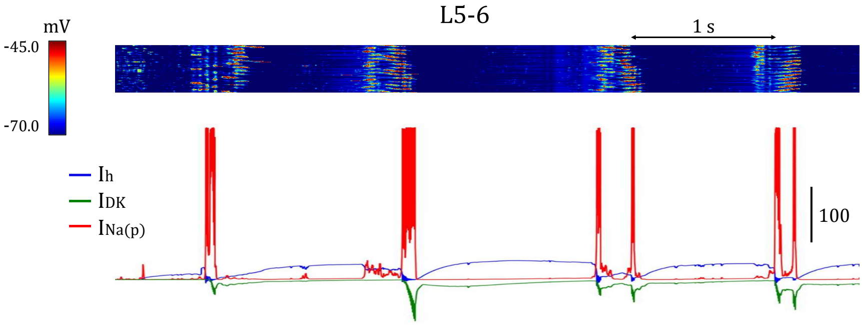

Figure 5: Membrane potential raster of cortical layer L5-6 compared with the individual intrinsic current traces for a selected cell in this layer. Conductance units are dimensionless since the neuron model does not have a defined area or volume.

Table 2: Target average membrane potentials (mV) used in the optimization.

	L2-3	**L4**	**L5-6**	**Rp**	**Tp**
0-200 ms	-65	-65	-65	-68	-68
200-600 ms	-75	-75	-75	-70	-70
600-1100 ms	-58	-58	-58	-65	-68
1100-1600 ms	-75	-75	-75	-75	-75
1600-2100 ms	-58	-58	-58	-65	-68

towards a more depolarized level during the down-state. When the membrane potential exceeds certain threshold, $I_{Na(p)}$ activates, promoting a spike burst. This burst initiates the depolarized phase of the slow oscillation until I_{DK}, also activated during spiking, progressively forces the cell to enter again the hyperpolarized state. The interplay among $I_{Na(p)}$, I_{DK} and I_h during sleep is determinant for shaping oscillations of the slow wave. I_T, only present in thalamus cells, does not increase significantly during the sleep mode (results not shown here), what discards a key role of this current.

4. Conclusion

Numerous approaches have been proposed to automatically search for sets of parameters of neuron models that best fit available experimental data[1, 2, 34]. The response of a neural system, however, is described by both intrinsic parameters that define the cells' morphology and biophysical dynamics and parameters of the network architecture and connections. We employed a genetic algorithm optimization, implemented with the Python library DEAP[24], to fit parameters of two different models of the visual system. The first one is a model of cone photoreceptors and horizontal cells that reproduces adaptation to the mean light intensity in the retina. It was configured using the simulation platform COREM[29]. The second model is an implementation of the large-scale thalamocortical system developed by Hill and Tononi[32] using NEST 2.8.0[33].

In the electrophysiology of the visual system, fitting every feature of the neuron's receptive field or the temporal response to specific stimulus conditions, is crucial to understand the mechanisms involved in the visual function. We have shown that a standard point-by-point comparison of response traces (e.g., by using only the MSE) is insufficient to accurately compare data and model responses. A multiobjective error metric has been proposed based on combination of the normalized root-mean-square error (NRMSE) and a shape error descriptor. We used this metric in conjunction with the well-known algorithm NSGA-II[23] to search for parameters of the model of cone photoreceptors and horizontal cells. Secondly, parameters of the model of the thalamocortical system are fitted by a single-objective feature-based error function. This function computes differences between data and model responses in terms of the average membrane potential of a set of neuron populations in specific time intervals.

Two extreme solutions of the multiobjective optimization have been used in Fig. 3 as an example of the type of results reached by giving more weighting to the NRMSE or to the shape error. High-frequency oscillations are better captured by the minimum shape-error solution of the Pareto front, particularly within the first 100 ms of the 100 td response. However, this solution presents also significant deviations from the target data in some specific points. On the contrary, the other solution has a smaller NRMSE but does not reproduce all high-frequency features of the data. We argue that results of the fitting can modify the model specifications and make us reconsider the mechanisms that shape the visual response. For example, the minimum shape-error solution justifies the inclusion of a second feedback component in the model of the cone photoreceptors and horizontal cells (see reference [29] for further discussion).

In the thalamocortical system model, the transition from the waking mode to the sleep mode is initiated by the increase of the potassium leak conductance, which triggers the hyperpolarized state of the network. During the sleep mode, the most significant changes in the intrinsic conductance values have been calculated for I_h, $I_{Na(p)}$ and I_{DK}. The interaction among these 3 currents provides a description of the up- and down-states of the slow oscillation in agreement with the study by Hill and Tononi[32]. We reproduced their simulation results by changing peak conductances of intrinsic ion channels but keeping the same network setup of the original publication. One challenge is to explore the possibility of including more parameters, in addition to peak conductances, and assess if the genetic algorithm is robust enough to provide a set of optimal parameters correlated with those computed in this work.

Another interesting issue involves adapting our approach to calculate also the confidence interval of every single parameter wherein the model output does not deviate considerably from the optimal behavior. There are cases in which small deviations of parameters from their optimal values put the system into a different dynamical regime. Finding the bounds of the optimal regime of each parameter would help neuroscientists to better understand the mechanisms underlying the neural function.

Acknowledgments

This work has been supported by the Human Brain Project (FET project 604102), Spanish National Grants TIN2013-47069-P and TIN2012-32039, projects

P11-TIC-7983 and P11-TIC-8120 of Junta of Andalucia (Spain), co-financed by the European Regional Development Fund (ERDF), and the Spanish Government PhD scholarship FPU13/01487.

References

[1] W. Van Geit, E. De Schutter, P. Achard, Automated neuron model optimization techniques: a review, Biological cybernetics 99 (4-5) (2008) 241–251.

[2] S. Druckmann, Y. Banitt, A. Gidon, F. Schürmann, H. Markram, I. Segev, A novel multiple objective optimization framework for constraining conductance-based neuron models by experimental data, Frontiers in neuroscience 1 (1) (2007) 7.

[3] W. C. Gerken, L. Purvis, R. J. Butera, Genetic algorithm for optimization and specification of a neuron model, Neurocomputing 69 (10) (2006) 1039–1042.

[4] C. M. Weaver, S. L. Wearne, The role of action potential shape and parameter constraints in optimization of compartment models, Neurocomputing 69 (10) (2006) 1053–1057.

[5] D. Haufler, F. Morin, J. Lacaille, F. K. Skinner, Parameter estimation in single-compartment neuron models using a synchronization-based method, Neurocomputing 70 (10) (2007) 1605–1610.

[6] A. Pettinen, O. Yli-Harja, M.-L. Linne, Comparison of automated parameter estimation methods for neuronal signaling networks, Neurocomputing 69 (10) (2006) 1371–1374.

[7] A. Wohrer, P. Kornprobst, Virtual retina: a biological retina model and simulator, with contrast gain control, Journal of computational neuroscience 26 (2) (2009) 219–249.

[8] S. A. Baccus, B. P. Ölveczky, M. Manu, M. Meister, A retinal circuit that computes object motion, The Journal of Neuroscience 28 (27) (2008) 6807–6817.

[9] J. Hérault, B. Durette, Modeling visual perception for image processing, in: Computational and Ambient Intelligence, Springer, 2007, pp. 662–675.

[10] G. T. Einevoll, H. E. Plesser, Extended difference-of-gaussians model incorporating cortical feedback for relay cells in the lateral geniculate nucleus of cat, Cognitive neurodynamics 6 (4) (2012) 307–324.

[11] N. Yousif, M. Denham, The role of cortical feedback in the generation of the temporal receptive field responses of lateral geniculate nucleus neurons: a computational modelling study, Biological cybernetics 97 (4) (2007) 269–277.

[12] F. Hayot, D. Tranchina, Modeling corticofugal feedback and the sensitivity of lateral geniculate neurons to orientation discontinuity, Visual neuroscience 18 (06) (2001) 865–877.

[13] Y. Ozuysal, S. A. Baccus, Linking the computational structure of variance adaptation to biophysical mechanisms, Neuron 73 (5) (2012) 1002–1015.

[14] V. Mante, V. Bonin, M. Carandini, Functional mechanisms shaping lateral geniculate responses to artificial and natural stimuli, Neuron 58 (4) (2008) 625–638.

[15] H. van Hateren, A cellular and molecular model of response kinetics and adaptation in primate cones and horizontal cells, Journal of vision 5 (4) (2005) 5.

[16] M. Mitchell, An introduction to genetic algorithms, MIT press, 1998.

[17] H. J. Alitto, T. G. Weyand, W. M. Usrey, Distinct properties of stimulus-evoked bursts in the lateral geniculate nucleus, The Journal of neuroscience 25 (2) (2005) 514–523.

[18] S. A. Baccus, M. Meister, Fast and slow contrast adaptation in retinal circuitry, Neuron 36 (5) (2002) 909–919.

[19] V. C. Smith, J. Pokorny, B. B. Lee, D. M. Dacey, Primate horizontal cell dynamics: an analysis of sensitivity regulation in the outer retina, Journal of Neurophysiology 85 (2) (2001) 545–558.

[20] P. Murphy, A. Sillito, Corticofugal feedback influences the generation of length tuning in the visual pathway.

[21] M. C. Vanier, J. M. Bower, A comparative survey of automated parameter-search methods for compartmental neural models, Journal of computational neuroscience 7 (2) (1999) 149–171.

[22] T. Blickle, L. Thiele, A comparison of selection schemes used in evolutionary algorithms, Evolutionary Computation 4 (4) (1996) 361–394.

[23] K. Deb, A. Pratap, S. Agarwal, T. Meyarivan, A fast and elitist multiobjective genetic algorithm: Nsga-ii, Evolutionary Computation, IEEE Transactions on 6 (2) (2002) 182–197.

[24] F.-A. Fortin, F.-M. De Rainville, M.-A. Gardner, M. Parizeau, C. Gagné, DEAP: Evolutionary algorithms made easy, Journal of Machine Learning Research 13 (2012) 2171–2175.

[25] W. Gropp, E. Lusk, A. Skjellum, Using MPI: portable parallel programming with the message-passing interface, Vol. 1, MIT press, 1999.

[26] L. D. Dalcin, R. R. Paz, P. A. Kler, A. Cosimo, Parallel distributed computing using python, Advances in Water Resources 34 (9) (2011) 1124–1139.

[27] J. Granahan, J. Sweet, An evaluation of atmospheric correction techniques using the spectral similarity scale, in: Geoscience and Remote Sensing Symposium, 2001. IGARSS'01. IEEE 2001 International, Vol. 5, IEEE, 2001, pp. 2022–2024.

[28] A. Rodríguez, J. L. Nieves, E. Valero, E. Garrote, J. Hernández-Andrés, J. Romero, Modified fuzzy c-means applied to a bragg grating-based spectral imager for material clustering, in: IS&T/SPIE Electronic Imaging, International Society for Optics and Photonics, 2012, pp. 83000J–83000J.

[29] P. Martínez-Cañada, C. Morillas, B. Pino, E. Ros, F. Pelayo, A computational framework for realistic retina modeling, International Journal of Neural Systems. Under review.

[30] P. Martínez-Cañada, C. Morillas, B. Pino, F. Pelayo, Towards a generic simulation tool of retina models, in: Artificial Computation in Biology and Medicine, Springer, 2015, pp. 47–57.

[31] P. Martínez-Cañada, C. Morillas, S. Romero, F. Pelayo, Modeling retina adaptation with multiobjective parameter fitting, in: Advances in Computational Intelligence, Springer, 2015, pp. 175–184.

[32] S. Hill, G. Tononi, Modeling sleep and wakefulness in the thalamocortical system, Journal of neurophysiology 93 (3) (2005) 1671–1698.

[33] J. M. Eppler, et al., NEST 2.8.0. Zenodo. (2015).
URL `http://dx.doi.org/10.5281/zenodo.32969`

[34] W. Van Geit, P. Achard, E. De Schutter, Neurofitter: a parameter tuning package for a wide range of electrophysiological neuron models, BMC Neuroscience 8 (Suppl 2) (2007) P5.

Appendix C

PLOS | COMPUTATIONAL BIOLOGY

RESEARCH ARTICLE

Biophysical network modeling of the dLGN circuit: Effects of cortical feedback on spatial response properties of relay cells

Pablo Martínez-Cañada[1,2], Milad Hobbi Mobarhan[3,4], Geir Halnes[3,5], Marianne Fyhn[3,4], Christian Morillas[1,2], Francisco Pelayo[1,2], Gaute T. Einevoll[3,5,6]*

1 Department of Computer Architecture and Technology, University of Granada, Granada, Spain, **2** Centro de Investigación en Tecnologías de la Información y de las Comunicaciones (CITIC), University of Granada, Granada, Spain, **3** Center for Integrative Neuroplasticity (CINPLA), University of Oslo, Oslo, Norway, **4** Department of Biosciences, University of Oslo, Oslo, Norway, **5** Faculty of Science and Technology, Norwegian University of Life Sciences, Ås, Norway, **6** Department of Physics, University of Oslo, Oslo, Norway

* gaute.einevoll@nmbu.no

Abstract

Despite half-a-century of research since the seminal work of Hubel and Wiesel, the role of the dorsal lateral geniculate nucleus (dLGN) in shaping the visual signals is not properly understood. Placed on route from retina to primary visual cortex in the early visual pathway, a striking feature of the dLGN circuit is that both the relay cells (RCs) and interneurons (INs) not only receive feedforward input from retinal ganglion cells, but also a prominent feedback from cells in layer 6 of visual cortex. This feedback has been proposed to affect synchronicity and other temporal properties of the RC firing. It has also been seen to affect spatial properties such as the center-surround antagonism of thalamic receptive fields, i.e., the suppression of the response to very large stimuli compared to smaller, more optimal stimuli. Here we explore the spatial effects of cortical feedback on the RC response by means of a a comprehensive network model with biophysically detailed, single-compartment and multi-compartment neuron models of RCs, INs and a population of orientation-selective layer 6 simple cells, consisting of pyramidal cells (PY). We have considered two different arrangements of synaptic feedback from the ON and OFF zones in the visual cortex to the dLGN: phase-reversed ('push-pull') and phase-matched ('push-push'), as well as different spatial extents of the corticothalamic projection pattern. Our simulation results support that a phase-reversed arrangement provides a more effective way for cortical feedback to provide the increased center-surround antagonism seen in experiments both for flashing spots and, even more prominently, for patch gratings. This implies that ON-center RCs receive direct excitation from OFF-dominated cortical cells and indirect inhibitory feedback from ON-dominated cortical cells. The increased center-surround antagonism in the model is accompanied by spatial focusing, i.e., the maximum RC response occurs for smaller stimuli when feedback is present.

Citation: Martínez-Cañada P, Mobarhan MH, Halnes G, Fyhn M, Morillas C, Pelayo F, et al. (2018) Biophysical network modeling of the dLGN circuit: Effects of cortical feedback on spatial response properties of relay cells. PLoS Comput Biol 14(1): e1005930. https://doi.org/10.1371/journal.pcbi.1005930

Editor: Arnd Roth, University College London, UNITED STATES

Received: June 4, 2017

Accepted: December 17, 2017

Published: January 29, 2018

Data Availability Statement: The scripts needed to run our models is available from https://github.com/CINPLA.

Funding: This research has been supported by the Human Brain Project (FET project 604102) and the Research Council of Norway (BIOTEK2021 Digital Life project 'DigiBrain', project 248828). PMC was supported by the PhD scholarship FPU13/01487 and the research stay grant EST15/00055, both awarded by the Government of Spain, FPU program. The funders had no role in study design, data collection and analysis, decision to publish, or preparation of the manuscript.

Competing interests: The authors have declared that no competing interests exist.

Author summary

The functional role of the dorsal lateral geniculate nucleus (dLGN), placed on route from retina to primary visual cortex in the early visual pathway, is still poorly understood. A striking feature of the dLGN circuit is that dLGN cells not only receive feedforward input from the retina, but also a prominent feedback from cells in the visual cortex. It has been seen in experiments that cortical feedback modifies the spatial properties of dLGN cells in response to visual stimuli. In particular, it has been shown to increase the center-surround antagonism for flashing-spot and patch-grating visual stimuli, i.e., the suppression of responses to very large stimuli compared to smaller stimuli. Here we investigate the putative mechanisms behind this feature by means of a comprehensive network model of biophysically detailed neuron models for RCs and INs in the dLGN and orientation-selective cortical cells providing the feedback. Our results support that the experimentally observed feedback effects may be due to a phase-reversed ('push-pull') arrangement of the cortical feedback where ON-symmetry RCs receive (indirect) inhibitory feedback from ON-dominated cortical cell and excitation from OFF-dominated cortical cells, and vice versa for OFF-symmetry RCs.

Introduction

Visual signals from the retina pass through the dorsal geniculate nucleus (dLGN), the visual part of thalamus, on the way to the visual cortex. However, this is not simply a one-way flow of information: cortical cells feed back to both relay cells (RCs) and interneurons (INs) in the dLGN and thus shape the transfer of visual information in the circuit [1–6]. Although there is no broad consensus about the effects of cortical feedback on sensory processing, there are many experimental studies that provide insight into its potential roles [7–20]. For example, cortical feedback has been observed to switch the response mode of RCs between tonic and burst modes [21, 22] and to synchronize the firing patterns of groups of dLGN cells [17]. Further, the studies have reported both enhanced and reduced responses of dLGN neurons from cortical feedback, and the functional role of cortical feedback is still debated [3, 23, 24].

One line of inquiry has addressed the question of how cortical feedback modulates the receptive-field properties of RCs. Cortical feedback was early shown to affect the length tuning of RC responses [12], and a series of studies from Sillito and co-workers have investigated how cortical feedback influences the RC responses to flashing spots and patch gratings, i.e., circular patches of drifting gratings [4, 13, 15, 16, 18, 19]. Retinal ganglion cells (GCs) provide the feedforward input to the dLGN circuit, and the receptive fields of both GCs and RCs have a roughly circular shape where an excitatory center is surrounded by an inhibitory surround [25–27]. For a flashing-spot stimulus the maximum response occurs for a spot centered on the receptive field which exactly covers the receptive-field center [27]. When the spot size is gradually increased to also stimulate the inhibitory surround, the response is gradually reduced until the entire surround is also covered. This phenomenon is referred to as *center-surround suppression*, and it is known that such suppression is increased for RCs compared to the GCs that provide the dominant feedforward input [27]. A part of this increased suppression likely stems from feedforward mechanisms in the dLGN circuit, i.e., a broad feedforward retinal input to LGN interneurons, in turn providing increased feedforward surround inhibition to the RCs [27, 28]. Increased center-surround suppression implies that the neurons are less responsive to broad visual stimuli and instead more tuned to narrow stimuli or sharp spatial variations in the visual scene. Thus dynamical tuning of this suppression may be a mechanism for the nervous system to adapt to changing light conditions and viewing demands to create an efficient representation of the stimulus [29].

Although the receptive fields of dLGN cells appear largely determined by the feedforward retinogeniculate input, corticothalamic feedback has been shown to increase the inhibitory surround, i.e., increase the suppression to very large stimuli [4, 12, 13, 15, 16, 19, 30]. Other studies have reported enhanced responses of dLGN neurons [18, 30, 31] when using smaller stimuli. Interestingly, cortical feedback has been experimentally observed to increase the surround suppression both for flashing spots [32] and patch gratings [4, 19], though, the increase has been found to be larger for patch gratings [2, 4]. The topic of the present modeling study is to investigate what aspects of the thalamocortical loop, and in particular what type of cortical feedback pattern, may underlie these observed changes in RC center-surround antagonism.

While the use of computational modeling to study the effect of cortical feedback on visual processing is not new, previous projects have investigated feedback effects on the temporal processing of RCs [33–38]. Modeling studies of spatial aspects have to our knowledge been limited to relatively simple firing-rate models [39, 40] where, for example, dLGN INs have not been explicitly included. The focus in [39] was on exploring cortical feedback effects on observed effects of RC responses to discontinuity in orientations in gratings in bipartite stimuli. In [40] the *extended DOG* (eDOG) model was introduced, allowing for analytical explorations of effects of cortical feedback in certain settings, i.e., with certain combinations of excitatory and (indirect) inhibitory feedback from ON- and OFF-center cortical cells onto RCs. In that study a preliminary use-case showed that a phase-reversed ('push-pull') arrangement of cortical feedback where ON-center RCs receive direct excitation from OFF-driven cortical cells and balanced indirect inhibitory feedback from ON-driven cortical cells, may provide increased center-surround antagonism.

Here we instead consider a biophysically detailed model where RCs and INs, as well as orientation-selective layer-6 pyramidal cortical cells (PYs), are explicitly included. The model is an extension of a recently developed network model of the feedforward part of the dLGN circuit [41]. The neuron models include a host of Hodgkin-Huxley type active conductances [42–44], and an important feature is the multicompartment IN model that incorporates both axonal and triadic inhibition of RCs [45]. Another key element of our model circuit is the explicit incorporation of both ON-symmetry and OFF-symmetry cells which, unlike for the rate-based eDOG model [40], allows exploration of a wide range of putative synaptic patterns for the feedback from cortical cells to RCs and INs, i.e., both same symmetry (ON to ON, OFF to OFF) and cross-symmetry (ON to OFF, OFF to ON). By comparing results from a wide range of feedback patterns, we find that our results support that a phase-reversed arrangement of the cortical feedback seems most effective in increasing the center-surround antagonism observed both for flashing spots and, even more significantly, for patch gratings.

Methods

Overview of the network model and feedforward connections

The core of the network model comprises two-dimensional grids of synaptically connected dLGN and cortical neurons of ON and OFF receptive-field arrangements. The network is driven by dLGN neurons that receive spikes encoding visual input from the retina. The network includes populations of retinal ganglion cells (GC), dLGN RCs and INs, and PYs of layer 6 in the primary visual cortex (Fig 1). Each layer is scaled to span a monocular patch of 10 deg × 10 deg in the visual field and contains 10 × 10 neurons of each symmetry type (ON/OFF), except in the case of dLGN INs for which there are 25 per symmetry type (20% of the total number of dLGN cells [46]). Based on the wiring rules of the cat dLGN, it has been

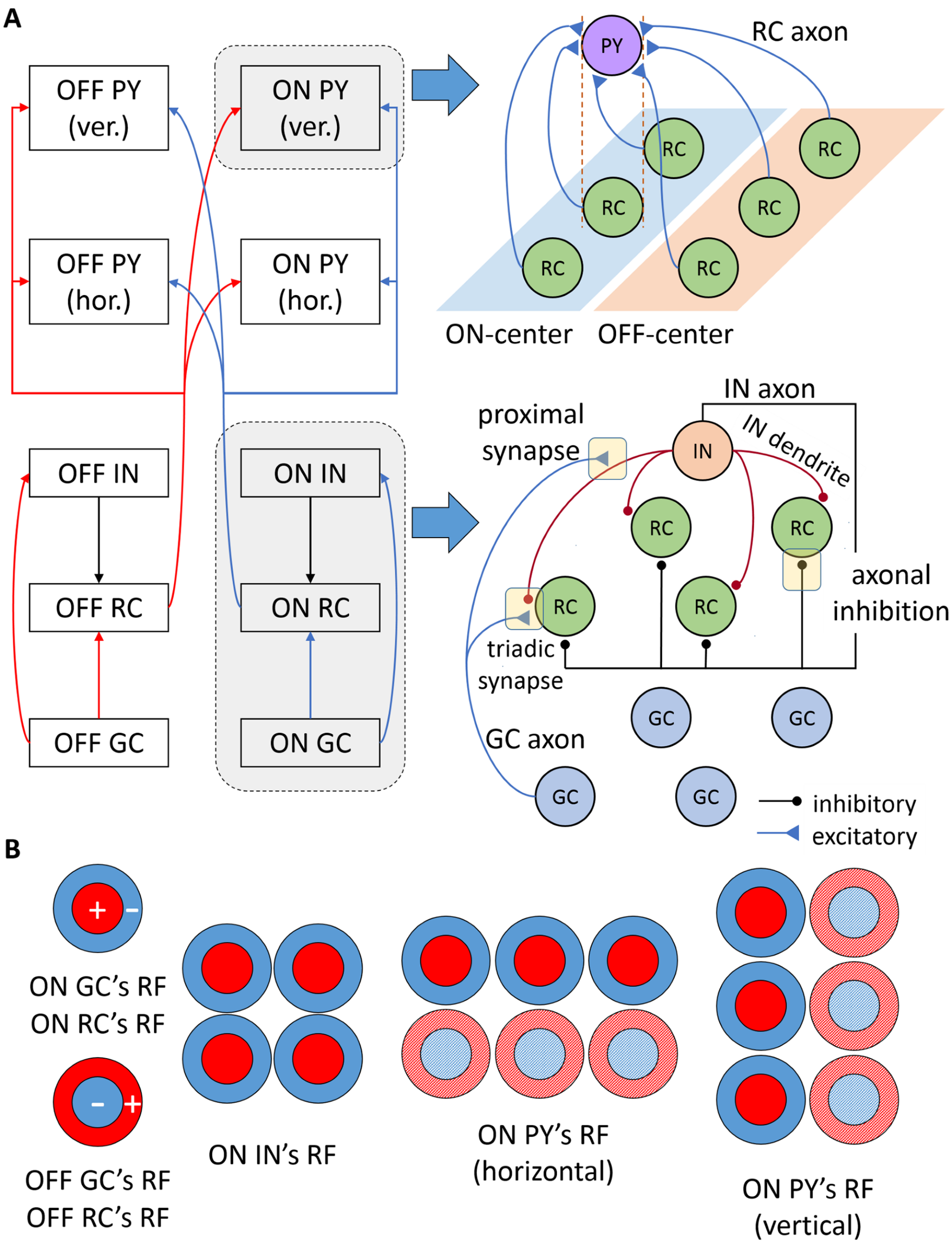

Fig 1. Schematic of the model circuit and feedforward connections. A: Neuronal populations and their connectivity patterns. On the left, each arrow represents synaptic connections between a source and a target population. On the right, a detailed view is shown of the spatial organization of input synapses for an ON-center PY (top) and for RCs and INs in the LGN (bottom). PYs with ON symmetry receive strong input from an elongated area of three ON-symmetry RCs and weak input from an adjacent row of three OFF-symmetry RCs. In the LGN, every IN receives input from GCs via the triadic synapse and the proximal IN dendrite. RCs are contacted by the IN axon, receiving axonal

inhibition, and by the IN dendrite at the triadic synapse, resulting in direct triadic inhibition. For the sake of clarity, only excitatory connections of a single GC to the IN are shown. B: Illustration of formation of receptive fields at each stage based on the spatial arrangement of receptive fields of the synaptic afferents. RCs with ON (OFF) symmetry receive input from single ON-symmetry (OFF-symmetry) GCs with circular center-surround receptive fields. INs with ON symmetry receive input from four ON-symmetry GCs. The strong flank of the PY's receptive field is shown in solid color and the weak flank is represented by a pattern fill. PYs both with horizontal and vertical orientation-selectivity are shown.

https://doi.org/10.1371/journal.pcbi.1005930.g001

estimated that a 1 deg × 1 deg patch of the dLGN contains about 10 RCs of one symmetry type on average at an eccentricity of 7 deg [47]. Thus, one simulated RC in our model would correspond to about 10 RCs of the cat dLGN. In the tuning of the model, we have chosen model parameters giving GC and RC responses similar to the cat experiments described in [27, 28]. Here the recordings were done on cells with receptive fields centered in areas of the visual field some distance away from the center of gaze (*area centralis* in cat).

Retinal GCs have a circularly symmetric center-surround receptive field that is inherited by dLGN RCs through one-to-one excitatory synapses as shown for cells of the ON and OFF pathways in Fig 1. In these receptive fields, the center and surround present an antagonistic push-pull arrangement [48]. A bright stimulus confined to the center of the ON-cell receptive field or a dark stimulus placed on the surround of the receptive field evoke a depolarization of the ON cell. By contrast, an ON cell is hyperpolarized by projecting either a dark stimulus to the center of the receptive field or a bright stimulus to the surround. The opposite behavior applies for OFF-center cells.

The feedforward elements of the dLGN are the same as in [41]. LGN INs receive input from four retinal ganglion cells via the triadic synapses and the proximal IN dendrites. RCs receive axonal inhibition through the IN axon and triadic inhibition by the IN dendrites at the triadic synapses, resulting in fast inhibition.

The cortical populations of PYs receive strong input from an elongated area of three RCs of the same symmetry and weak input from an adjacent row of three RCs of the opposite symmetry. PYs come in two different orientation-selectivity variants: horizontally-selective or vertically-selective. Further, each of these two cortical populations also come with ON and OFF symmetry making a total of four distinct cortical populations. This is a simplified representation of the thalamocortical loop as it neglects that the strongest thalamic input to primary visual cortex arrives in layer 4 while the feedback inputs to dLGN cells come from cells in layer 6.

The models for the dLGN and cortical neurons are all biophysically detailed in the sense that they include a variety of Hodgkin-Huxley type active conductances explicitly reproducing generation of action potentials. The GC spiking mechanism is not modeled explicitly, instead this input is modeled by means of phenomenological filter models as in [41].

Retinal input

Descriptive filter model of retinal ganglion cells. The input spike trains from GCs were generated by non-stationary Poisson processes with firing rates determined by a response function $R_g(\boldsymbol{r}, t)$. The response function $R_g(\boldsymbol{r}, t)$ is defined as a non-separable center-surround filter that takes into account the additional delay between the center and surround signals [49–51]:

$$R_g^{ON}(\boldsymbol{r}, t) = H[C(r, t) - S(r, t)]. \tag{1}$$

Here the response is the difference between the center signal, $C(\boldsymbol{r}, t)$, and the surround signal, $S(\boldsymbol{r}, t)$. $H[x] = x\theta(x)$ is introduced to enforce nonnegative firing rates, where $\theta(x)$ is the

Heaviside step function. The difference between the center and the surround is reversed for the OFF-center ganglion cell:

$$R_{\mathrm{g}}^{\mathrm{OFF}}(\boldsymbol{r},t) = H[S(\boldsymbol{r},t) - C(\boldsymbol{r},t)]. \tag{2}$$

The center and surround signals are obtained by convolution between the stimulus signal, $s(\boldsymbol{r}, t)$, and linear spatial (G_{a_C}, G_{a_S}) and temporal ($T_{n_\mathrm{O},\tau_\mathrm{O}}$, $E_{n_\mathrm{C},\tau_\mathrm{C}}$, $E_{n_\mathrm{S},\tau_\mathrm{S}}$) filters:

$$C(\boldsymbol{r},t) = G_{a_\mathrm{C}}(\boldsymbol{r}) * T_{n_\mathrm{O},\tau_\mathrm{O}}(t) * E_{n_\mathrm{C},\tau_\mathrm{C}}(t) * s(\boldsymbol{r},t), \tag{3}$$

$$S(\boldsymbol{r},t) = \omega * G_{a_\mathrm{S}}(\boldsymbol{r}) * E_{n_\mathrm{S},\tau_\mathrm{S}}(t) * s(\boldsymbol{r},t). \tag{4}$$

Temporal filters $E_{n,\tau}(t)$ are normalized low-pass filters implemented as an exponential cascade:

$$E_{n,\tau}(t) = \frac{(nt)^n e^{-nt/\tau}}{\tau^{n+1}(n-1)!}, \tag{5}$$

where τ is the time constant and n the number of low-pass filtering stages. $T_{n_\mathrm{O},\tau_\mathrm{O}}$ is a high-pass temporal filter that modulates the overshoot that follows the stimulus onset, observed experimentally [25, 27]. It is computed as the difference between the Dirac function, weighted by the overshoot amplification factor β, and a low-pass temporal filter:

$$T_{n_\mathrm{O},\tau_\mathrm{O}}(t) = \beta\delta_0(t) - E_{n_\mathrm{O},\tau_\mathrm{O}}(t). \tag{6}$$

Spatial filters are implemented by means of the well-known normalized Gaussian function [25, 28, 49, 50]:

$$G_a(\boldsymbol{r}) = \frac{1}{\pi a^2} e^{-r^2/a^2}, \tag{7}$$

with a the spatial extent of the kernel. Thus, a_C defines the size of the center receptive field and a_S, of the surround.

Visual stimuli. With the spatiotemporal stimulus function $s(\boldsymbol{r}, t)$ specified, the GC response can be computed by means of Eqs 1 and 2. The two main visual stimuli explored in the present work were (i) flashing circular spots and (ii) circular drifting patch gratings. In addition, separate simulations with flashed bright and dark spots within the ON and OFF subregions of different cell types were done to map out the receptive fields.

Each trial of the flashing-spot stimulus consisted of a 500 ms period of full-field isoluminant background followed by a 500 ms period in which the circular spot was superimposed on the background. The luminance profile of the flashing-spot stimulus can be described mathematically as

$$L(\boldsymbol{r},t) = \begin{cases} L_{\mathrm{bkg}} & \text{for } t < 500\,\mathrm{ms}, \\ L_{\mathrm{bkg}}(1-\theta(d_s/2 - r)) + L_{\mathrm{stim}}(1-\theta(r-d_s/2)) & \text{for } 500\,\mathrm{ms} \le \mathrm{t} < 1000\,\mathrm{ms}, \end{cases} \tag{8}$$

where d_s is the diameter of the circular spot. The circular spot was concentric with the receptive field of the central GC, located in the 6th row and 6th column of the 10 × 10 grid where we set $\boldsymbol{r} = 0$. In our formalism the stimulus $s(\boldsymbol{r}, t)$ is represented via an (unspecified) sigmoidal function of the luminance $L(\mathbf{r}, t)$, that is, $s(\mathbf{r}, t) = l(L(\mathbf{r}, t))$, where l is a sigmoidal *activity function* of some form, converting luminance to firing rates [28].

For the second stimulus, a circular patch of sinusoidal grating with horizontal orientation was presented for 2000 ms on a full-field isoluminant background. The luminance profile of this stimulus can mathematically be described as [40]:

$$L(\mathbf{r},t) = L_{\mathrm{bkg}} + (L_{\mathrm{stim}} - L_{\mathrm{bkg}})(1 - \theta(r - d_{\mathrm{pg}}/2))\cos(\boldsymbol{k}_{\mathrm{pg}}\boldsymbol{r} - \omega_{\mathrm{pg}}t), \tag{9}$$

k_{pg} and ω_{pg} are the wave vector and the angular frequency of the patch grating, respectively, and d_{pg} is the diameter of the circular patch. Note that a circular spot stimulus is obtained for $|\boldsymbol{k}_{\mathrm{pg}}| = \omega_{\mathrm{pg}} = 0$. $\nu_{\mathrm{pg}} = |\boldsymbol{k}_{\mathrm{pg}}|/2\pi$ and $f_{\mathrm{pg}} = \omega_{\mathrm{pg}}/2\pi$ are the spatial and temporal frequencies of the patch grating, respectively. In the present applications we used $\nu_{\mathrm{pg}} = 0.15$ cycles/ deg and $f_{\mathrm{pg}} = 1$ Hz. While the activity function $l(L)$ could have an arbitrary sigmoidal form for the flashing-spot stimulus, it is assumed to be linear for the patch-grating stimulus, i.e., $s(\mathbf{r}, t) = l(L(\mathbf{r}, t))$, where l is of the form $l(x) = cx$ for some (unspecified) constant c [52].

The spatial part of the convolution between the stimulus and $G_{a_{\mathrm{C}}}$ and $G_{a_{\mathrm{S}}}$ can be computed analytically both when the Gaussian is concentric with the spot stimulus and when it is non-concentric [28, 40]. Parameters listed in Table 1 were tuned to approximate simultaneously the spatial properties of the GC response to the experimental results obtained with a spot stimulus [27] and the temporal properties to the range of values reported by Usrey et al. [53]. The two values of $l_{\mathrm{bkg}} \equiv l(L_{\mathrm{bkg}})$ and $l_{\mathrm{stim}} \equiv l(L_{\mathrm{stim}})$ in Table 1 correspond to the GC response for the flashing spot (left) and the patch grating (right). A larger background level was used for the patch-grating stimulus to avoid rectification of the GC response for the negative period of the sinusoid and to assure a roughly linear GC response.

Neuron models

dLGN interneuron (IN). We used the same IN and RC models as in previous work [41]. The IN model consisted of a cylindrical soma of radius 8.72 μm and length 15.3 μm, with four identical linear 'stick'-like dendrites of length 500 μm, a set of passive membrane properties, and seven active channel conductances including the traditional Hodgkin-Huxley type sodium and potassium channels for generating action potentials, a hyperpolarization-activated cation channel, a low-threshold, T-type calcium channel, a high-threshold, L-type calcium channel, a medium-duration, calcium-dependent afterhyperpolarization channel, and a long-lasting calcium-activated non-specific cation channel. The IN model was an adapted version of the

Table 1. Parameters of the response function of GCs. The two values of l_{bkg} and l_{stim} in the last two rows correspond to the GC response for the flashing spot (left) and the patch grating (right).

Parameter	Description	Units	Value	
β	Overshoot amplification factor		2.0	
ω	Center-surround relative strength		0.85	
n_{O}	Filtering stages of the overshoot		1.0	
τ_{O}	Time constant of the overshoot	ms	30.0	
n_{C}	Filtering stages of the center signal		4.0	
τ_{C}	Time constant of the center signal	ms	20.0	
n_{S}	Filtering stages of the surround signal		5.0	
τ_{S}	Time constant of the surround signal	ms	50.0	
a_{C}	Center width	deg	0.62	
a_{S}	Surround width	deg	1.26	
ν_{pg}	Spatial frequency of the patch grating	cycles/ deg	0.15	
f_{pg}	Temporal frequency of the patch grating	Hz	1.0	
$l_{\mathrm{bkg}}(1-\omega)$	GC response rate to the background	s^{-1}	36.8	78.75
$l_{\mathrm{stim}}(1-\omega)$	GC response rate to the stimulus	s^{-1}	56.5	89.25

https://doi.org/10.1371/journal.pcbi.1005930.t001

multicompartmental interneuron model in [45, 54]. For a list of the model parameters, see Table 2 in [41].

dLGN relay cell (RC). RCs can be considered electronically compact [55] and thus we used a single-compartment model. The RC model corresponds to the model in [42] and includes the standard Hodgkin-Huxley type sodium and potassium channels, as well as the T-type calcium channel. While most of the parameters of the RC model are maintained as in [41], the maximal conductance of the T-type calcium channel, g_{CaT}, was reduced to 0.2 mS/cm^2 to force the RC to respond in the tonic firing mode even with strong disynaptic inhibition from cortical cells. For further details on the model parameters, see Table 4 in [41].

Cortical pyramidal cell (PY). The thalamocortical feedback loop in mammalian brain involves more than just a single cortical population and a single cortical layer. Both neurophysiological and neuroanatomical studies have shown that layers 4 and 6 of the visual cortex are the main postsynaptic targets of the geniculate inputs and that dLGN cells receive cortical-feedback afferents only from layer 6 of the visual cortex (reviewed in [2, 4, 5]). While a monosynaptic excitatory feedback loop thalamus-cortex-thalamus involving only layer 6 is possible, intracortical processing is expected to affect the action of the thalamocortical feedback loop. Detailed modeling of this intracortical processing is beyond the scope of this work, and we instead represented the effect of cortical feedback in a reduced way by neglecting the layered organization of cortical processing (which is in accordance with other modeling approaches [33, 35, 38–40, 43]). Further, only one type of cortical neuron was included in the model, a PY.

The single-compartment model of cortical PYs was taken from [43, 44]. This model was originally developed to investigate spindle oscillations in a network of cortical neurons, thalamic reticular neurons and RCs. The model includes the classical Hodgkin-Huxley type sodium and potassium channels for action potential generation, and a slow voltage-dependent potassium channel, I_{M}. I_{M} accounts for the classic 'regular-spiking' behavior that generates adapting trains of action potentials in response to depolarizing current injection (see Fig 2). Parameters of this cell type are summarized in Table 2.

Synaptic connections in the network

Conductance-based synapses were assumed, i.e.,

$$I_{\mathrm{syn}}(t) = w f_{\mathrm{syn}}(t - t_{\mathrm{s}} - t_{\Delta})(V - E_{\mathrm{syn}})\theta(t - t_{\mathrm{s}} - t_{\Delta}), \tag{10}$$

for a presynaptic spike arriving at t_{s}. Here the weight w is the maximal conductance of the postsynaptic receptors and E_{syn} is the reversal potential. f_{syn} is the temporal envelope of the synaptic conductance modeled as the difference between two exponential functions specified by time constants τ_{rise} and τ_{decay} (Eqs. 6.4–6.6 in [56]). t_{Δ} is the conduction time delay from the generation of the presynaptic spike to the initiation of the postsynaptic response and was set to a fixed value of 1 ms for all synaptic connections. Action potentials of RCs, INs and PYs were detected by upward somatic voltage crossings at −10 mV.

While AMPA receptors mediate all excitatory connections in this model, GABA$_{\mathrm{A}}$ receptors mediate all inhibitory synaptic interactions. Parameters of synaptic connections are shown in Table 3. Parameters of retinogeniculate and intrathalamic connections remain similar to those presented in [41]. An exception is the GC input to the IN part of the triad, for which we reduced the synaptic weight to compensate for the added excitatory input from corticothalamic connections not present in the previous model [41].

Feedforward excitation and inhibition of RCs. Following our previous network scheme [41], each GC axon synapses at two different locations, i.e., in the triadic synapse where the RC and the IN receive excitatory input, and in a proximal IN dendrite, both dependent on AMPA

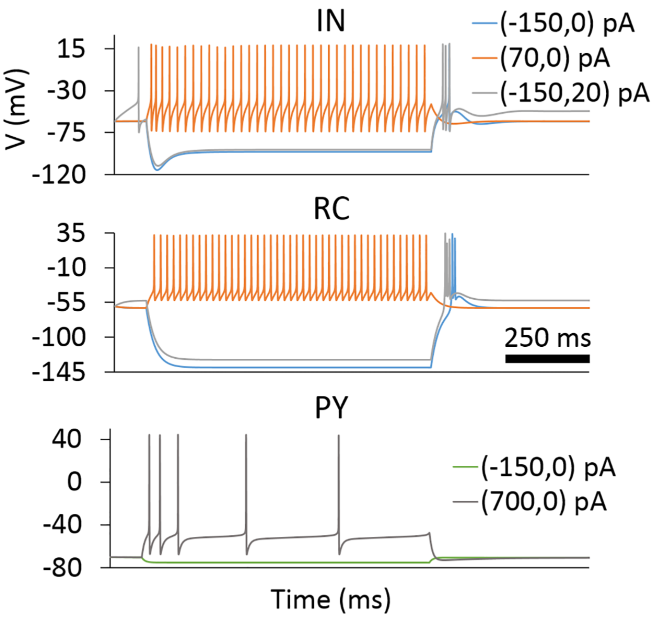

Fig 2. Spiking patterns of model neurons for somatic current injection. Somatic membrane potentials of the model neurons following injection of depolarizing (positive) and hyperpolarizing (negative) current steps lasting 900 ms (first of the two numbers in parenthesis). A depolarizing current step of 0 or 20 pA (second number in parenthesis) is applied afterwards.

https://doi.org/10.1371/journal.pcbi.1005930.g002

receptors. In particular, each GC synapses the IN in two spatially separated locations of the corresponding IN dendrite, either at the proximal dendrite (65 μm from the soma) or in the triadic synapse located distally on the dendrite (434 μm from the soma). Conversely, all four RCs are contacted by the IN axon, receiving the same $\mathrm{GABA_A}$ axonal inhibition, and by the IN dendrites at the triadic synapse, where local $\mathrm{GABA_A}$ release results in direct triadic inhibition. The triadic inhibition was modeled by means of Eq (10), and GABA release from the IN dendrites was assumed to occur whenever the local IN membrane potential at the triad crossed −10 mV (on the way upward).

Table 2. Parameters of cortical PY.

Parameter	Description	Units	Value
A	Neuron surface area	μm^2	28950
C_m	Membrane capacitance	$\mu F/cm^2$	1.0
R_m	Membrane resistivity	Ωcm^2	34000
E_{pas}	Passive leak reversal potential	mV	-70.0
g_{Na}	Max. Na conductance	mS/cm^2	50.0
E_{Na}	Na reversal potential	mV	50.0
g_K	Max. K conductance	mS/cm^2	5.0
E_K	K reversal potential	mV	-100.0
g_M	Max. M conductance	mS/cm^2	0.07

https://doi.org/10.1371/journal.pcbi.1005930.t002

Table 3. Parameters of synaptic connections. Each synaptic weight w represents a monosynaptic connection between each source and target cell. For corticothalamic connections, instead of one synaptic weight w, we compared the model response for a range of different values, between the listed values.

Receptor	Location	w (nS)	E_{syn} (mV)	τ_{rise} (ms)	τ_{decay} (ms)
AMPA	GC → IN triad	0.4	10.0	0.3	2.0
AMPA	GC → IN prox.	0.3	10.0	1.6	3.6
AMPA	GC → RC	15.6	10.0	0.1	1.2
$GABA_A$	IN triad → RC	6.0	-80.0	0.45	5.0
$GABA_A$	IN axon → RC	4.0	-60.0	0.45	5.0
AMPA	$RC^{ON} \rightarrow PY^{ON}$	50.0	10.0	0.2	1.2
AMPA	$RC^{OFF} \rightarrow PY^{ON}$	20.0	10.0	0.2	1.2
AMPA	PY → RC	0.0–6.0	10.0	0.2	1.2
AMPA	PY → IN dend.	0.0–6.0	10.0	0.2	1.2

https://doi.org/10.1371/journal.pcbi.1005930.t003

Thalamocortical connections. Receptive fields of simple cortical cells are orientation-selective, arising primarily from oriented convergence of thalamocortical excitatory inputs of ON and OFF elongated subregions of the dLGN [48, 57–59]. On average, simple cells present two to three subregions, each with a length/width ratio of 2.5. In addition, the width of the sub-region has been measured to match approximately the center of a geniculate receptive field [60, 61].

From these studies it appears that three geniculate receptive fields would be sufficient to cover one subregion of the cortical receptive field [60]. To impose such receptive fields on the cortical cells, receptive fields of model cortical PYs are formed by synaptic integration of 3 ON and 3 OFF RCs as shown in Fig 1. This minimal model of the cortical network is a base case scenario that facilitates the understanding of the key features of the circuit behavior and whose results can be easily extrapolated to more complex network architectures. Monosynaptic cortical excitation from RCs is assumed to be mediated by similar parameters of AMPA receptors as the retinal input.

Cortical feedback to LGN. Cortical feedback projections are mediated by a full set of cortical populations preferring different orientations [13], with a resulting net effect expected to be essentially isotropic [40]. In the model, only two orientation-selective populations are included, one preferring horizontal stimuli while the other preferring vertical stimuli.

The detailed arrangement of the synapses of the cortical afferents in dLGN is less known, and in the present work several possible arrangements were explored (see Fig 3). In terms of spatial symmetry of receptive fields, the arrangement can be either phase-matched (A) or phase-reversed (B). With the phase-reversed feedback, effects mediated by OFF-center cortical cell drive direct excitatory input to ON-center RCs (and the opposite for ON-center cortical cells on OFF-center RCs) [62]. In the phase-matched feedback, the ON-center cortical cell synapses both ON-center INs and RCs.

For each of the two options (A,B) above, we explored two configurations for the spatial extent of the corticothalamic axon: 1 × 1 and 2 × 2 (C). In the 1 × 1 feedback, every PY synapses one spatially overlapping RC and the corresponding IN dendrite. The 1 × 1 feedback was used as a theoretical base case scenario. It has, however, been demonstrated that individual corticothalamic axons innervate an area of the dLGN that extends significantly beyond the classical receptive fiels of RCs [63]. We thus also considered a case with a spatially more widespread feedback, i.e., a 2 × 2 feedback where every PY connects an extended region of 4 RCs and the four dendrites of the IN.

The majority of retinal terminals synapse on dendritic appendages of interneurons, while cortical synapses typically establish their connections on the dendritic trunks of interneurons

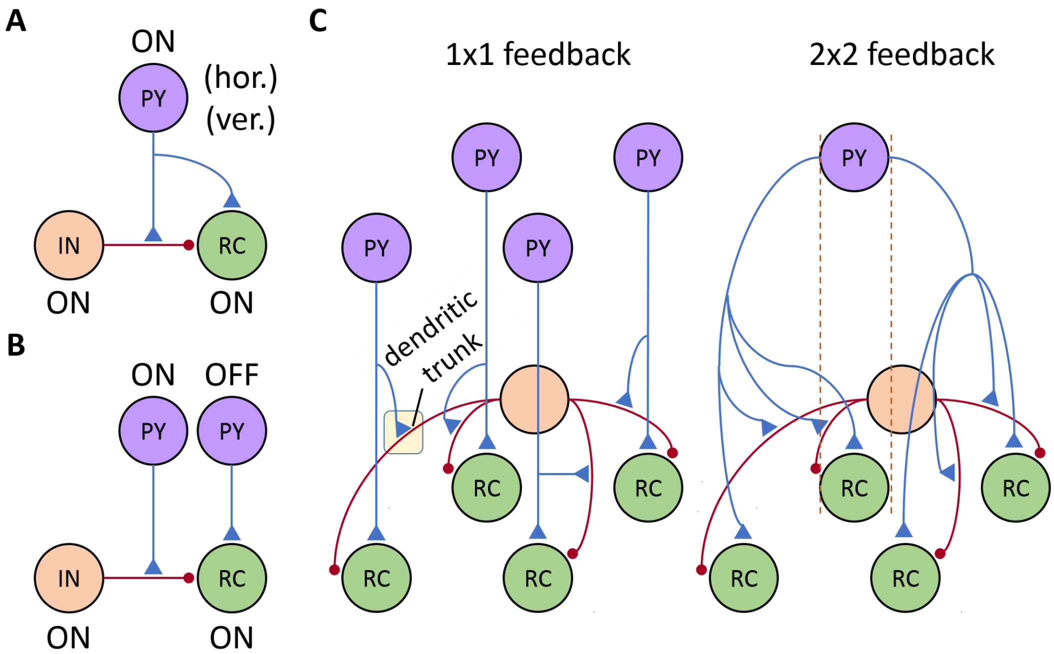

Fig 3. Cortical feedback configurations. Phase arrangements explored for connections between receptive fields of PYs and RCs: phase-matched (panel A) vs phase-reversed (panel B). Additionally, every RC receives feedback both from PYs with horizontal and vertical orientation-selectivity. C: The effect of the spatial spread of corticothalamic axons onto LGN cells is analyzed for another two feedback configurations: 1 × 1 and 2 × 2 cells. In the latter case, only synapses made by one PY are shown.

https://doi.org/10.1371/journal.pcbi.1005930.g003

[64]. In the model, we placed cortical synapses on the trunk, 391 μm from the soma. With this relatively distal location, the cortical synapses could contribute to triadic inhibition of relay cells, but had a relatively minor impact on the somatic action potential generation in INs, which is predominantly driven by retinal input [64, 65].

Simulation and analysis of results

Area-response curves. Area response curves were computed for two types of stimuli: flashing circular spots and patch gratings. Simulations were repeated by varying the spot diameter (patch diameter), ranging from smaller than, to larger than the receptive field center of the central RC. In particular, the spot diameter was increased from 0 to 10 degrees, every 0.2 degrees, giving a total of 51 different stimulus sizes. Raw poststimulus time histograms (PSTHs) were collected for all cells in the model. These PSTHs were averaged over 100 trials for the flashing spot and over 400 trials for the patch grating.

Averaged PSTHs were used to obtain the firing rates within specific time intervals of the stimulus. The firing rates for each stimulus diameter were used to construct the area-response curves, also known as area-summation curves [19, 27, 66]. For the flashing spot, each data point of the area-response curve corresponds to the mean firing rate computed during the second 500 ms period of the simulation [27].

A standard way to analyze the response for harmonically oscillating stimuli such as patch gratings is to compute the amplitude of the first harmonic. However, in the present simulations the duration of the patch-grating stimulus was too short to reliably compute this first-harmonic amplitude by a conventional Fourier transform. We instead estimated the amplitude of the first harmonic as follows: (1) Pick a time range corresponding to one complete period of of the oscillation. Here we chose the time period from 1000 to 2000 ms to avoid any transient effects from the upstart of the simulation. (2) Compute the DC component [67], i.e., the mean firing rate in this time window. (3) Subtract the DC component to the patch-grating response and (4) rectify the resulting signal by using the absolute value. The mean value of the rectified response over one full cycle corresponds to the mean rectified deviation of the response. For a sinusoidal modulation of the firing rate, this mean rectified deviation corresponds to $2/\pi \sim 0.64$ of the amplitude of the modulation.

Area-response curves were computed from the mean rectified deviation over one full cycle. The DC component was added to the mean rectified deviation to facilitate a visual comparison, in absolute terms, between the flashing-spot and patch-grating results. The area-response curves of both the flashing circular spots and patch gratings were filtered with a seven-point rectangular window to produce smoother curves. Additionally, the 0-degree response was added to the interpolated area-response curve to have the reference of background firing for computing the normalized response.

The normalized firing rate of area-response curves $\hat{R}(d)$ is calculated as

$$\hat{R}(d) = \frac{R(d) - \min(R(d))}{\max(R(d) - \min(R(d)))}, \tag{11}$$

where $R(d)$ is the unnormalized area-response. Two quantities extracted from the area-response curves are of particular interest here: the stimulus diameter giving the largest response (corresponding to the RF center size for the case of flashing spots) and the center-surround antagonism coefficient [27, 28]:

$$\alpha = 100\% \cdot (R_c - R_{cs})/(R_c - R_{bkg}), \tag{12}$$

where R_c is the maximum response, R_{cs} is the minimum response to spot/patch diameters larger than the receptive field center diameter, and R_{bkg} is the background firing rate. α provides a measure of the receptive-field surround suppression, where a value of 100% means that the surround suppression is strong enough to cancel out the visually-driven response to center stimulation.

Receptive fields. We here used two types of receptive fields: both the traditional *spike receptive field* where the trial-averaged spiking response to visual test stimuli is considered [26, 68] and the *membrane-potential receptive field* where the corresponding trial-averaged membrane-potential response is considered [48, 69].

We characterized the spike receptive fields of RCs and PYs by computing their spatiotemporal profiles (*x*-*y*-*t* receptive field maps and *x*-*t* plots) [26, 68]. The space was divided in a grid of 20 × 20 sampling points, i.e., one point every 0.25 degrees, and bright and dark spots were briefly flashed for 40 ms at every point. For every trial we ran a simulation of 300 ms where the spot was ON from 100 to 140 ms. PSTHs of the center cell (located in the 6th row and 6th column of the 10 × 10 grid) were collected and averaged across 100 trials. The spot has a diameter of 1 degree, which is the optimal stimulus size to cover the thalamic receptive field and was flashed at 50% contrast.

A composite receptive-field profile is obtained by computing the difference between the PSTHs for the bright and dark stimuli [68]. With this approach we obtained a complete *x*-*y*-*t* receptive field map over a range of values of *t*. Given that *x* is the dimension that cuts across the elongated bright- and dark-excitatory subregions, we integrated along *y* the different *x*-*y* receptive field maps at spaced time intervals (10 ms) to obtain the *x*-*t* plot. Plots were smoothed with the use of a Gaussian filter ($\sigma = 1$ deg) and displayed as contour plots.

To further characterize the spike receptive fields of PYs we used a measure to assess the spatial segregation of subregions within the receptive field, the *overlap index*, as described in references [48, 69]. The overlap index was computed as follows:

$$\textit{Overlap index} = \frac{0.5W_\mathrm{p} + 0.5W_\mathrm{n} - D}{0.5W_\mathrm{p} + 0.5W_\mathrm{n} + D}, \tag{13}$$

where W_p and W_n are the widths of the ON and OFF subregions, respectively, and *D* is the distance between peak positions of each subregion. Values ≤ 0 denote separated subregions and values close to 1 mean symmetrically overlapped subregions. These parameters are computed from the raw *x*-*y*-*t* receptive field maps (before Gaussian smoothing) of the PY to bright and dark stimuli, within the time window from 130 to 150 ms. First, we search for the *x*-*y* positions of the peak responses to bright and dark stimuli and the corresponding value of *D*. From the peak responses, moving to the right and to the left in the *x* dimension, the two points whose responses were $1/\sqrt{e}$ of the peak response delimit the values of W_p and W_n.

To characterize the mebrane-potential receptive fields of the different cells, bright and dark spots were flashed only within the center of the ON and OFF subregions of a PY and on the center of a thalamic RC. For every trial we ran a simulation of 300 ms where the spot was ON from 100 to 140 ms. In this case, somatic potentials of the center cell were collected and averaged across 100 trials. A *push-pull index*, as described in [48, 69], was used to determine the relative weight of the antagonistic response to stimuli of opposite contrast:

$$\textit{Push-pull index} = \frac{|P + N|}{\max\left(|P|, |N|\right)}, \tag{14}$$

where *P* and *N* represent synaptic responses to the bright and the dark stimuli, respectively. Synaptic responses are defined as the average membrane potential that was above or below the baseline within a time interval centered near the peak response (also a time window from 130 to 150 ms) [48, 69]. The baseline is computed from the first 100 ms preceding stimulus onset. While the index is 0 for stimuli of opposite contrast that evoke excitatory and inhibitory responses of identical magnitude, the index is 1 for stimuli in which only one contrast generates significant responses.

Numerical implementation. The network model was implemented in Python using Object Oriented Programming [70], which defines a set of classes of objects describing the attributes and methods of the different neuron types and the ganglionar input. Individual cells were created with the Python package LFPy [71] that relies on the NEURON simulator [72] to compute their membrane potentials. Neurons of the network were connected by means of NetCon objects and synaptic connections simulated as discrete events [73]. In addition, we implemented an interface for creating two-dimensional layers of neurons placed in space and connecting them through topology masks. By contrast, the input spike trains from GCs were simulated using NEST 2.8.0 [74, 75] as a Poisson spike generator (*poisson_generator*).

Simulations of the model for the different stimulus sizes were parallelized in the Stallo supercomputer cluster [76] based on the MPI interface [77]. The Stallo cluster has 304 compute nodes that embed Intel Xeon E5 2670/2680 processors of 16 cpu-cores and 32/128 GB memory. We chose an MPI distributed-memory parallelization implemented with the Python library *mpi4py* [78] whereby simulation of every spot size is mapped to one MPI process. Simulation of 1 of the 51 different stimulus conditions within a trial took on average 2.4 minutes. By running 64 processes in parallel, computation of the area-response curves took 4 and 16 hours on average for the flashing spot (100 trials) and the patch grating (400 trials), respectively. We computed 16 area-response curves simultaneously by using up to 1024 processes.

Results

The results are divided into two distinct parts. In the first part results for the feedforward part of the circuit is presented, mainly to validate the model against previous findings in the literature. The studies of the effects of cortical feedback are presented in the second part where the feedforward circuit explored in the first section is used as a starting point.

Network response without cortical feedback

Before studying the effects of cortical feedback on the RC response specifically, we describe the feedforward response of the different cell types in the network model when the cortical feedback is deactivated, i.e., corticothalamic synapses from PYs to dLGN relay cells (RCs) and interneurons (dLGN INs) are disconnected. In this situation the RC response is driven only by excitation from its GC afferents and feedforward inhibition from INs.

Spike receptive fields. The most common way to characterize response properties of cells in the early visual pathway is to measure their spike receptive fields, i.e., the trial-averaged spike response to visual test stimuli [26, 68]. In Fig 4, we show the spatiotemporal dynamics of receptive fields of cells in our network model. Panel A depicts spatial receptive field profiles at two different time intervals: one time interval centered near the peak of the center response (from 130 to 150 ms) and a second time interval centered near the minimum of the rebound decrease in the firing rate (from 200 to 220 ms). Receptive fields of GCs and RCs exhibit the characteristic properties of these cell types: circular receptive fields, with center-surround organization, and their center and surround responses are biphasic in time, consisting of an initial firing-rate increase of the center response followed by a slow rebound firing-rate decrease (the surround has a similar behavior but the respective polarities are reversed). The biphasic structure is further illustrated in the spatiotemporal x-t receptive field profiles (panel B): for t between 130 and 150 ms, the receptive fields of GCs and RCs show a bright-excitatory center, i.e., an increased firing to a bright spot, but for t larger than 200 ms, on the other hand, the polarity of the response of the receptive field center is reversed and it is seen to be dark-excitatory, i.e, increased firing-rate for dark spots.

The receptive field of the cortical cells is formed by a strong ON subregion and a weaker flanking OFF subregion. Both the center and flank subregions show also a biphasic structure in time, a feature that is inherited from the ON and OFF cells providing their afferent inputs. A visual comparison of our model receptive fields in Fig 4 with experimentally measured receptive fields shown in [26] reveals that our RC receptive field qualitatively resembles the experimental receptive field for the 'non-lagged RC' while our cortical-cell receptive field similarly resembles the experimental receptive field for the 'separable simple-cell', i.e., ON and OFF subregions are separable in the space-time domain.

From the spatial receptive field maps of the PY to bright and dark stimuli (before calculating the composite receptive-field profiles shown in Fig 4A), we estimated the widths of the ON and OFF subregions, W_p and W_n, and the distance D between peak positions of each subregion. The position of the peak response to the bright stimulus was situated at (0, 0) degrees and the position of the peak response to the dark stimulus was at (1.25, 0) degrees, providing a distance D of 1.25 degrees. The widths of the ON and OFF subregions were nearly identical ($W_\mathrm{p} = W_\mathrm{n} \simeq 1.3$ degrees), as expected from the symmetrical design of the network. The overlap index was 0.02 (see Eq 13), a value that is within the range of values of cells quantitatively described as simple cells according to their membrane-potential receptive fields [48, 69].

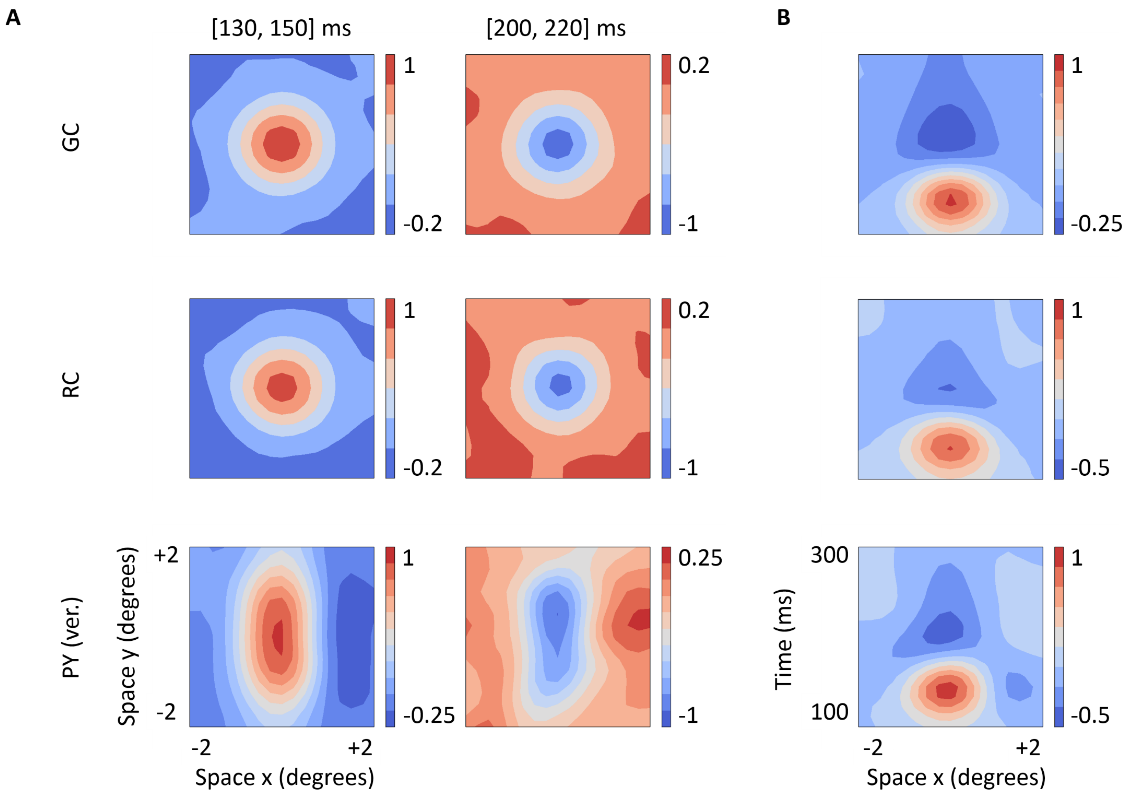

Fig 4. Spatiotemporal structure of spike receptive fields. *x*-*y*-*t* receptive field maps averaged over two different time windows, shortly after stimulus onset and at a later time (panel A), and spatiotemporal *x*-*t* receptive field profiles (panel B) of an ON-center GC, an ON-center RC and an ON-center vertically oriented PY. All cells correspond to the center cell (positioned at the 6th row and 6th column in 10 × 10 grid). Firing rates are normalized to the maximal firing rate. For details about computation of these receptive fields, see Methods.

https://doi.org/10.1371/journal.pcbi.1005930.g004

Membrane-potential receptive fields. To further illustrate the structure of receptive fields and the antagonism between ON and OFF inputs, we show in Fig 5 the membrane-potential receptive fields of RCs and PYs to bright and dark spots, i.e., trial-averaged membrane-potential responses to bright and dark spots [79]. The push-pull effect (in terms of stimulus response) is observed both for the RC and in the different subregions of the PY, that is, stimuli of the reverse contrast evoke responses of the opposite sign. When positioned both in the receptive-field center of the ON-center RC (left panel) and in the ON subregion of the ON-center PY (center panel), a bright spot evoked a strong depolarization followed by a rebound hyperpolarization while a dark spot evoked pronounced hyperpolarization followed by rebound depolarization. The responses when stimulating the OFF subregion of the present cortical cell (right panel), were much weaker. However, as for the stimulation of the ON subregion, a push-pull pattern was observed here as well, although of opposite polarity. We also noted that the trial-averaged membrane-potential traces for the PY in Fig 5 show a higher variance because they integrate synaptic inputs from a larger pool of neurons than RCs do.

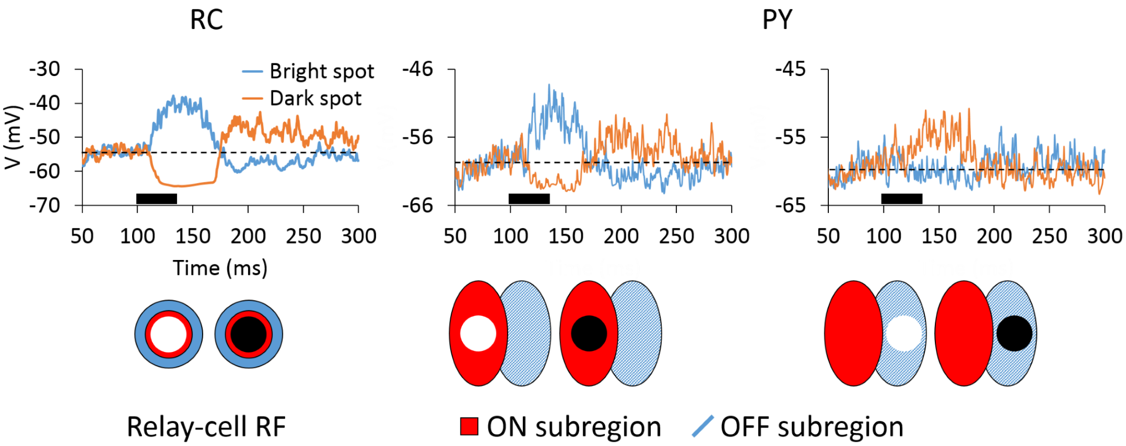

Fig 5. Membrane-potential receptive fields of RCs and PYs to bright and dark stimulation. Averaged somatic membrane potentials over 100 trials to bright or dark spots flashed in the receptive-field center of a RC (left) or within the ON (center) or OFF (right) subregions of a PY cell. Both cells are ON-center cells. Dashed lines indicate baseline computed from the first 100 ms preceding stimulus onset. The thick bar under the traces marks the time the stimulus is on (from 100 to 140 ms).

https://doi.org/10.1371/journal.pcbi.1005930.g005

Further, the presently used test spot is a suboptimal stimuli for PY receptive fields, and thus does not evoke responses as strong as for the RC.

To compare our model responses with experimental results we computed another measure, the push-pull index (see Eq 14), used previously to determine the relative weight of the antagonistic response to stimuli of opposite contrast [69]. For our model, the push-pull index was found to be 0.32 for the RC and 0.68 for the PY. The observation of a larger push-pull index for PYs compared to RCs is in general accordance with the findings of [69] (cf. Fig 4 therein), and a push-pull index of PYs between 0.6 and 0.7 is also seen for some simple cells (though here a large variation is observed in the experiments). While a comprehensive comparison with experiments is prohibited by lack of experimental data, as well as the simplistic description of cortical circuitry, we conclude that the feedforward aspects of our model circuit appear to produce plausible receptive fields.

Temporal response to flashing spots and patch gratings. We next explored the temporal response of the model to flashing spots and patch gratings. Fig 6 shows the trial-averaged post-stimulus time histograms (PSTHs) for cells at the center of the grid stimulated by concentric flashing spots (left column) or patch gratings (right column). For the ON GC response to flashing spots we observe similar overshoot responses to the stimulus onset for the two spot sizes considered, i.e., the 2-degree spot, which essentially covers the receptive-field center, and the 8-degree spot also covering the surround (Fig 6A).

However, the surround-inhibition evoked by the 8-degree spot substantially reduced the response after stimulus onset, resulting in a more pronounced exponential-like decay of the ON GC as observed experimentally [27]. The response of the OFF GC is suppressed for the entire time the flashing spot is on for the 2-degree spot, while for the 8-degree spot some firing is seen after approximately 200 ms.

The RC response is qualitatively similar to the response of the ON GC but the overall firing rate is lower in accordance with the lower retinogeniculate transfer ratio of the firing rate reported in [27]. The overshoot responses of the IN and PYs to the flashing spot were more

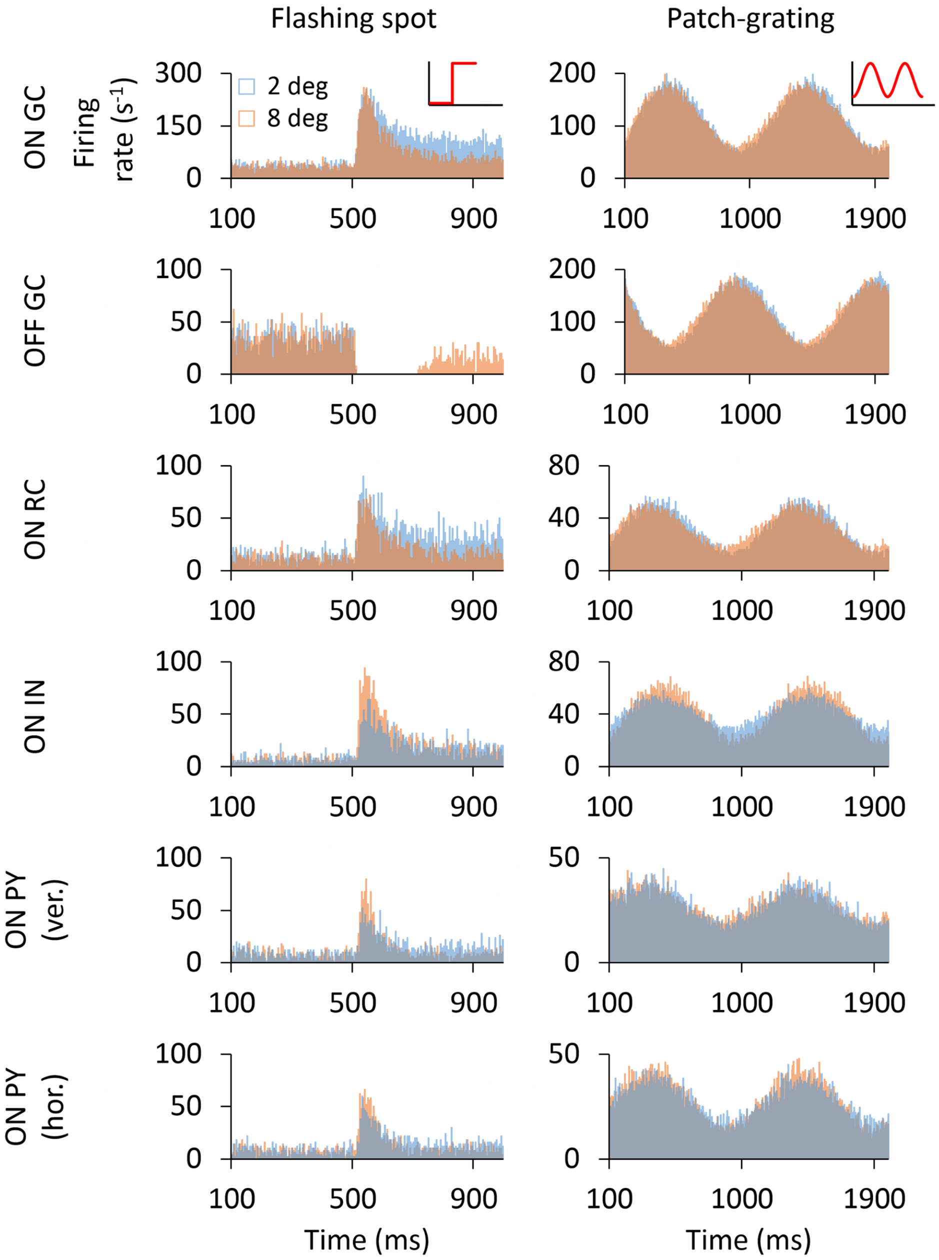

Fig 6. PSTHs of cells for the flashing spot and patch grating. Trial-averaged PSTHs of ON- and OFF-center GCs, ON-center RC, ON-center IN and ON-center vertically and horizontally oriented PYs for two spot/patch diameters: 2 and 8 degrees. All cells correspond to the center cells (6th row, 6th column) in the two-dimensional grids. The 8-degree responses of the IN and PYs are plotted in the front of graph for better visualization.

https://doi.org/10.1371/journal.pcbi.1005930.g006

pronounced for a 8-degree spot because this stimulus size better stimulates their receptive fields during the transient response. As for the GC response, the RC response reached a steady state after an exponential-like decay.

Inspection of the patch-grating responses in the right column of Fig 6 reveals that the response, i.e., amplitude modulation, to the 2-degree patch is slightly larger than the response to the 8-degree patch for both the ON and OFF GCs, as well as the ON RC. More noticeable differences were observed between responses to 2-degree and 8-degree patches when choosing smaller values of the spatial frequency ν_{pg} of the patch grating (see Eq 9). However, the spatial frequency selected in this work evokes smaller surround suppression in the GC response and thus facilitates the study of cortical-feedback induced effects of the increase in the surround suppression in RCs. Another noteworthy feature of both the GC and RC responses are that the 2-degree response is seen to be slightly phase-delayed compared to the 8-degree response.

For the ON IN the patch-grating results are similar to that observed with the flashing spot: there is a significant increase of the firing rate for the largest patch diameter. However, unlike for GCs and RCs, the 8-degree response is seen to be slightly phase-delayed compared to the 2-degree response. This reflects the spatial arrangement of synaptic inputs from GCs to the IN.

For PYs, an interesting difference is seen between responses of the horizontally-selective and vertically-selective cells. While the 8-degree response was substantially larger than the 2-degree response when the stripe orientation matched the orientation selectivity (horizontally-selective PY), this difference was barely noticeable when they were non-matched (vertically-selective cells PY).

Two-dimensional spatial representation of the network response. The spatial profile of the network response is depicted in Fig 7 for the various cell types in the model. Here each

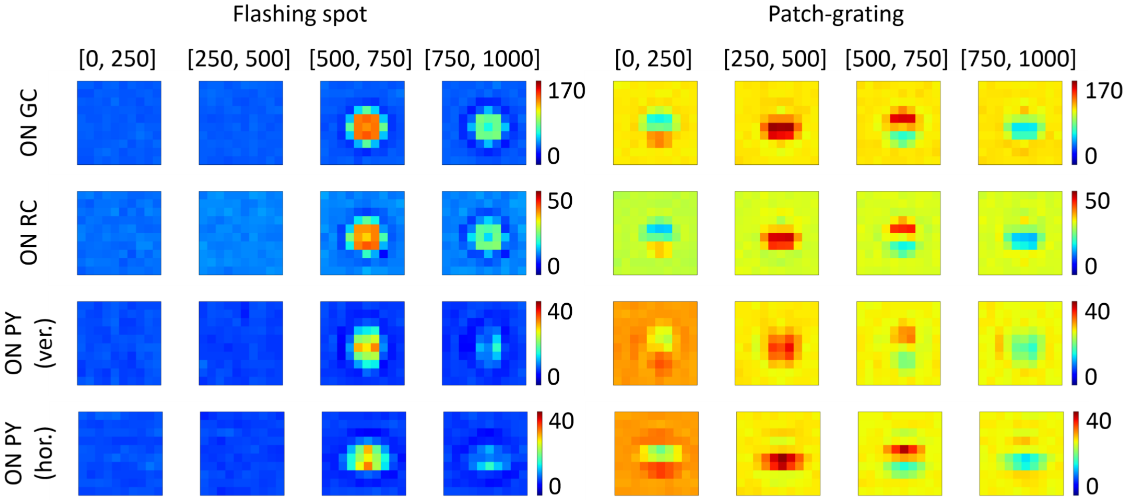

Fig 7. Time-averaged topographic representation of responses of cells in the network grids. Two-dimensional representations of time-averaged PSTHs of ON-center GCs, RCs and horizontally- and vertically-selective PYs. Four leftmost columns: Averaged PSTHs for the flashing-spot stimulus at four different time windows as indicated (in ms). Four rightmost columns: Averaged PSTHs for the patch-grating stimulus at the same time windows. A pixel in every panel represents time-averaged activity of one cell in the corresponding 10 × 10 grid. Color bars include values of the time-averaged firing rates. The stimuli are centered on the cell at the 6th row and 6th column of the 10 × 10 grid, and the stimulus diameter is 4 degrees.

https://doi.org/10.1371/journal.pcbi.1005930.g007

color panel shows a topographic representation that includes the activity of every cell in the corresponding 10 × 10 grid, averaged across four different time intervals.

The four leftmost columns of plots show flashing-spot responses. Following the spot onset at 500 ms, the response of GCs and RCs covering the spot area reproduce the overshoot response seen in experiments [25, 27, 80], reflected in an increase of the activity that progressively diminishes and reaches a steady state for the last time interval (from 750 to 1000 ms). In the response of GCs and RCs after spot onset, we can observe the clear effects of the center-surround antagonism of their receptive fields. Thus, cells at the edge of the spot, whose receptive-field center is covered by the stimulus while a significant portion of the receptive-field surround is not, show a larger response than cells situated in the stimulus center. The response drops below the background firing for those cells whose receptive field lies just beyond the edge of the spot, producing a dark annulus of reduced activity surrounding the stimulating spot. The spatial pattern of the flashing-spot response for the RCs is qualitatively similar to that of the GCs, but the firing rates are generally smaller (similar to what was seen in the PSTHs depicted in Fig 6). The spatial profile of the flashing-spot responses of the PYs resembled those of RCs, but the orientation selectivity of the PYs has some notable effects: the horizontally selective population enhances horizontal edges of the spot stimulus while the vertically selective population enhances vertical edges (see, for example, activity of the four cells flanking the cell situated in the center of the grating).

The four rightmost columns of plots in Fig 7 show the responses to a patch grating for one complete oscillatory cycle. The circular patch contains a horizontal-striped sine wave grating moving upward. For this stimulus one expects the horizontally selective cortical neurons (PY hor.) to respond more vigorously than the vertically selective population (PY ver.). This is also what is observed: compare, for example, responses of the center cells of the horizontally-selective and the vertically-selective populations for the period between 250 and 500 ms.

Area-response curves. The measurement of the so-called area-response curves has been a common way to quantify the spatial response properties of cells in the early visual pathway, in particular for LGN RCs [4, 18, 19, 27, 81]. Here the response to circular spots (patches) centered on the receptive-field center is measured as a function of the spot (patch) diameter. Of particular interest for the present study is the area-response curves measured for LGN RCs since the main focus is on the role of cortical feedback on the RC response. Interestingly, the measured RC area-response curves have been observed in experiments to depend on whether cortical feedback is present or not [4]. A key goal of the present modeling study is to investigate possible mechanisms for these observed differences. Most of the following results are thus focused on such area-response curves, in particular on specific features of these curves such as the stimulus diameter giving the maximum response (corresponding to the receptive-field center size in the case of flashing spots) and the center-surround antagonism coefficient α defined in Eq 12.

Fig 8 shows area-response curves for the different types of cells in our model circuit. Panel A (left column) shows results for GCs, both ON and OFF cells, when bright flashing spots are used as stimuli. For the ON cell, the area-response curve reaches a maximum for a spot diameter of about 2 degrees, corresponding to the size of the receptive-field center [27, 28]. For this diameter the stimulus spot fits the excitatory center exactly. For larger spots the stimulus also covers part of the inhibitory surround, and the response is correspondingly reduced. When the spot diameter increases beyond also the surround, the response no longer changes with diameter, i.e., the area-response curve reaches a plateau level. For the OFF GC, the area-response curve has instead a dip for spot sizes similar to the receptive-field center but the response recovers when the spot diameter is increased to cover also part of the now excitatory surround.

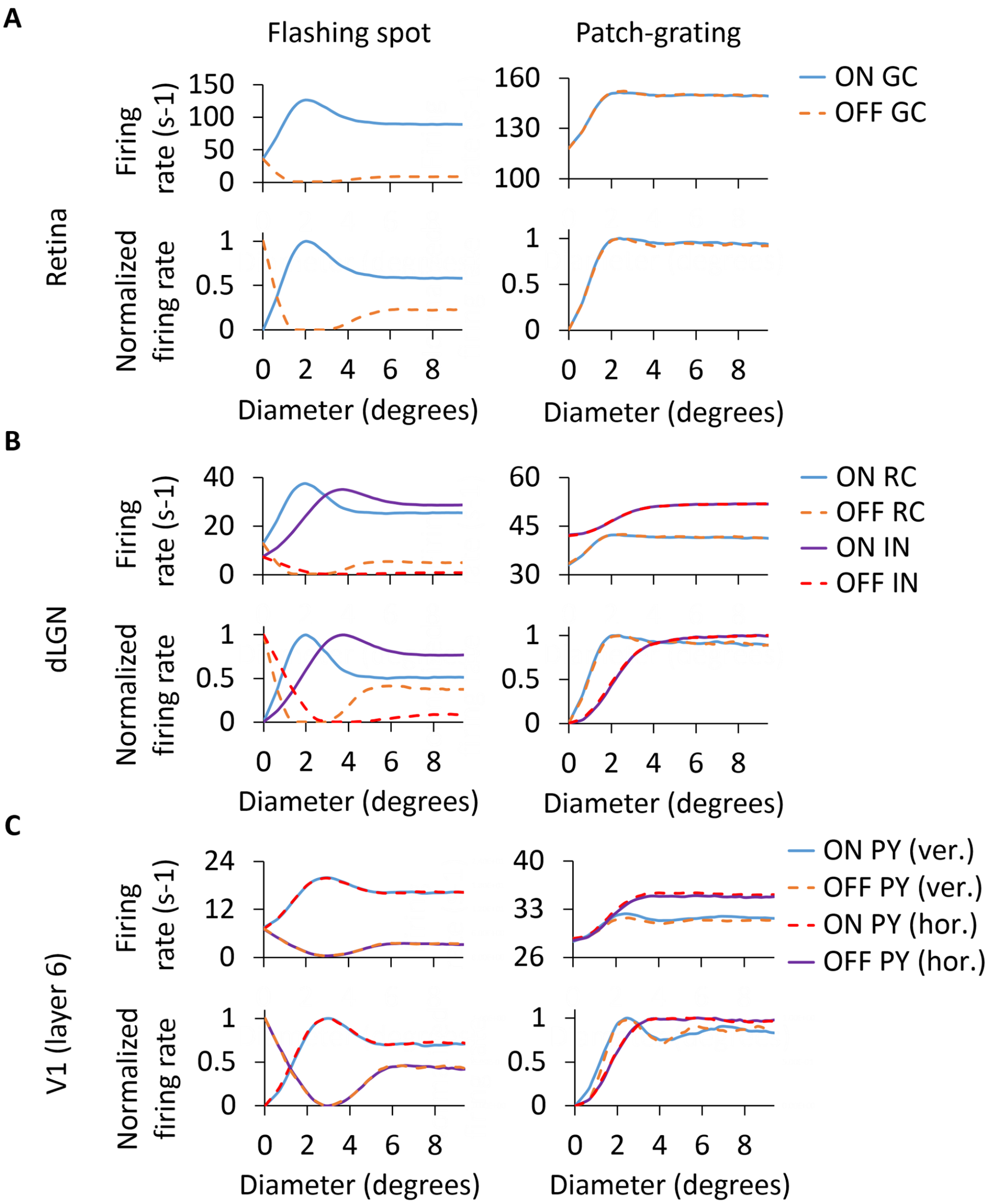

Fig 8. Area-response curves of cells in the model circuit including only feedforward connections. Area-response curves of GCs (A), RCs and INs (B) and PYs with horizontal and vertical orientation-selectivity (C) for the flashing spot and patch grating. For the flashing spot, each data point of the area-response curve represents the mean firing rate computed during the second 500 ms period of the simulation. For the patch grating, each data point corresponds to the mean firing rate of the rectified response over one full cycle (see Methods for further details). ON and OFF responses for the patch grating are 180 degrees out of phase.

https://doi.org/10.1371/journal.pcbi.1005930.g008

Table 4. Response measures for GC and RC for example area-response curves for flashing spots and patch gratings. d_c is the spot size giving the largest response (and corresponds to the receptive-field center size for flashing spots). The center-surround antagonism α is defined in Eq 12. Results from upper two rows are extracted from Fig 8. Results from the third, fourth and fifth rows are extracted from Figs 10 and 14, respectively.

	Flashing spot		**Patch grating**	
	d_c (deg)	**α (%)**	**d_c (deg)**	**α (%)**
GC	2.0	41.8	2.4	6.6
RC (without feedback)	2.0	50.1	2.4	11.2
RC (phase-reversed feedback)	1.8	61.6	2.0	26.0
RC (phase-matched feedback, Fig 14A)	2.0	49.1	2.4	11.3
RC (phase-matched feedback, Fig 14B)	2.0	54.6	2.0	18.3

https://doi.org/10.1371/journal.pcbi.1005930.t004

In Fig 8B (left column), area-response curves for dLGN cells are depicted for the flashing-spot stimulus. While the magnitude of the firing rate is much reduced, the RC area-response curve qualitatively resembles that of the ON GC (panel A) that provides the feedforward excitatory input. The patch size giving the maximum response is, for example, very close to that of its retinal afferent, i.e., about 2 degrees. However, we observe a larger center-surround antagonism for the RC compared to the GC that feeds into it, i.e., the center-surround antagonism coefficient α is increased from 41.8% to 50.1% (see Table 4). As there are only feedforward connections in this configuration of the dLGN model circuit, the larger center-surround antagonism of the RC compared to the GC is due the feedforward inhibition via INs [41].

The flashing-spot area-response curves of INs in Fig 8B are distinguished from the RC curves by the much larger receptive-field center diameter, i.e., about 4 degrees rather than 2 degrees. This reflects the spatially more widespread feedforward input from four neighboring GCs. We also observe a much reduced center-surround antagonism compared to RCs, in accordance with previous experimental [82] and modeling studies [28, 41]. The flashing-spot curves for the PY in panel C exhibit similar qualitative features of the INs: larger receptive-field center sizes (about 3 degrees) and smaller center-surround antagonism than for the RC. We also observe essentially identical area-response curves for the horizontally and vertically-selective PYs, reflecting the circular symmetry of the flashing-spot stimulus.

Panels in the right column of Fig 8 show the area-response curves for patch gratings. For the ON-center GC response (panel A), the shape of the curve follows the same tendency as shown for the flashing spot, in which the maximal response is seen at about 2 degrees and the response is reduced for larger diameters. However, this reduction of the response is less pronounced for the patch-grating stimulus as observed experimentally in decorticate conditions where only feedforward inputs are present like here [4].

Note, also, that the shape of the patch-grating curve depends on the chosen value of the spatial frequency ν_{pg} of the grating. With a lower spatial frequency than the one used here (0.15 cycles/deg; cf. Table 1), i.e., thicker grating stripes, the area-response curves would be more similar to the flashing-spot curves. The patch-grating curves for the RC in panel B also show a maximum at around 2 degrees and the center-surround antagonism α is increased compared to the GC curve, from 6.6% to 11.2% (see Table 4). It should be noted that the patch-grating response of OFF-center cells is 180 degrees out of phase compared to the response of ON-center cells.

The IN area-response curve for the patch grating does not exhibit a clear maximum, but is instead monotonously increasing even for patch diameters beyond the IN receptive-field center size of about 4 degrees. The patch-grating area-response curves of the PYs are shown in Fig 8C. Unlike for the flashing-spot stimulus, the response to the grating is different for the horizontally-oriented and vertically-oriented PYs when the diameter of the patch is greater than 2 degrees. While the receptive field of the horizontally-oriented PY perfectly matches the horizontal stripes of the stimulus, the receptive field of the vertically-oriented PY is perpendicular to the grating stripes, resulting in a lower firing rate as shown for the area-response curves in panel C.

Effects of cortical feedback on the RC response

After exploring above the feedforward response of the different cell types in the network model, we now move on to investigate how cortical feedback to the dLGN circuit affects the spatial response properties of RC cells. This will depend on the detailed corticothalamic connectivity pattern which is not yet experimentally fully resolved. In the next sections, we thus present simulation results for the different alternatives considered in Fig 3.

Functional organization schemes of the feedback signal. One key aspect of the feedback signal is its spatial organization, i.e., whether each PY only feeds back to a single RC (1 × 1 configuration) or whether each PY feeds back to a cluster of four neighboring RCs (2 × 2 configuration), see Fig 3C. For the 1 × 1 case a qualitative account of the effect of the corticothalamic feedback on the RC area-response curves is obtained from the PY curves in Fig 8C, while for the 2 × 2 feedback the aggregate activity of the four PYs connected to a RC is more relevant. In Fig 9 we show this aggregate response computed by averaging the area-response curves of the four PYs in every cortical population that connect to the same RC: ON and OFF vertically-oriented, and ON and OFF horizontally-oriented. Comparison of the area-response curves for single PYs in Fig 8C, and the corresponding curves for the aggregate PY responses in Fig 9 reveals similar characteristics. As expected, the area-response curves for aggregate feedback is independent of orientation selectivity for flashing spots, both for ON and OFF cells, but not for the patch grating.

For the flashing-spot curves a difference between the aggregate area-response curves in Fig 9 and the area-response curves for single PYs in Fig 8 is that the maximum occurs for a larger

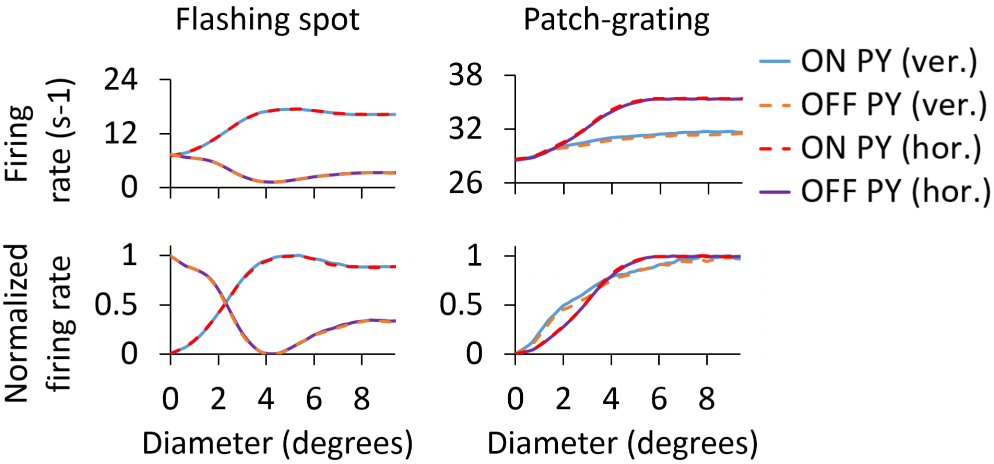

Fig 9. Aggregate corticothalamic signals from ON- and OFF-center PYs. ON PY (hor.) and ON PY (ver.) are the aggregate area-response curves of the 4 horizontally oriented and the 4 vertically oriented ON-center PYs, respectively, that feedback to one RC (and one dendrite of the IN) in the 2 × 2 configuration of Fig 3C. The same notation is used for the OFF-center cells.

https://doi.org/10.1371/journal.pcbi.1005930.g009

spot diameter for the aggregate. Likewise, for the patch-grating curves, the plateau level is reached for a larger patch size for the aggregate. As shown below, these differences between the feedback curves from single PYs and 2 × 2 PYs for large stimulus diameters are key for understanding how the different spatial feedback configurations affect the RC response.

Another key aspect of the cortical feedback is the functional organization of synapses between ON and OFF PYs and their target ON and OFF RCs. We consider two different configurations: (i) ON PYs excite both ON RCs and ON INs (*phase-matched feedback*, Fig 3A) and (ii) OFF PYs excite ON RCs (*phase-reversed feedback*, Fig 3B). The latter arrangement implies that there is a phase-reversed *push-pull* influence from layer 6 simple cells providing feedback to the LGN, a set-up that has received support both in experimental [62] and modeling studies [40]. In analogy, the phase-matched arrangement can be also called *push-push* feedback [48, 69].

Phase-reversed (push-pull) cortical feedback. Corticothalamic feedback has been observed to exert both excitatory and inhibitory influences on RCs [1, 2, 4, 83]. By itself, direct excitatory feedback to RCs will generally increase the RC firing rate, while indirect inhibitory feedback via INs will reduce the firing rate. In the present model study we are particularly interested in regimes with a rough balance between excitatory and inhibitory effects so that the main effect of cortical feedback is the change in the *shapes* of the area-response curves, not their overall magnitude. Further, the model set-up and parameters values are chosen so that the IN firing rate is only modestly altered [64], i.e., all inhibitory effects from cortical feedback are mediated via triadic action from INs to RCs with little effect on IN firing. This is in accordance with the idea that the corticothalamic pathway is primarily modulatory rather than driving in nature [5]. Although we focus on ON-center RCs, a similar behavior is found for OFF-center RCs.

Area-response curves: In Fig 10 we compare the RC responses with and without cortical feedback (absolute firing rates on top, normalized firing rates below). Firstly, we describe the

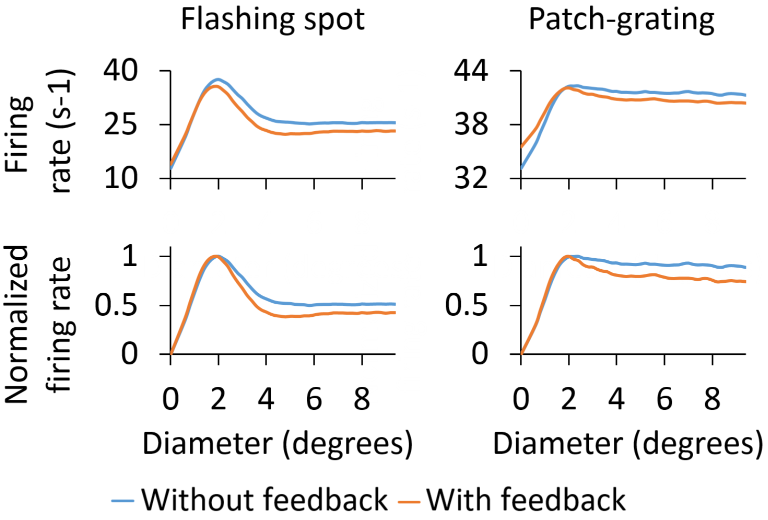

Fig 10. Area-response curves for ON-center RC with and without cortical feedback for the phase-reversed configuration. The RC receives feedback from a set of 2 × 2 PYs. The synaptic weight of the monosynaptic connection between PYs and RCs is set to 1.5 nS and to 0.3 nS between PYs and INs. Other parameters are listed in Tables 1–3.

https://doi.org/10.1371/journal.pcbi.1005930.g010

inhibitory effects of cortical feedback on the RC response. As observed for both stimuli, the major effect is that cortical feedback increases surround suppression on RCs, which results in a reduction of the response for stimulus diameters larger than 2 degrees. The center-surround antagonism α is increased compared to the RC curve without feedback, from 50.1% to 61.6% for the flashing spot and from 11.2% to 26.0% for the patch grating (see Table 4).

The additional surround suppression is seen to have the signature of the aggregate response of ON-center PYs (shown in Fig 9) that feed back to the IN. Indeed, the flashing-spot response in Fig 10 has a dip for a spot size similar to the maximum of the ON-center aggregate response in Fig 9 (at about 5 degrees). Likewise, the continuous decrease of the patch-grating response with increasing patch sizes is seen to match the corresponding increase in the patch-grating aggregate response. In addition, the effectively reduced excitatory feedback from OFF-center PYs (since this feedback is out of phase with the ON-center RC) for large spot sizes (Fig 9) may also contribute to the increased center-surround antagonism.

The increase of surround suppression has been observed in experiments with both flashing spots [32] and patch gratings [4, 19], although the effect seems to be less prominent with flashing spots [2, 4]. Our example results in Fig 10 also show a larger increase of surround suppression for the patch-grating stimulus, but not as prominent as the increase reported in [4].

As seen below where the dependency of model behavior on the corticothalamic synapse weights are systematically explored, the amount of suppression and center-surround antagonism vary with model parameters. However, a general trend is that cortical feedback appears more effective in increasing surround suppression for patch gratings than for flashing spots.

Unlike for the flashing spot, cortical feedback also amplifies the patch-grating response for the smallest patches, i.e., for diameters smaller than the diameter of the receptive-field center (upper right panel in Fig 10). Thus, in this stimulus range, the competition between excitatory feedback from OFF PYs and inhibitory feedback from ON PYs results in a net excitation. This model prediction is in accordance with experimental observations of patch-grating responses on primate LGN RCs [18].

The third effect produced by cortical feedback is the reduction of the stimulus diameter giving the maximum response. For the example results in Fig 10, close inspection reveals that the size of this maximum-response diameter is slightly reduced from 2.0 degrees without feedback to 1.8 degrees with feedback for the flashing spot (where this maximum-response diameter corresponds to the receptive-field center size [27]). For the patch grating the maximum-response diameter is reduced from 2.4 to 2.0 degrees by the cortical feedback (Table 4).

Membrane potentials: We next turn to an exploration of the mechanisms behind the effects observed for cortical feedback in the phase-reversed situation in Fig 10. In Fig 11 we show excerpts of membrane potentials for various cells in the model circuit with patch-grating stimulation. Two different patch diameters are considered, 1.8 degrees and 8 degrees. We note that, as the RC voltage dynamics is dominated by the driving input from retina, it was close to identical in the cases without (black lines) and with (red lines) cortical feedback included. However, exceptions to this occurred when the membrane potential was close to the action-potential threshold. At such instances, cortical input could either act to push (otherwise) subthreshold events in RCs above the threshold by providing direct excitation, or to prohibit threshold crossings (that would otherwise occur) by providing indirect inhibition of RCs via INs. Thus, the cortical feedback on RC responses is to either add or remove spikes, in accordance with previous experimental observations [34].

In the case of the small spot (1.8 degrees) the excitatory component of the cortical feedback dominated. Cortical feedback then acted to push occasional subthreshold events above the threshold, and lead to extra action potentials being fired by RCs (blue arrows in Fig 11). This

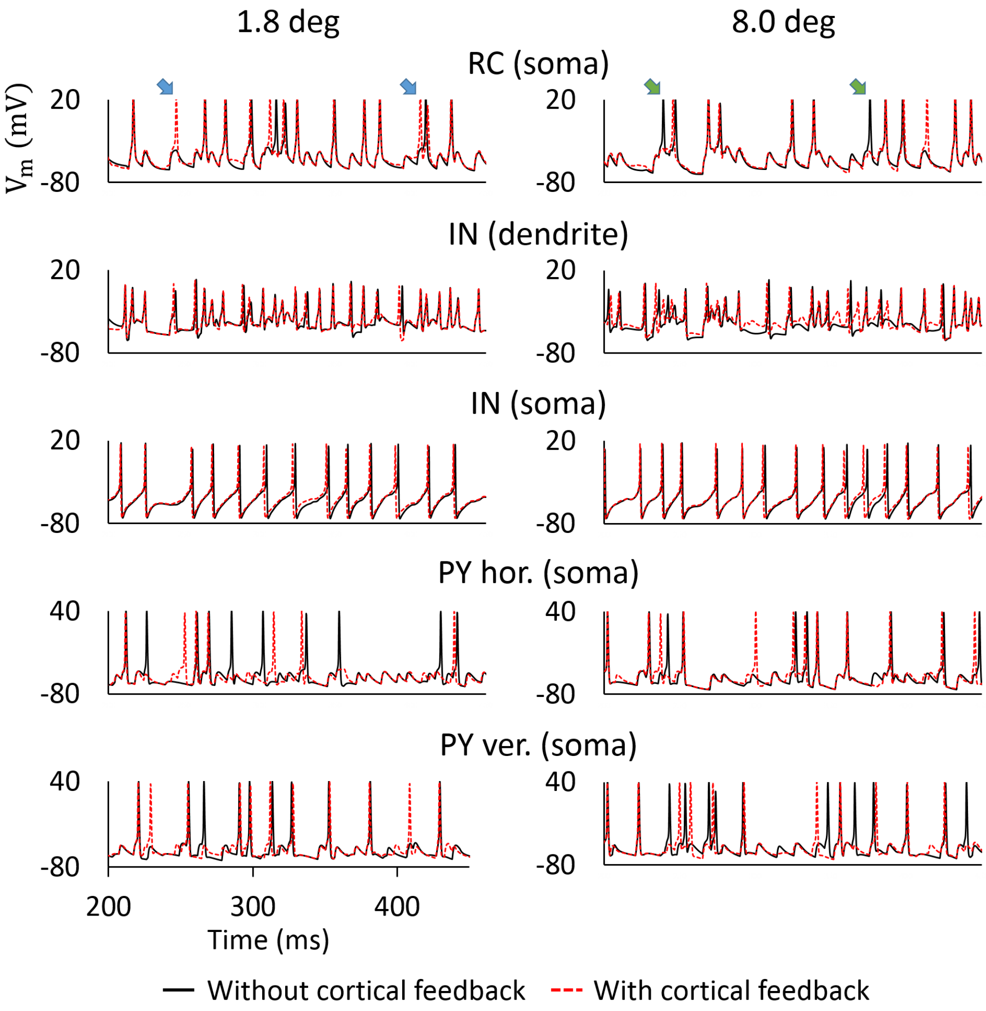

Fig 11. Membrane-potential dynamics for the patch grating at different stimulus sizes with the phase-reversed feedback. Somatic records correspond to ON cells situated at the center of their corresponding layers. The LGN IN dendrite depicted is the dendrite connected with the RC. Blue and green arrows indicate extra action potentials and suppression of action potentials elicited by cortical feedback, respectively. Corticothalamic synapse weights are the same as in Fig 10.

https://doi.org/10.1371/journal.pcbi.1005930.g011

explains the observation in Fig 10 that cortical feedback increased the response for patch sizes smaller than 2 degrees.

With a larger spot (8 degrees), a larger number of PY cells were activated, the spatially extended INs thus received more cortical feedback (cf., Fig 3C). Then, the inhibitory component of cortical feedback became more pronounced. The inhibitory mechanisms are complex, as INs provide inhibition both via dendodendritic and axonal GABA-release. A close investigation of Fig 11 indicates that cortical feedback predominantly acted on INs by modulating the timing (i.e., the spikes occurred earlier), rather than the amount (i.e., the number of spikes was

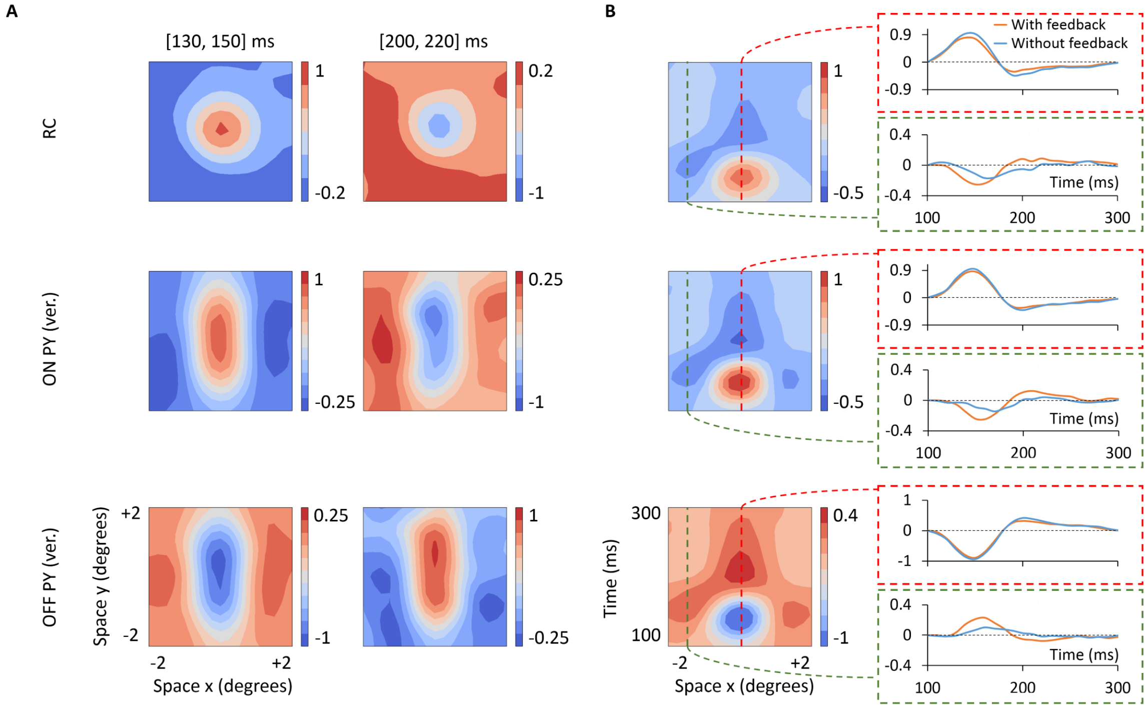

Fig 12. Spike receptive fields with phase-reversed cortical feedback. *x*-*y*-*t* receptive field maps averaged over two different time windows (panel A) and spatiotemporal *x*-*t* receptive field profiles (panel B) of an ON-center RC and two vertically oriented PYs of the ON and OFF-center type, respectively. The additional column on the right of panel B shows 1D temporal profiles extracted from two locations of the *x*-*t* receptive field (see Methods), one corresponding to the receptive-field center, the other two the receptive-field surround. Firing rates are normalized by the same values used in Fig 4. Corticothalamic synapse weights are the same as in Fig 10.

https://doi.org/10.1371/journal.pcbi.1005930.g012

the same) of inhibitory output. Since RCs and INs receive joint retinal input, the timing is important, and especially so in the triadic synapses, where excitation and inhibition of RCs tend to follow with a time-locked delay [84]. As Fig 11 indicates, an earlier occurrence of inhibitory output from INs tended to prevent threshold crossings in RCs (green arrows), while the opposite occurred more rarely. Therefore, cortical feedback leads to a reduced RC firing rate. This explains the observation in Fig 10 that cortical feedback increased surround suppression for large patches.

Receptive fields: We next examined effects of the phase-reversed feedback on properties of the spike receptive fields. Spatial *x*-*y*-*t* receptive-field representations and spatiotemporal *x*-*t* receptive field profiles, analogous to Fig 4 for the case without cortical feedback, are shown in Fig 12. Overall, the receptive field of the depicted ON-center RC (panel A) maintains the same spatial structure as seen for the feedforward situation in Fig 4: roughly circular receptive fields with center and surrounds both responding biphasically in time. The most striking differences between the configurations with and without feedback arise in the relative amplitudes of the center and surround responses. To better illustrate this, we have added a column on the right in panel B showing the time evolution of the center and surround responses. As seen here, cortical feedback reduces the RC center response and increases the RC surround response (in terms of the absolute value of deviation from the background firing activity).

These changes in the center response of RCs can be explained by considering the time plots of center responses of ON-center and OFF-center PYs (center and bottom right panels of Fig 12). The center response of ON PYs increases its firing rate immediately after stimulus onset, which implies increased disynaptic inhibition (mediated by LGN interneurons) and thus a reduced RC firing rate in the first part of the biphasic response.

OFF-center PYs, which give excitatory input to RCs in this phase-reversed configuration, instead decrease their firing rate in the first phase of a center-stimulus response. This further contributes to the reduced RC response to a center stimulus in the first phase of the biphasic response. For the second phase the situation is opposite. Here the OFF-center PYs increase their firing rate with a center-stimulus response, further contributing to the increased response of the RC in the second phase.

The effect of cortical feedback on the RC surround response is seen to not only quantitatively change the amplitude of the response: here the feedback is seen to provide a substantial dip in the RC firing rate for the first part of the response (up until about 180 ms, cf. second panel in the right row of Fig 12). Note that this effect cannot be accounted for by the surround responses of ON and OFF PYs shown in Fig 4 as this would give the oppositely directed change in the RC firing rate for surround stimulation. Instead the observed response changes must mainly stem from center responses of laterally shifted PYs, i.e., with their receptive-field centers positioned in the surround of the RC cell. Note that in the present model example each RC receives feedback from a set of 2 × 2 PYs (each with elongated receptive-field centers as seen in panel A).

Poststimulus time histograms (PSTHs): We finally explored the effect of phase-reversed cortical feedback on PSTHs, both for flashing-spot and patch-grating responses. Fig 13 shows results for two spot/patch diameters: the smallest (2 degree diameter) essentially covering the receptive-field center, the largest (8 degree diameter) covering a large part of the surround. A detailed comparison of the cases with and without cortical feedback is difficult just by visual inspection. However, the key point is that the amplitude of the sinusoidal rate modulation is reduced with cortical feedback for large patch gratings (cf. Fig 10), which is clearly discernible. We also observe that the patch-grating response for the case with cortical feedback is phase-advanced compared to no-feedback case, in accordance with previous observations of the effect of inhibition-dominated feedback on the drifting-grating response transfer function [85].

Phase-matched (push-push) cortical feedback. *Area-response curves:* In the phase-matched configuration, both ON RCs and ON INs receive feedback from ON PYs (Fig 3A). Fig 14A shows the area-response results obtained for the same set of parameters used for the phase-reversed situation depicted in Fig 10. These parameter values roughly balance the excitatory and inhibitory feedback effects to RCs. Since these two effects have similar size but have opposite signs, the net effect on the RC for phase-matched feedback is as expected practically negligible both for flashing spots and patch gratings. As a consequence, the center-surround antagonism α is now essentially unaffected by the feedback.

We find that in order for cortical feedback to increase surround suppression in the RC response in this phase-matched configuration, the inhibitory contribution to the feedback must be larger than the excitatory contribution. To illustrate this point we show in Fig 14B area-response curves for the case when the excitatory feedback is turned off, i.e., the synaptic weight between PYs and RCs is set to zero. In this situation the cortical feedback again increases surround suppression on RCs, i.e., α is increased compared to the RC curve without feedback, from 50.1% to 54.6% for the flashing spot and from 11.2% to 18.3% for the patch

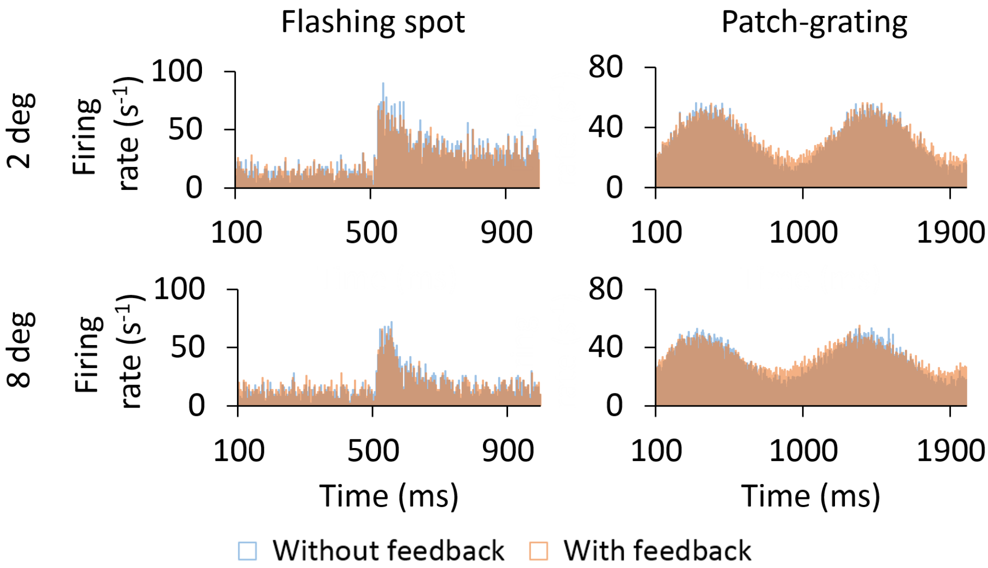

Fig 13. PSTHs of RCs for flashing spots and patch gratings with phase-reversed feedback and without feedback. Trial-averaged PSTHs of ON-center RC for two spot/patch diameters: 2 and 8 degrees. PSTHs for the phase-reversed feedback are compared with PSTHs shown in Fig 6. Corticothalamic synapse weights for the feedback configuration are the same as in Fig 10.

https://doi.org/10.1371/journal.pcbi.1005930.g013

grating (see Table 4). However, the surround suppression is still smaller than for the phase-reversed feedback (Fig 14) where the excitatory feedback from OFF PYs adds to center-surround suppression, not subtracts from it as for feedback from ON PYs in the phase-matched situation.

Spike receptive fields: The spike receptive-field plots in Fig 15 further illustrate this point. For the case with phase-matched feedback effects of the cortical feedback are almost absent both for the center and the surround responses (panel B). With only inhibitory feedback present, the center response is reduced as for the phase-reversed situation in Fig 12. However, the extent of the reduction is smaller.

Influence of corticothalamic synapse weights and spatial connectivity profile of cortical feedback. In the following, we further investigate the behavior of the network model by exploring the dependence of the area-response curves on the model parameters describing the cortical feedback. We systematically varied weights of synapses between cortical PYs and RCs and INs. Simulations were done for both feedback arborization configurations, 1 × 1 and 2 × 2, and also for the different phase arrangements between receptive fields of PYs and dLGN neurons, phase-reversed (Figs 16 and 17) and phase-matched (Figs 18 and 19).

In Fig 16, we show the different RC responses to the flashing spot for the phase-reversed case. As expected the overall firing rates of RCs are increased when increasing the feedback weight values for RCs (moving down) and are reduced when increasing the values for INs (moving right). This is seen for both spatial kernels, 1 × 1 and 2 × 2. However, the 2 × 2 feedback configuration is seen to increase surround suppression more than 1 × 1.

The upper row of panels corresponds to the case where there is no feedback excitation from PYs to RCs and clearly illustrates how inhibitory feedback increases the surround suppression of RCs. The first column of panels instead shows the case where feedback inhibition is turned

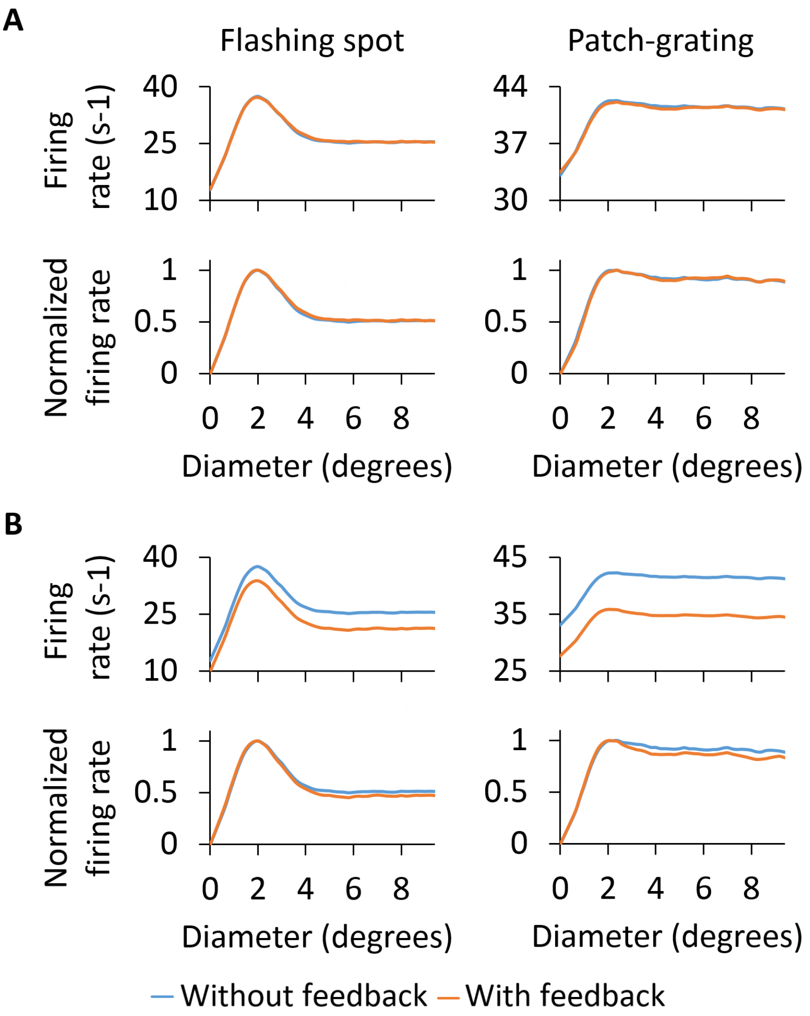

Fig 14. Area-response curves for ON-center RC with and without feedback for phase-matched and inhibitory-only feedback. A: phase-matched: synaptic weight between PYs and RCs set to 1.5 nS, between PYs and INs to 0.3 nS. B: inhibitory-only: synaptic weight between PYs and RCs set to zero, between PYs and INs to 0.3 nS The RC receives feedback from a region of 2 × 2 PYs.

https://doi.org/10.1371/journal.pcbi.1005930.g014

off, and there is only feedback excitation. Here it is seen that very large values of the excitatory connection from PYs to RCs (cf. row 4) can even result in an opposite effect, i.e., a reduced surround suppression. However, the combined effect of feedback excitation and inhibition enables a larger increase of the surround suppression compared to the case with only feedback inhibition as exemplified by the lower right panel (row 4, column 4) in Fig 16.

In general terms, a similar behavior is observed for the responses to the patch grating with phase-reversed feedback (Fig 17): there are larger firing rates when increasing the excitatory

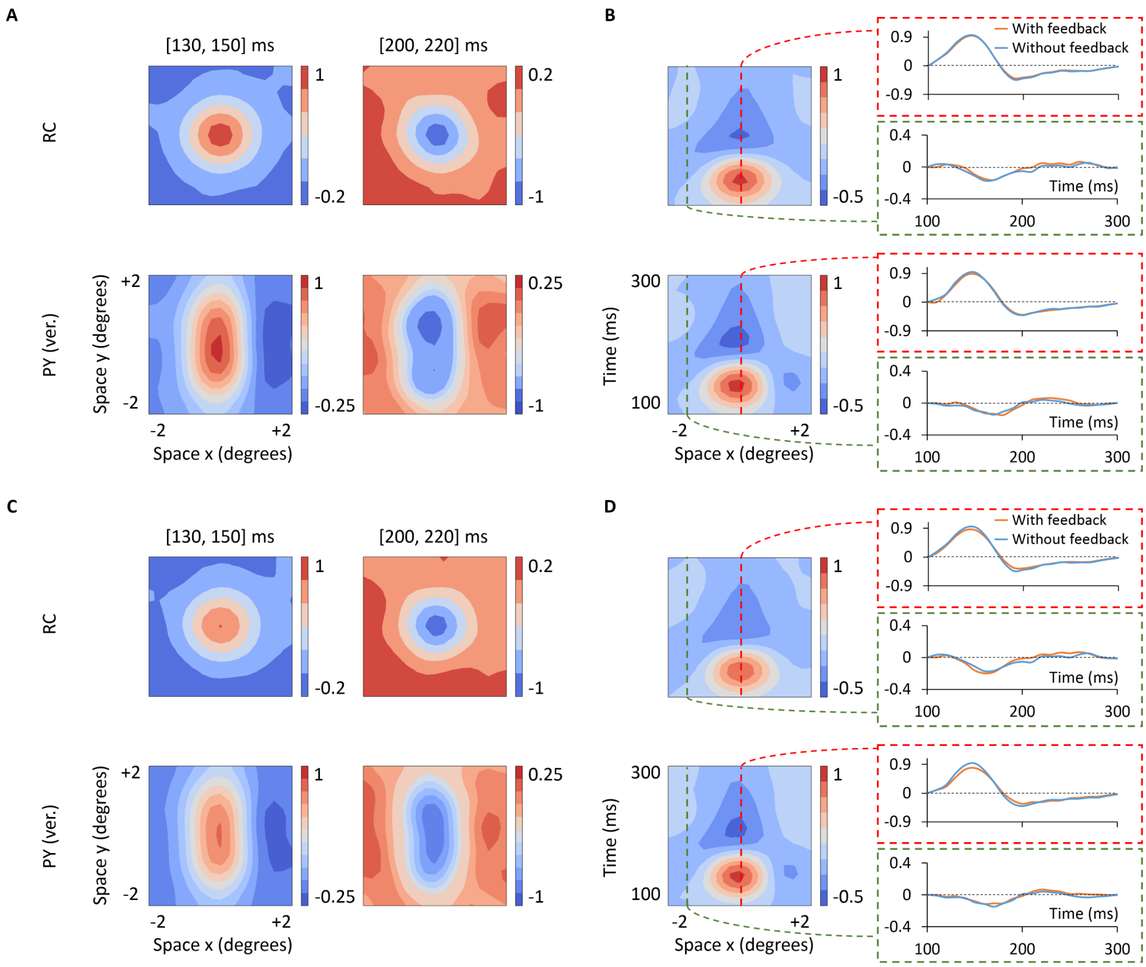

Fig 15. Spike receptive fields for RC and PY for phase-matched and inhibitory-only feedback. A–B: phase-matched: synaptic weight between PYs and RCs set to 1.5 nS, between PYs and INs to 0.3 nS. C–D: inhibitory-only: synaptic weight between PYs and RCs set to zero, between PYs and INs to 0.3 nS. The RC receives feedback from a region of 2 × 2 PYs. *x*-*y*-*t* receptive-field maps of ON-center RC and ON-center vertically oriented PY are shown in A and C. Their corresponding spatiotemporal *x*-*t* receptive-field profiles are shown in B and D. Additional column on the right of panels B and D shows 1D temporal profiles extracted from two locations of the *x*-*t* receptive field corresponding to the receptive-field center (ON subregion) and receptive-field surround (OFF subregion). Firing rates are normalized by the same values used in Fig 4.

https://doi.org/10.1371/journal.pcbi.1005930.g015

connection and a marked reduction of firing rates for the greatest values of the IN synaptic conductance. Also here the combined effect of excitation and inhibition from cortical feedback produces the largest increase in surround suppression of RCs.

RC responses with the phase-matched configuration are shown for the flashing spot in Fig 18 and for the patch grating in Fig 19. Here the area-response curves with feedback largely maintain the same shape of the area-response curves without feedback since both cortical excitation and inhibition are driven by the same type of cell. Unlike for the phase-reversed

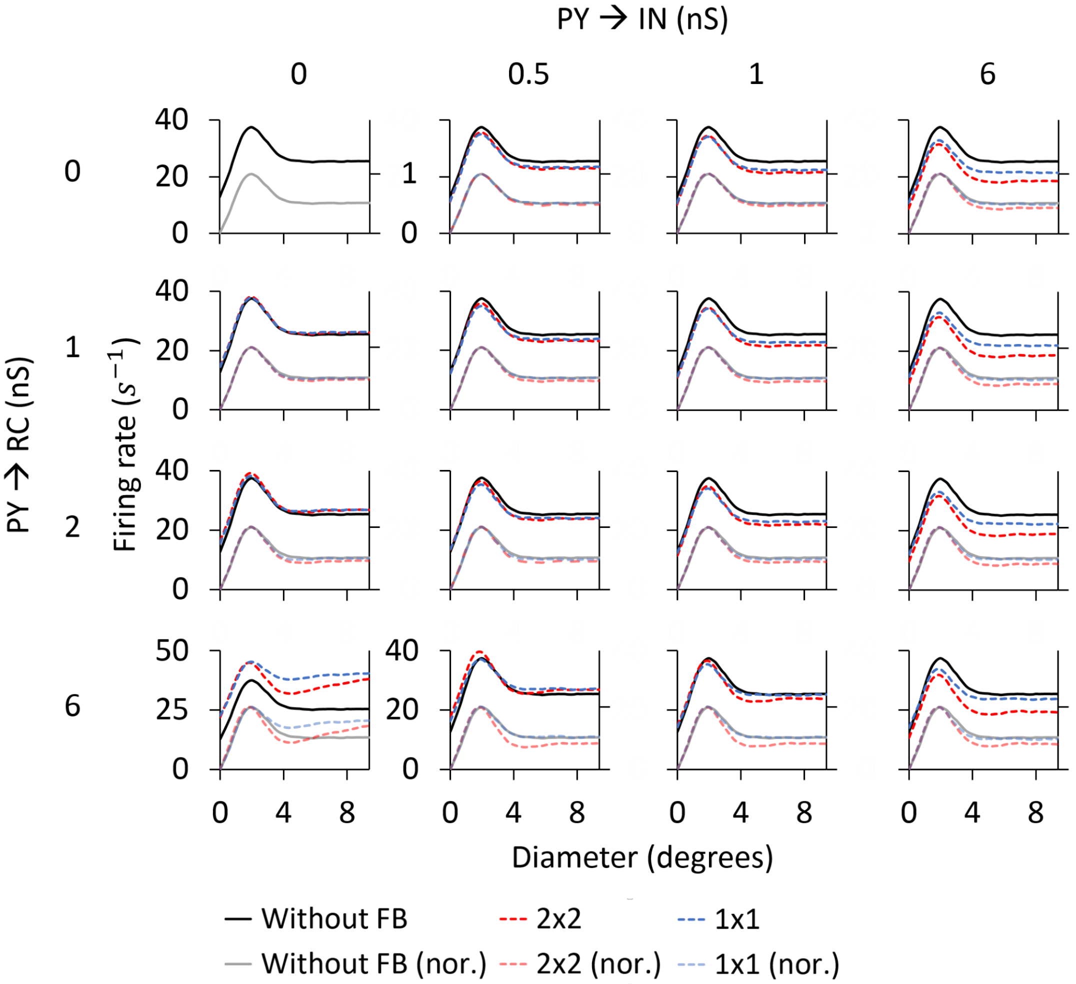

Fig 16. RC area-response curves for flashing spots for phase-reversed feedback. Normalized and unnormalized RC responses for different synapses weights between PYs and dLGN neurons, ranging from 0 (without feedback) to 6 nS, and for the two feedback spatial kernels: 1 × 1 and 2 × 2. Values shown for the synaptic weights represent the sum of all individual synaptic conductances of the same type converging to a given cell, i.e., for the 2 × 2 kernel, the value of every monosynaptic connection is the value depicted here divided by 4. The primary vertical axis of every panel (on the left) shows the values of the unnormalized response and the secondary vertical axis (on the right), the values of the normalized response, as shown for the panel in the first row and first column.

https://doi.org/10.1371/journal.pcbi.1005930.g016

feedback, the level of surround suppression in the RC is only increased when the excitatory feedback is absent, i.e., top rows in Figs 18 and 19. With excitatory feedback added (rows 2–4), the surround suppression is reduced. Thus with excitatory feedback present in addition to feedback inhibition, the surround suppression is always smaller for the phase-matched set-up compared to the phase-reversed set-up.

Two measures have been commonly been used to characterize area-response curves: the diameter giving the largest response (corresponding to the receptive-field center size for

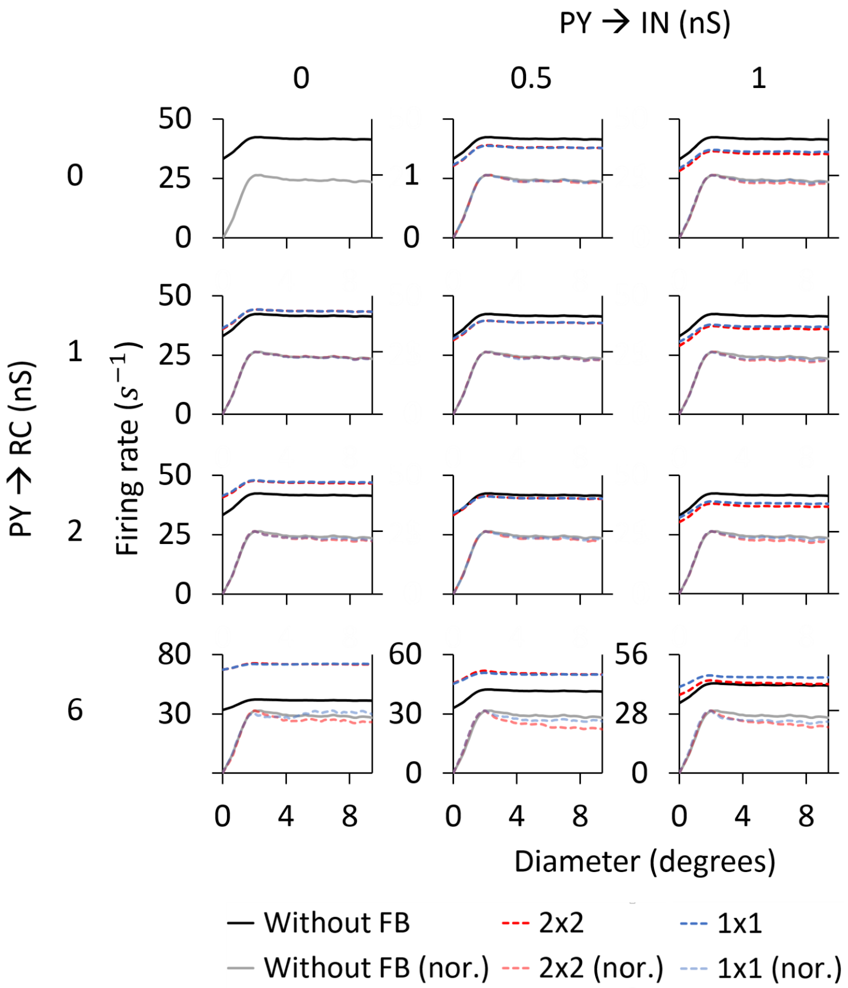

Fig 17. RC area-response curves for patch gratings for phase-reversed feedback. Normalized and unnormalized RC responses for different synapses weights between PYs and dLGN neurons, ranging from 0 (without feedback) to 6 nS, and for the two feedback spatial kernels: 1 × 1 and 2 × 2. Values shown for the synaptic weights represent the sum of all individual synaptic conductances of the same type converging to a given cell, i.e., for the 2 × 2 kernel, the value of every monosynaptic connection is the value depicted here divided by 4. The primary vertical axis of every panel (on the left) shows the values of the unnormalized response and the secondary vertical axis (on the right), the values of the normalized response, as shown for the panel in the first row and first column.

https://doi.org/10.1371/journal.pcbi.1005930.g017

flashing spots) and the center-surround antagonism [27, 28, 41]. In Fig 20 we show a summary of these response measures from the previous area-response curves (Figs 16–19).

We first consider the effects of cortical feedback on the center-surround antagonism coefficient (Fig 20A). Independently of the type of stimulus, there is a significant difference between the phase-reversed and phase-matched feedback configurations: in the phase-reversed case, high values of the center-surround antagonism coefficient are achieved by those parameter combinations that exert both strong excitation and inhibition to the RC (towards the bottom

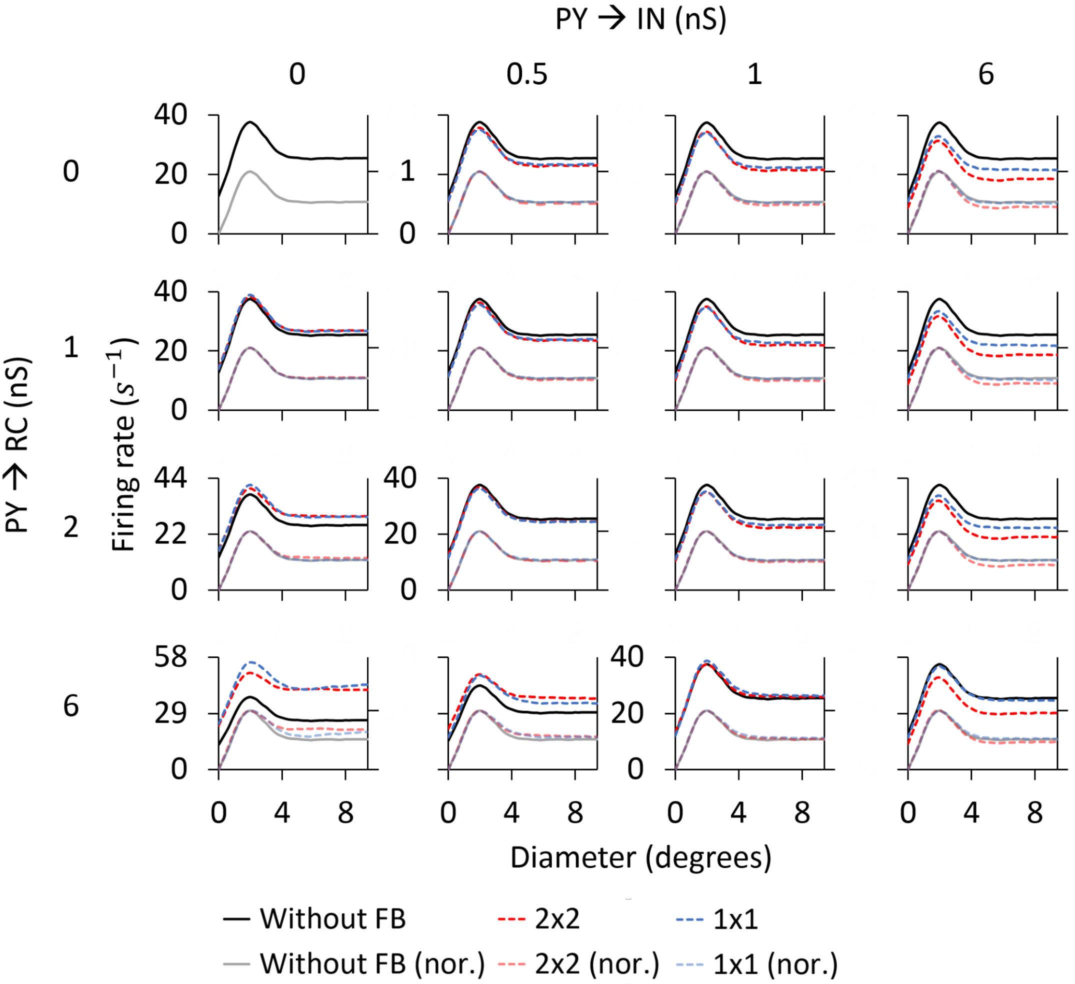

Fig 18. RC area-response curves for flashing spots for phase-matched feedback. Normalized and unnormalized RC responses for different synapses weights between PYs and dLGN neurons, ranging from 0 (without feedback) to 6 nS, and for the two feedback spatial kernels: 1 × 1 and 2 × 2. Values shown for the synaptic weights represent the sum of all individual synaptic conductances of the same type converging to a given cell, i.e., for the 2 × 2 kernel, the value of every monosynaptic connection is the value depicted here divided by 4. The primary vertical axis of every panel (on the left) shows the values of the unnormalized response and the secondary vertical axis (on the right), the values of the normalized response, as shown for the panel in the first row and first column.

https://doi.org/10.1371/journal.pcbi.1005930.g018

right corner), whereas, in the phase-matched case, only large values of inhibition can increase the center-surround antagonism coefficient (towards the top right corner).

For the same synaptic conductances for the feedback, the phase-reversed arrangement always gives the largest values of the center-surround antagonism coefficient. Further, with this configuration, cortical feedback always increases the center-surround antagonism more for the patch-grating than for the flashing spot. We also see that the wider feedback axonal arborization, i.e., 2 × 2, always gives larger surround suppression than the narrow 1 × 1.

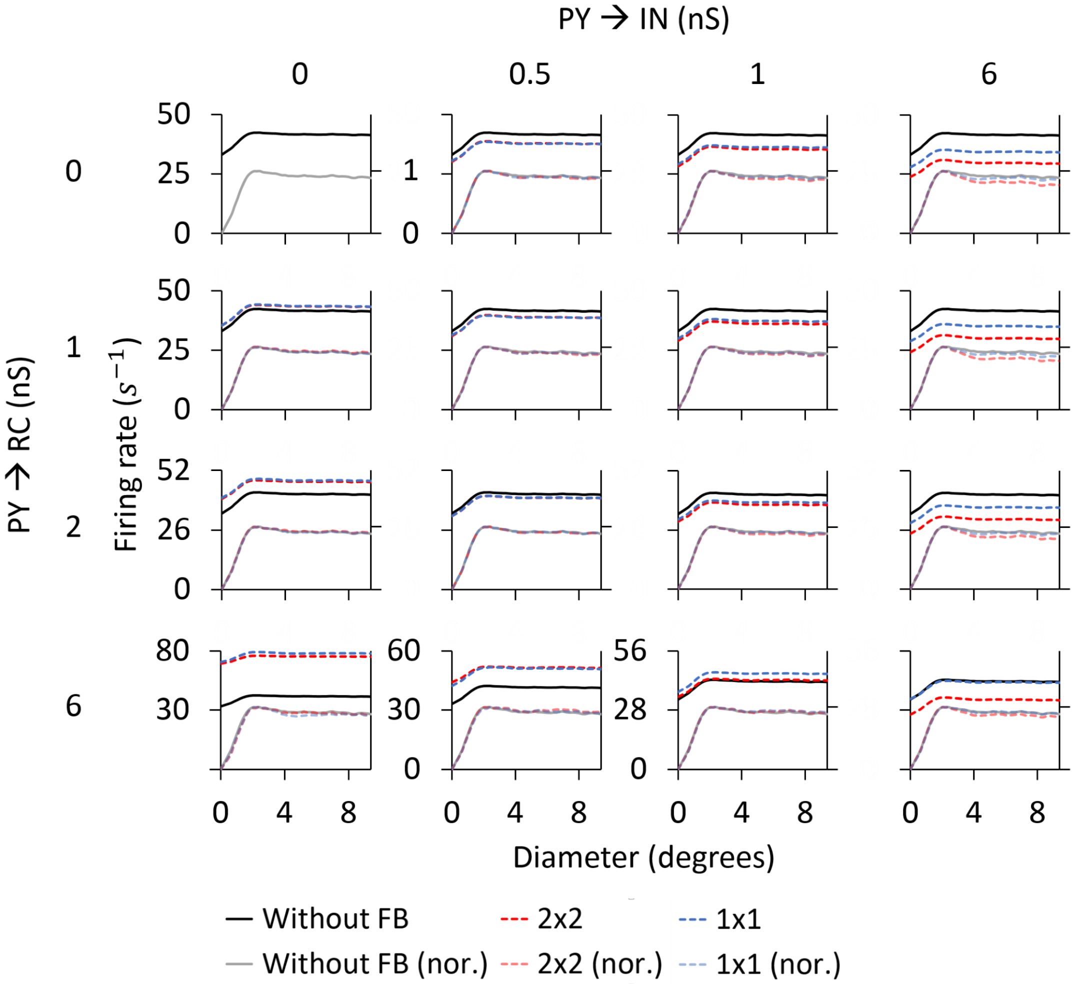

Fig 19. RC area-response curves for patch-grating for phase-matched feedback. Normalized and unnormalized RC responses for different synapses weights between PYs and dLGN neurons, ranging from 0 (without feedback) to 6 nS, and for the two feedback spatial kernels: 1 × 1 and 2 × 2. Values shown for the synaptic weights represent the sum of all individual synaptic conductances of the same type converging to a given cell, i.e., for the 2 × 2 kernel, the value of every monosynaptic connection is the value depicted here divided by 4. The primary vertical axis of every panel (on the left) shows the values of the unnormalized response and the secondary vertical axis (on the right), the values of the normalized response, as shown for the panel in the first row and first column.

https://doi.org/10.1371/journal.pcbi.1005930.g019

The sizes of the spot/patch that produce the maximal RC response are shown in Fig 20B. For the phase-reversed feedback, a reduction of the maximum-response size is seen for the patch grating when one or both types of cortical feedback is present. The same tendency, though less prominent, is seen also for flashing spots. Also for the phase-matched feedback, the maximum-response sizes are reduced by increasing inhibition to RCs. However, in the phase-matched case, excitatory feedback had the opposite effect compared to the phase-reversed case, i.e., excitation enlarged the maximum-response sizes.

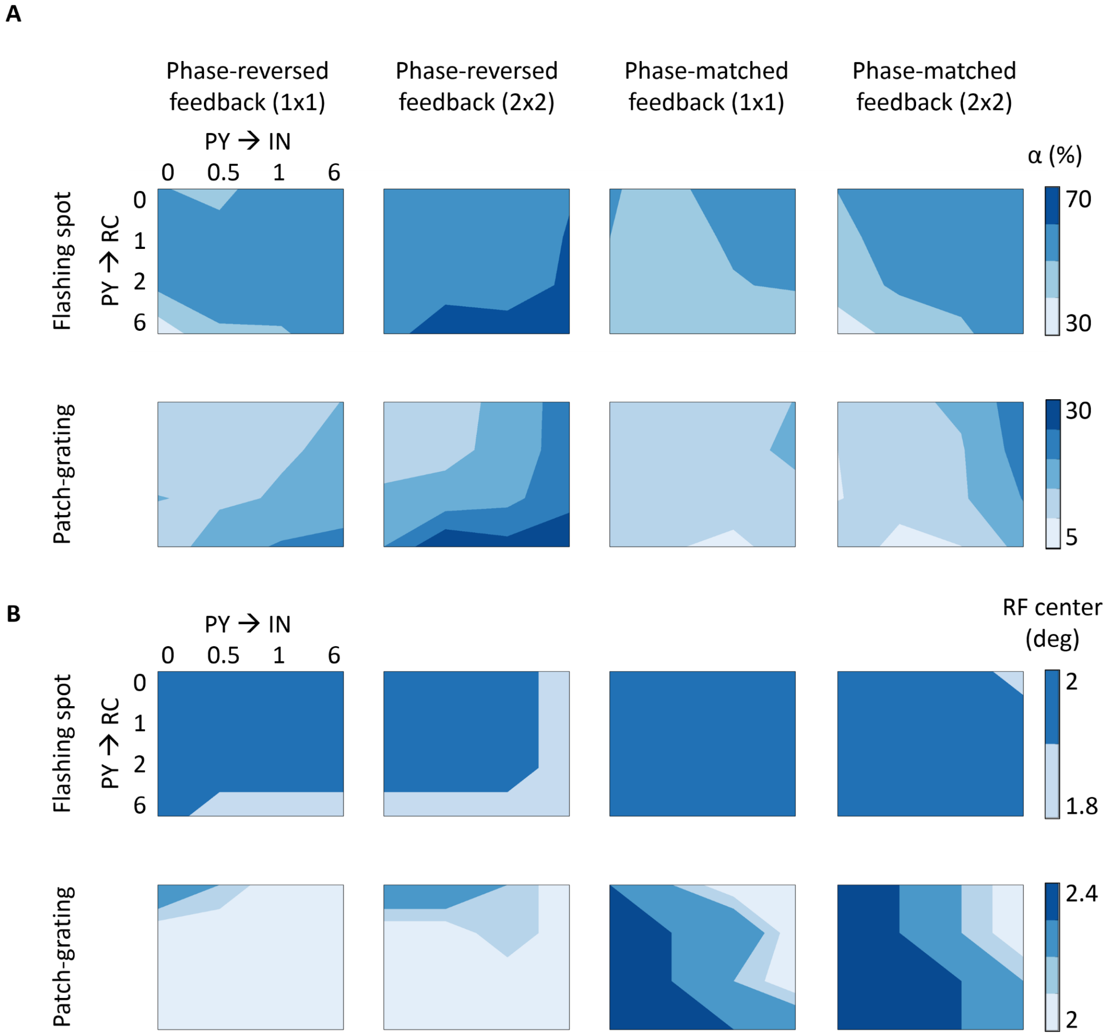

Fig 20. Summary of response measures for area-response curves. Contour plots of the center-surround antagonism coefficient (A) and stimulus diameters giving the largest response (corresponding to the receptive-field (RF) center for flashing spot) (B) as a function of synaptic weights and feedback spatial extent for the two phase arrangements considered: phase-reversed and phase-matched.

https://doi.org/10.1371/journal.pcbi.1005930.g020

Discussion

In the present paper we have developed a mechanistic network model of the thalamocortical system with explicit representations of LGN cells (relay cells (RCs) and interneurons (INs)) and orientation-selective layer 6 simple cells placed on two-dimensional spatial grids. The LGN and cortical cells are represented by biophysical neuron models based on the cable equation and Hodgkin-Huxley type active conductances. The input of the model is provided by retinal ganglion cells (GCs) implemented by means of descriptive filter models.

The main focus of the study has been exploration of the effects of cortical feedback on the spatial responses of RCs to flashing-spot and patch-grating stimuli as this has received substantial experimental attention [2, 4, 19, 32]. Comparison of our simulation results with previous experimental findings supports the notion that a 'push-pull' (phase-reversed) organization of cortical feedback [62], i.e., ON-center RCs receive direct (monosynaptic) excitatory feedback from OFF-dominated cortical cells and indirect inhibitory feedback from ON-dominated cortical cells, provides a dual effect that simultaneously amplifies excitatory responses in the receptive-field center and inhibitory responses in the receptive-field surround of RCs [18, 83]. As a result, the center-surround antagonism of RCs is amplified by cortical feedback and the maximum RC response occurs for reduced stimulus sizes. The combination of these two effects, excitatory in the receptive-field center [18] and inhibitory in the receptive-field surround [4, 19], may be understood as complementary functions that dynamically sharpens the spatial focus of the receptive field and increase their spatial resolution.

Model construction and validation

Feedforward model. The present work builds on our previous feedforward model that investigated the roles of triadic and axonal inhibition from dLGN INs on the RC response [41]. In the previous model, a single multicompartmental IN model incorporating dendrodendritic interaction between RCs and INs on triads [45] was used in combination with five single-compartment RC point-neuron models (adapted from [42]). Further, the parameters of the synaptic connections were fitted so that the model predicted flashing-spot area-response curves for RCs and GCs in accordance with experimental data from cat dLGN [27, 28]. In the present model the connectivity pattern for retinogeniculate and intrageniculate connections in [41] is kept. The plausibility of the RC and GC models was supported by the observation that their spatiotemporal receptive-field profiles (upper two rows of panels in Fig 4) were seen to be qualitatively similar to experimental observations [26].

With the present focus on how cortical feedback affects the RC response, we constructed a minimal model of layer 6 in the primary visual cortex including a single type of cortical cells, pyramidal cells (PYs). Further, the model in [41] was extended to include both ON- and OFF-center cells to allow for cross-symmetry thalamocortical and corticothalamic projections. Receptive fields of simple cortical cells are orientation-selective, and two orientation-selective cortical populations have been included in the model, one preferring horizontally-oriented stimuli, the other vertically-oriented stimuli. This orientation selectivity was constructed by tailoring thalamocortical excitatory inputs from 3 ON and 3 OFF RCs, each ON and OFF subregion spanning a patch of 3 deg × 1 deg in the visual field with a length/width ratio of about 2.5 [58–61] (Fig 1).

The resulting PY spatiotemporal receptive-field profiles was observed to resemble the experimentally-observed receptive field for the 'separable simple cell' in [26] (Fig 4). We further computed two receptive-field measures as described in [48, 69]: an overlap index (Eq 13) assessing the spatial segregation of subregions within the receptive field and a push-pull index (Eq 14) determining the relative weight of the antagonistic response to stimuli of opposite contrast, and confirmed that they were compatible with what has been observed for cortical simple cells [48, 69].

Feedback model. The detailed arrangement of the corticothalamic feedback provided by layer-6 cells is less known. We thus investigated several candidate feedback configurations both in terms of (i) the different phase arrangements from the ON and OFF zones in the visual cortex to the dLGN cells and (ii) the spatial divergence of the feedback. With regard to the phase arrangements between receptive fields of cortical cells and LGN cells, we have considered two different patterns (Fig 3): In the phase-reversed arrangement ('push-pull') [62], ON-center PYs synapse on ON-center INs while OFF-center PYs synapse on ON-center RCs. In the phase-matched arrangement ('push-push'), both ON-center INs and ON-center RCs receive feedback from ON-center PYs.

Previous studies (on cat LGN) have indicated that most interneuron action potentials can be accounted for by retinal input [64, 65]. Therefore, we chose to put cortical synapses distally on INs. With this setup, cortical feedback could increase the inhibition of RCs via dendrodendritic interaction with little effect on the IN firing rate (cf. Fig 11).

In terms of the spatial divergence of the corticothalamic axons, we have analyzed two feedback configurations: 1 × 1 and 2 × 2. In the 1 × 1 feedback, every PY synapses a single spatially overlapping RC and the corresponding IN dendrite. In the 2 × 2 feedback, every PY connects to four neighboring RCs and the four dendrites of a single IN. Such a spatially extended arrangement (2 × 2) is more in accordance with anatomical observations of the spatial spread of corticothalamic axons in cat dLGN [63].

Area-response curves

The main results from our model study were the area-response curves for flashing-spot and patch-grating stimuli, a commonly used measure of visual responses for cells in the early stages of the visual system [2, 4, 18, 19, 27, 28, 40, 80, 81].

We first considered the case with a rough balance between excitatory and inhibitory feedback so that the main effect of cortical feedback is on the shape of the area-response curves, not the magnitude (Figs 10 and 14). With a phase-reversed feedback arrangement a clear feedback-induced increase in surround suppression is observed both for flashing spots and patch gratings (Fig 10), as quantified by the center-surround antagonism coefficient α (Eq 12) (Table 4). Such a feedback-induced increase of surround suppression has been observed in experiments with both flashing spots [32] and patch gratings [4, 19], although the effect appears more significant for patch gratings [2, 4]. Our model results gave a larger increase of surround suppression for the patch-grating stimulus, but not as prominent as the increase reported by Sillito et al. [4]. With the same choice of parameters, a phase-matched feedback arrangement resulted in very little change in surround suppression for both types of stimulus (Fig 14).

Increased surround suppression implies that RC cells in relative terms become more responsive to small stimuli and, thus, the cell more selective in spatial tuning. An additional effect of the phase-reversed feedback is the shrinking of the stimulus size giving the maximum responses in the area-response curves, clearly observed for the phase-reversed feedback, but largely absent for phase-matched feedback (Figs 10 and 14).

We next did a parameter sweep, i.e., investigated the effects of cortical feedback on the RC area-response curves for a wide range of different synaptic weights between PYs and dLGN neurons and for the different spatial feedback kernels (1 × 1 and 2 × 2) (Figs 16–19). The results for our two key area-response curve measures, the stimulus diameters giving the largest response and the center-surround antagonism coefficient α, were summarized in Fig 20.

A first observation was that both for flashing-spot and patch-grating stimuli, the phase-reversed and phase-matched cases gave very different dependency of the center-surround suppression, i.e., center-surround antagonism coefficient α, on synaptic weights (Fig 20A). For the phase-reversed case, high values of the center-surround antagonism coefficient were achieved by those parameter combinations that exert both strong excitation and (indirect) inhibition to the RC (towards the bottom right corner). Here the ON-center inhibition and the OFF-center excitation both contribute to increasing the surround suppression. Thus large values of the surround suppression can be achieved even when excitatory and inhibitory effects are roughly balanced [18, 83]. In contrast, for the phase-matched case, feedback-induced increases in the center-surround antagonism coefficient α required the inhibition to dominate the excitation. This reflects that the effects of ON-center inhibition and ON-center excitation in the feedback tend to cancel each other out. This is in accordance with the observation in Figs 10 and 14 where the area-response curve for the 'inhibition-only' case was seen to represent an intermediate case between the phase-reversed and phase-matched situations.

When comparing the different spatial feedback patterns for the phase-reversed case, the 2 × 2 feedback pattern was seen to be more effective in increasing surround suppression in the RC response than the 1 × 1. Incidentally, a spatially widespread feedback pattern has been suggested by anatomical studies of the innervation pattern of corticothalamic axons in the dLGN [63].

For flashing-spot stimuli only small variations in the diameters producing the maximal RC response were observed when varying the synaptic weights (Fig 20B). However, for patch-grating stimuli a reduction was observed in the maximum-response diameter was observed when one or both types of cortical feedback were present.

Comparison with previous modeling approaches

Other modeling studies have also investigated the effect of cortical feedback on spatial processing of RCs with different stimulus patterns [39, 40]. The focus in [39] was on exploring the role of cortical feedback in modulating RC responses to discontinuity in orientations in gratings in bipartite stimuli. In [40] the extended DOG (eDOG) model was introduced, allowing for analytical explorations of effects of cortical feedback in certain settings, i.e., with certain combinations of excitatory and (indirect) inhibitory feedback from ON- and OFF-center cortical cells onto RCs. There a preliminary use-case showed that a phase-reversed ('push-pull') arrangement of cortical feedback where ON-center RCs receive direct excitation from OFF-driven cortical cells and balanced indirect inhibitory feedback from ON-driven cortical cells, may provide increased center-surround antagonism.

Our biophysical model and the above-discussed firing-rate models represent opposite extremes in terms of biological detail in LGN circuit models [86]. Models at an intermediate complexity level where the cells are modeled as integrate-and-fire neurons have also been used to explore cortical feedback effects on LGN cell [33–36]. However, these have focused on temporal response properties such as feedback-induced spike synchronization [35], long-lasting correlations [36] and effects of feedback on visual latency [33], not the spatial properties which has been the main topic here.

Future model applications and model extensions

An obvious next application of the present model would be to explore temporal response properties of LGN cells and, in particular, how these are affected by various types of cortical feedback. One line of inquiry would be to explore the relative roles of feedforward and feedback connections in shaping the temporal receptive fields of LGN cells, analogous to the questions addressed by the firing-rate models in [37] and [38]. Another line of research would be on studying spike synchronicity and correlations as addressed earlier with integrate-and-fire models [35, 36]. A third line could be to explore in detail how the temporal structure of the PSTH, and in particular the 'interval histogram' of RC spikes, is affected by feedback [34].

In addition to feedback from cortex, both RCs and INs receive inhibitory feedback from neurons in the thalamic reticular nucleus (TRN) [5]. TRN neurons are thought to play a key role in the process of sleep spindle oscillations generated within the thalamic circuitry [42, 43].

The TRN also contributes to the control of visual attention and awareness [87], but the effects on procession of visual signals remain poorly understood [88]. TRN neurons do not receive direct input from the retina as LGN INs, instead they receive feedforward visual signals from collaterals of geniculocortical axons. TRN neurons also receive cortical feedback through corticothalamic axons, and their synapses on RCs are situated in close proximity to those of corticothalamic axons [1]. Given this organization of synaptic connections and its position within the network, TRN cells are likely to influence the transfer of visual information in a different manner than LGN INs. Modeling studies exploring the putative role of TRN neurons on visual processing have already been pursued [89], and the present biophysical model could be extended to include also such neurons when more is known about these neurons and their possible role in visual processing.

The present model assumes static synapses while a number of studies have demonstrated short-term plasticity in different synapses of the thalamocortical circuit, i.e., short-term depression at the retinogeniculate [90, 91] and geniculocortical [92, 93] synapses, as well as in the feedback connection from cortex to INs [94]. In contrast, the feedback connection from cortex to RCs appears to be facilitating [90, 95]. Such plasticity opens up for an even richer dynamical repertoire of the circuit, and would be an interesting topic for a future study using the present model with static synapses as a starting point. In particular, it would be interesting to explore if short-term synaptic plasticity could affect our prediction that phase-reversed cortical feedback is the most effective mechanism for increasing center-surround antagonism.

dLGN cells have two different response modes, burst and tonic, suggested to relate of the animal [5, 96, 97]. Modulatory inputs from other parts of the brain may switch between these modes by shifting the baseline membrane potentials of RCs and INs. Tonic firing has been suggested to be more suitable for transferring visual information because it avoids nonlinear distortions created during burst firing, while burst firing was suggested to be best suited as an 'alarm clock', i.e., rapid stimulus detection [5]. Recent studies have demonstrated, however, that thalamic bursts can also contribute to sensory processing [98–101]. In the current study, our RC and IN models were based on data from dLGN neurons that rested on relatively depolarized membrane potentials, -60 mV and -63 mV, respectively, and fired predominantly in the tonic mode (Fig 2). An exploration of the functional roles of the two firing modes, and putative switches between them, would be another natural extension of the present work.

The present model of primary visual cortex is obviously simplified. Cells in layer 4 of cortex are the main targets of projections from RCs, while the feedback from cortex to dLGN comes from cells in layer 6. Even though there are also projections from RCs to layer-6 cells, there are likely cross-layer processing in cortex that affects the thalamocortical feedback loop and difficult to capture by a single-layer cortex model. Despite the model simplicity, the pyramidal-cell receptive fields produced by our network model (Figs 4, 12 and 15) are nevertheless seen to resemble the receptive fields of simple cells which also has been observed in layer 6 of cat visual cortex [102]. Thus the error introduced by our simplified cortical network model could be modest for the present application, but this needs further exploration when thalamocortical models including more comprehensive cortical circuitry becomes available.

Further, there are several neural mechanisms that our simplified model of cortical orientation tuning does not account for, such as recurrent cortical excitation or horizontal inhibitory connections [58, 103–105], which can amplify a weak orientation bias. Although the area-response curves of cortical cells to the patch grating in Figs 8 and 9 showed a marked difference for gratings at preferred and non-preferred orientations, stimuli presented at non-preferred orientations did not suppress cortical response to the background rate as observed experimentally in some cells [106]. A stronger orientation selectivity of the cortical cells would likely affect the feedback-induced changes in RC response, but how, and to what extent, remains to be explored.

While one option for extending the present model would be to add more neuron types to a single-layer cortex model, it might be tempting to aim to connect the present biophysically detailed model for the dLGN circuit with an equally detailed model for the primary visual cortex. However, at present such models are lacking, and a comprehensive model based on biophysical neuron models including both the dLGN and, say, V1 would anyway be computationally extremely demanding. An alternative could be to instead model V1 dynamics with simpler neuron models such as the Potjans-Diesmann network model based on integrate-and-fire neurons [107].

Experimental studies of cortical feedback effects on response properties in the dLGN have been ongoing for at least 40 years (see, e.g., [7]). However, a recurring challenge has been to reversibly remove cortical feedback in a controlled manner to compare physiological responses of dLGN cells with and without cortical feedback. Both cooling [11] and pharmacological manipulations [18] have been used. However, the advent of optogenetics now offers unprecedented opportunities for highly-controlled activation or deactivation of individual cell types. In [108] the role of layer-6 cells in providing gain control for the visual responses in the upper layers of mouse visual cortex was studied by such techniques. A similar study where visual responses of dLGN cells are measured while the corticothalamic cells in layer 6 are selectively activated or deactivated by photostimulation, would be most welcome for testing predictions of the present model.

Acknowledgments

Simulations were parallelized using the Stallo supercomputer cluster at Notur, the Norwegian metacenter for computational science.

We wish to thank Thomas Heiberg and Torbjørn Vefferstad Ness for their helpful inputs and discussions. This work was started while P. Martínez-Cañada was on research stay at CINPLA, University of Oslo. He wishes to thank staff of this institution for their hospitality and support.

Author Contributions

Conceptualization: Pablo Martínez-Cañada, Milad Hobbi Mobarhan, Geir Halnes, Gaute T. Einevoll.

Methodology: Pablo Martínez-Cañada, Milad Hobbi Mobarhan, Geir Halnes, Gaute T. Einevoll.

Project administration: Marianne Fyhn, Christian Morillas, Francisco Pelayo, Gaute T. Einevoll.

Software: Pablo Martínez-Cañada.

Writing – original draft: Pablo Martínez-Cañada, Gaute T. Einevoll.

Writing – review & editing: Pablo Martínez-Cañada, Milad Hobbi Mobarhan, Geir Halnes, Marianne Fyhn, Christian Morillas, Francisco Pelayo, Gaute T. Einevoll.

References

1. Usrey WM, Alitto HJ. Visual functions of the thalamus. Annual Review of Vision Science. 2015; 1:351–371. https://doi.org/10.1146/annurev-vision-082114-035920 PMID: 28217740

2. Sillito AM, Cudeiro J, Jones HE. Always returning: feedback and sensory processing in visual cortex and thalamus. Trends in Neurosciences. 2006; 29(6):307–316. https://doi.org/10.1016/j.tins.2006.05.001 PMID: 16713635

3. Cudeiro J, Sillito AM. Looking back: corticothalamic feedback and early visual processing. Trends in Neurosciences. 2006; 29(6):298–306. https://doi.org/10.1016/j.tins.2006.05.002 PMID: 16712965

4. Sillito AM, Jones HE. Corticothalamic interactions in the transfer of visual information. Philosophical Transactions of the Royal Society of London B: Biological Sciences. 2002; 357(1428):1739–1752. https://doi.org/10.1098/rstb.2002.1170 PMID: 12626008

5. Sherman SM, Guillery R. The role of the thalamus in the flow of information to the cortex. Philosophical Transactions of the Royal Society of London B: Biological Sciences. 2002; 357(1428):1695–1708. https://doi.org/10.1098/rstb.2002.1161 PMID: 12626004

6. Sherman SM, Guillery RW. Exploring the thalamus. Elsevier; 2001.

7. Tsumoto T, Creutzfeldt OD, Legendy CR Functional organization of the corticofugal system from visual cortex to lateral geniculate nucleus in the cat. Experimental Brain Research 1978; 32:345–364. https://doi.org/10.1007/BF00238707 PMID: 210031

8. Geisert EE, Langsetmo A, Spear PD. Influence of the cortico-geniculate pathway on response properties of cat lateral geniculate neurons. Brain Research 1981; 208(2):409–415. https://doi.org/10.1016/0006-8993(81)90568-0 PMID: 6260290

9. Vidyasagar TR, Urbas JV. Orientation sensitivity of cat LGN neurones with and without inputs from visual cortical areas 17 and 18. Experimental Brain Research. 1982; 46:157–69. https://doi.org/10.1007/BF00237172 PMID: 7095028

10. Marrocco RT, McClurkin JW, Young RA. Modulation of lateral geniculate nucleus cell responsiveness by visual activation of the corticogeniculate pathway. Journal of Neuroscience 1982; 2(2):256–263. PMID: 7062107

11. McClurkin JW, Marrocco RT. Visual cortical input alters spatial tuning in monkey lateral geniculate nucleus cells. Journal of Physiology 1984; 348:135–152. https://doi.org/10.1113/jphysiol.1984.sp015103 PMID: 6716281

12. Murphy P, Sillito A. Corticofugal feedback influences the generation of length tuning in the visual pathway. Nature. 1987;. https://doi.org/10.1038/329727a0

13. Sillito A, Cudeiro J, Murphy P. Orientation sensitive elements in the corticofugal influence on centre-surround interactions in the dorsal lateral geniculate nucleus. Experimental Brain Research. 1993; 93(1):6–16. https://doi.org/10.1007/BF00227775 PMID: 8467892

14. Sillito AM, Jones HE, Gerstein GL, West DC. Feature-linked synchronization of thalamic relay cell firing induced by feedback from visual cortex. Nature. 1994; 369:479–482. https://doi.org/10.1038/369479a0 PMID: 8202137

15. Cudeiro J, Sillito A. Spatial frequency tuning of orientation-discontinuity-sensitive corticofugal feedback to the cat lateral geniculate nucleus. Journal of Physiology. 1996; 490(2):481–492. https://doi.org/10.1113/jphysiol.1996.sp021159 PMID: 8821144

16. Jones HE, Andolina IM, Oakely NM, Murphy PC, Sillito AM. Spatial summation in lateral geniculate nucleus and visual cortex. Experimental Brain Research. 2000; 135(2):279–284. https://doi.org/10.1007/s002210000574 PMID: 11131514

17. Andolina IM, Jones HE, Wang W, Sillito AM. Corticothalamic feedback enhances stimulus response precision in the visual system. Proceedings of the National Academy of Sciences (USA). 2007; 104(5):1685–1690. https://doi.org/10.1073/pnas.0609318104

18. Jones HE, Andolina IM, Ahmed B, Shipp SD, Clements JT, Grieve KL, et al. Differential feedback modulation of center and surround mechanisms in parvocellular cells in the visual thalamus. Journal of Neuroscience. 2012; 32(45):15946–15951. https://doi.org/10.1523/JNEUROSCI.0831-12.2012 PMID: 23136432

19. Andolina IM, Jones HE, Sillito AM. Effects of cortical feedback on the spatial properties of relay cells in the lateral geniculate nucleus. Journal of Neurophysiology. 2013; 109(3):889–899. https://doi.org/10.1152/jn.00194.2012 PMID: 23100142

20. Wang W, Andolina IM, Lu Y, Jones HE, Sillito AM. Focal Gain Control of Thalamic Visual Receptive Fields by Layer 6 Corticothalamic Feedback. Cerebral Cortex. 2018; 28(1):267–280. PMID: 27988493

21. McCormick DA, von Krosigk M. Corticothalamic activation modulates thalamic firing through glutamate'metabotropic' receptors. Proceedings of the National Academy of Sciences (USA). 1992; 89:2774–2778. https://doi.org/10.1073/pnas.89.7.2774

22. Godwin DW, Vaughan JW, Sherman SM. Metabotropic glutamate receptors switch visual response mode of lateral geniculate nucleus cells from burst to tonic. Journal of Neurophysiology. 1996; 76:1800–1816. https://doi.org/10.1152/jn.1996.76.3.1800 PMID: 8890293

23. Briggs F, Usrey WM. Corticogeniculate feedback and visual processing in the primate. Journal of Physiology. 2011; 589(Pt 1):33–40. https://doi.org/10.1113/jphysiol.2010.193599 PMID: 20724361

24. Alitto HJ, Usrey WM. Dissecting the dynamics of corticothalamic feedback. Neuron. 2015; 86:605–607. https://doi.org/10.1016/j.neuron.2015.04.016 PMID: 25950627

25. Enroth-Cugell C, Robson JG. The contrast sensitivity of retinal ganglion cells of the cat. Journal of Physiology. 1966; 187(3):517–552. https://doi.org/10.1113/jphysiol.1966.sp008107 PMID: 16783910

26. DeAngelis GC, Ohzawa I, Freeman RD. Receptive-field dynamics in the central visual pathways. Trends in Neurosciences. 1995; 18(10):451–458. https://doi.org/10.1016/0166-2236(95)94496-R PMID: 8545912

27. Ruksenas O, Fjeld I, Heggelund P. Spatial summation and center-surround antagonism in the receptive field of single units in the dorsal lateral geniculate nucleus of cat: comparison with retinal input. Visual Neuroscience. 2000; 17(6):855–870. https://doi.org/10.1017/S0952523800176059 PMID: 11193102

28. Einevoll GT, Heggelund P. Mathematical models for the spatial receptive-field organization of nonlagged X-cells in dorsal lateral geniculate nucleus of cat. Visual Neuroscience. 2000; 17(06):871–885. https://doi.org/10.1017/S0952523800176060 PMID: 11193103

29. Barlow H. Possible principles underlying the transformation of sensory messages. In: Rosenblith WA, editor: Sensory Communication. MIT Press; 1961.

30. Webb BS, Tinsley CJ, Barraclough NE, Easton A, Parker A, Derrington AM. Feedback from V1 and inhibition from beyond the classical receptive field modulates the responses of neurons in the primate lateral geniculate nucleus. Visual Neuroscience. 2002; 19(5):583–592. https://doi.org/10.1017/S0952523802195046 PMID: 12507325

31. Przybyszewski AW, Gaska JP, Foote W, Pollen DA. Striate cortex increases contrast gain of macaque LGN neurons. Visual Neuroscience. 2000; 17(04):485–494. https://doi.org/10.1017/S0952523800174012 PMID: 11016570

32. De Labra C, Rivadulla C, Grieve K, Mariño J, Espinosa N, Cudeiro J. Changes in visual responses in the feline dLGN: selective thalamic suppression induced by transcranial magnetic stimulation of V1. Cerebral Cortex. 2007; 17(6):1376–1385. https://doi.org/10.1093/cercor/bhl048 PMID: 16908494

33. Köhn J, Wörgötter F. Corticofugal feedback can reduce the visual latency of responses to antagonistic stimuli. Biological Cybernetics. 1996; 75(3):199–209. https://doi.org/10.1007/s004220050287 PMID: 8900035

34. Wörgötter F, Nelle E, B L, Funke K. The influence of corticofugal feedback on the temporal structure of visual response of cat thalamic relay cells. Journal of Physiology. 1998; 509:797–815. https://doi.org/10.1111/j.1469-7793.1998.797bm.x PMID: 9596801

35. Kirkland KL, Gerstein GL. A model of cortically induced synchronization in the lateral geniculate nucleus of the cat: a role for low-threshold calcium channels. Vision Research. 1998; 38(13):2007–2022. https://doi.org/10.1016/S0042-6989(97)00385-4 PMID: 9797947

36. Kirkland KL, Sillito AM, Jones HE, West DC, Gerstein GL. Oscillations and long-lasting correlations in a model of the lateral geniculate nucleus and visual cortex. Journal of Neurophysiology. 2000; 84 (4):1863–1868. https://doi.org/10.1152/jn.2000.84.4.1863 PMID: 11024078

37. Yousif N, Denham M. The role of cortical feedback in the generation of the temporal receptive field responses of lateral geniculate nucleus neurons: a computational modelling study. Biological Cybernetics. 2007; 97(4):269–277. https://doi.org/10.1007/s00422-007-0171-3 PMID: 17657507

38. Norheim ES, Wyller J, Nordlie E, Einevoll GT. A minimal mechanistic model for temporal signal processing in the lateral geniculate nucleus. Cognitive Neurodynamics. 2012; 6(3):259–281. https://doi.org/10.1007/s11571-012-9198-9 PMID: 23730357

39. Hayot F, Tranchina D. Modelling corticofugal feedback and the sensitivity of lateral genculate neurons to orientation discontinuity. Visual Neuroscience. 2001; 18(6):865–878. PMID: 12020077

40. Einevoll GT, Plesser HE. Extended difference-of-Gaussians model incorporating cortical feedback for relay cells in the lateral geniculate nucleus of cat. Cognitive Neurodynamics. 2012; 6(4):307–324. https://doi.org/10.1007/s11571-011-9183-8 PMID: 24995047

41. Heiberg T, Hagen E, Halnes G, Einevoll GT. Biophysical Network Modelling of the dLGN Circuit: Different Effects of Triadic and Axonal Inhibition on Visual Responses of Relay Cells. PLoS Computational Biology. 2016; 12(5):e1004929. https://doi.org/10.1371/journal.pcbi.1004929 PMID: 27203421

42. Destexhe A, Bal T, McCormick DA, Sejnowski TJ. Ionic mechanisms underlying synchronized oscillations and propagating waves in a model of ferret thalamic slices. Journal of Neurophysiology. 1996; 76(3):2049–2070. https://doi.org/10.1152/jn.1996.76.3.2049 PMID: 8890314

43. Destexhe A, Contreras D, Steriade M. Mechanisms underlying the synchronizing action of corticothalamic feedback through inhibition of thalamic relay cells. Journal of Neurophysiology. 1998; 79 (2):999–1016. https://doi.org/10.1152/jn.1998.79.2.999 PMID: 9463458

44. McCormick DA, Wang Z, Huguenard J. Neurotransmitter control of neocortical neuronal activity and excitability. Cerebral Cortex. 1993; 3(5):387–398. https://doi.org/10.1093/cercor/3.5.387 PMID: 7903176

45. Halnes G, Augustinaite S, Heggelund P, Einevoll GT, Migliore M. A multi-compartment model for interneurons in the dorsal lateral geniculate nucleus. PLoS Computational Biology. 2011; 7(9):e1002160. https://doi.org/10.1371/journal.pcbi.1002160 PMID: 21980270

46. Binzegger T, Douglas RJ, Martin KA. A quantitative map of the circuit of cat primary visual cortex. Journal of Neuroscience. 2004; 24(39):8441–8453. https://doi.org/10.1523/JNEUROSCI.1400-04.2004 PMID: 15456817

47. Martinez LM, Molano-Mazón M, Wang X, Sommer FT, Hirsch JA. Statistical wiring of thalamic receptive fields optimizes spatial sampling of the retinal image. Neuron. 2014; 81(4):943–956. https://doi.org/10.1016/j.neuron.2013.12.014 PMID: 24559681

48. Hirsch JA, Martinez LM. Circuits that build visual cortical receptive fields. Trends in Neurosciences. 2006; 29(1):30–39. https://doi.org/10.1016/j.tins.2005.11.001 PMID: 16309753

49. Martínez-Cañada P, Morillas C, Pino B, Ros E, Pelayo F. A Computational Framework for Realistic Retina Modeling. International Journal of Neural Systems. 2016; 26(07):1650030. https://doi.org/10.1142/S0129065716500301 PMID: 27354192

50. Wohrer A, Kornprobst P. Virtual retina: a biological retina model and simulator, with contrast gain control. Journal of Computational Neuroscience. 2009; 26(2):219–249. https://doi.org/10.1007/s10827-008-0108-4 PMID: 18670870

51. Mante V, Bonin V, Carandini M. Functional mechanisms shaping lateral geniculate responses to artificial and natural stimuli. Neuron. 2008; 58(4):625–638. https://doi.org/10.1016/j.neuron.2008.03.011 PMID: 18498742

52. Einevoll GT, Plesser HE. Response of the difference-of-Gaussians model to circular drifting-grating patches. Visual Neuroscience. 2005; 22(4):437–446. https://doi.org/10.1017/S0952523805224057 PMID: 16212701

53. Usrey WM, Reppas JB, Reid RC. Specificity and strength of retinogeniculate connections. Journal of Neurophysiology. 1999; 82(6):3527–3540. https://doi.org/10.1152/jn.1999.82.6.3527 PMID: 10601479

54. Allken V, Chepkoech JL, Einevoll GT, Halnes G. The subcellular distribution of T-type Ca2+ channels in interneurons of the lateral geniculate nucleus. PLoS One. 2014; 9(9):e107780. https://doi.org/10.1371/journal.pone.0107780 PMID: 25268996

55. Bloomfield SA, Sherman SM. Dendritic current flow in relay cells and interneurons of the cat's lateral geniculate nucleus. Proceedings of the National Academy of Sciences (USA). 1989; 86(10):3911–3914. https://doi.org/10.1073/pnas.86.10.3911

56. Schutter ED. Computational modeling methods for neuroscientists. The MIT Press; 2009.

57. Martinez LM, Alonso JM. Complex receptive fields in primary visual cortex. The Neuroscientist. 2003; 9(5):317–331. https://doi.org/10.1177/1073858403252732 PMID: 14580117

58. Ferster D, Miller KD. Neural mechanisms of orientation selectivity in the visual cortex. Annual Review of Neuroscience. 2000; 23(1):441–471. https://doi.org/10.1146/annurev.neuro.23.1.441 PMID: 10845071

59. Hubel DH, Wiesel TN. Receptive fields, binocular interaction and functional architecture in the cat's visual cortex. Journal of Physiology. 1962; 160(1):106–154. https://doi.org/10.1113/jphysiol.1962.sp006837 PMID: 14449617

60. Alonso JM, Usrey WM, Reid RC. Rules of connectivity between geniculate cells and simple cells in cat primary visual cortex. Journal of Neuroscience. 2001; 21(11):4002–4015. PMID: 11356887

61. Reid RC, Alonso JM, et al. Specificity of monosynaptic connections from thalamus to visual cortex. Nature. 1995; 378(6554):281–283. https://doi.org/10.1038/378281a0 PMID: 7477347

62. Wang W, Jones HE, Andolina IM, Salt TE, Sillito AM. Functional alignment of feedback effects from visual cortex to thalamus. Nature Neuroscience. 2006; 9(10):1330–1336. https://doi.org/10.1038/nn1768 PMID: 16980966

63. Murphy PC, Sillito AM. Functional morphology of the feedback pathway from area 17 of the cat visual cortex to the lateral geniculate nucleus. Journal of Neuroscience. 1996; 16(3):1180–1192. PMID: 8558247

64. Montero V. A quantitative study of synaptic contacts on interneurons and relay cells of the cat lateral geniculate nucleus. Experimental Brain Research. 1991; 86(2):257–270. https://doi.org/10.1007/BF00228950 PMID: 1756802

65. Dubin MW, Cleland BG. Organization of visual inputs to interneurons of lateral geniculate nucleus of the cat. Journal of Neurophysiology. 1977; 40(2):410–427. https://doi.org/10.1152/jn.1977.40.2.410 PMID: 191574

66. Alitto HJ, Usrey WM. Surround suppression and temporal processing of visual signals. Journal of Neurophysiology. 2015; 113(7):2605–2617. https://doi.org/10.1152/jn.00480.2014 PMID: 25652919

67. Troyer TW, Krukowski AE, Priebe NJ, Miller KD. Contrast-invariant orientation tuning in cat visual cortex: thalamocortical input tuning and correlation-based intracortical connectivity. Journal of Neuroscience. 1998; 18(15):5908–5927. PMID: 9671678

68. DeAngelis GC, Ohzawa I, Freeman R. Spatiotemporal organization of simple-cell receptive fields in the cat's striate cortex. I. General characteristics and postnatal development. Journal of Neurophysiology. 1993; 69(4):1091–1117. https://doi.org/10.1152/jn.1993.69.4.1091 PMID: 8492151

69. Martinez LM, Wang Q, Reid RC, Pillai C, Alonso JM, Sommer FT, et al. Receptive field structure varies with layer in the primary visual cortex. Nature Neuroscience. 2005; 8(3):372–379. https://doi.org/10.1038/nn1404 PMID: 15711543

70. Langtangen HP. A primer on scientific programming with Python. vol. 2. Springer; 2009.

71. Lindén H, Hagen E, Leski S, Norheim ES, Pettersen KH, Einevoll GT. LFPy: a tool for biophysical simulation of extracellular potentials generated by detailed model neurons. Frontiers in Neuroinformatics. 2014; 7:41. https://doi.org/10.3389/fninf.2013.00041 PMID: 24474916

72. Hines ML, Carnevale NT. NEURON: a tool for neuroscientists. The Neuroscientist. 2001; 7(2):123–135. https://doi.org/10.1177/107385840100700207 PMID: 11496923

73. Hines ML, Carnevale NT. Discrete event simulation in the NEURON environment. Neurocomputing. 2004; 58:1117–1122. https://doi.org/10.1016/j.neucom.2004.01.175

74. Eppler JM, et al. NEST 2.8.0. Zenodo.; 2015. Available from: http://dx.doi.org/10.5281/zenodo.32969.

75. Gewaltig MO, Diesmann M. NEST (neural simulation tool). Scholarpedia. 2007; 2(4):1430. https://doi.org/10.4249/scholarpedia.1430

76. HPC group—UiT The Arctic University of Norway. Stallo supercomputer; 2016. Available from: http://hpc-uit.readthedocs.io/.

77. Gropp W, Lusk E, Skjellum A. Using MPI: portable parallel programming with the message-passing interface. vol. 1. MIT press; 1999.

78. Dalcin LD, Paz RR, Kler PA, Cosimo A. Parallel distributed computing using python. Advances in Water Resources. 2011; 34(9):1124–1139. https://doi.org/10.1016/j.advwatres.2011.04.013

79. Hirsch JA, Alonso JM, Reid RC, Martinez LM. Synaptic integration in striate cortical simple cells. Journal of Neuroscience. 1998; 18(22):9517–9528. PMID: 9801388

80. Einevoll GT, Jurkus P, Heggelund P. Coarse-to-fine changes of receptive fields in lateral geniculate nucleus have a transient and a sustained component that depend on distinct mechanisms. PLoS ONE. 2011; 6(9):e24523. https://doi.org/10.1371/journal.pone.0024523 PMID: 21931739

81. Ruksenas O, Bulatov A, Heggelund P. Dynamics of spatial resolution of single units in the lateral geniculate nucleus of cat during brief visual stimulation. Journal of Neurophysiology. 2007; 97(2):1445–1456. https://doi.org/10.1152/jn.01338.2005 PMID: 16914606

82. Mastronarde DN. Non-lagged relay cells and interneurons in the cat lateral geniculate nucleus:Receptive field properties and retinal inputs. Visual Neuroscience. 1992; 8:407–441. https://doi.org/10.1017/S0952523800004934 PMID: 1586644

83. Alitto HJ, Usrey WM. Corticothalamic feedback and sensory processing. Current Opinion in Neurobiology. 2003; 13(4):440–445. https://doi.org/10.1016/S0959-4388(03)00096-5 PMID: 12965291

84. Blitz DM, Regehr WG. Timing and specificity of feed-forward inhibition within the LGN. Neuron. 2005; 45(6):917–928. https://doi.org/10.1016/j.neuron.2005.01.033 PMID: 15797552

85. Einevoll GT, Plesser HE. Linear mechanistic models for the dorsal lateral geniculate nucleus of cat probed using drifting-grating stimuli. Network: Computation in neural systems. 2002; 13:503–530. https://doi.org/10.1088/0954-898X_13_4_305

86. Einevoll GT, Halnes G. Lateral Geniculate Nucleus (LGN) Models. In: Jaeger D, Jung R, editors. Encyclopedia of Computational Neuroscience. Springer; 2015. p. 1–7.

87. Guillery R, Harting JK. Structure and connections of the thalamic reticular nucleus: advancing views over half a century. Journal of Comparative Neurology. 2003; 463(4):360–371. https://doi.org/10.1002/cne.10738 PMID: 12836172

88. Wang X, Sommer FT, Hirsch JA. Inhibitory circuits for visual processing in thalamus. Current Opinion in Neurobiology. 2011; 21(5):726–733. https://doi.org/10.1016/j.conb.2011.06.004 PMID: 21752634

89. Rogala J, Waleszczyk WJ, Leski S, Wrobel A, Wojcik DK. Reciprocal inhibition and slow calcium decay in perigeniculate interneurons explain changes of spontaneous firing of thalamic cells caused by cortical inactivation. Journal of Computational Neuroscience. 2013; 34:461–476. https://doi.org/10.1007/s10827-012-0430-8 PMID: 23150147

90. Turner JP, Salt TE. Characterization of sensory and corticothalamic excitatory inputs to rat thalamocortical neurones in vitro. Journal of Physiology. 1998; 510 (Pt 3):829–843. https://doi.org/10.1111/j.1469-7793.1998.829bj.x PMID: 9660897

91. Kielland A, Heggelund P. AMPA and NMDA currents show different short-term depression in the dorsal lateral geniculate nucleus of the rat. Journal of Physiology. 2002; 542(Pt 1):99–106. https://doi.org/10.1113/jphysiol.2002.019240 PMID: 12096054

92. Boudreau CE, Ferster D. Short-term depression in thalamocortical synapses of cat primary visual cortex. Journal of Neuroscience. 2005; 25(31):7179–7190. https://doi.org/10.1523/JNEUROSCI.1445-05.2005 PMID: 16079400

93. Stoelzel CR, Bereshpolova Y, Gusev AG, Swadlow HA. The impact of an LGNd impulse on the awake visual cortex: synaptic dynamics and the sustained/transient distinction. Journal of Neuroscience. 2008; 28(19):5018–5028. https://doi.org/10.1523/JNEUROSCI.4726-07.2008 PMID: 18463255

94. Augustinaite S, Yanagawa Y, Heggelund P. Cortical feedback regulation of input to visual cortex: role of intrageniculate interneurons. Journal of Physiology. 2011; 589:2963–2977. https://doi.org/10.1113/jphysiol.2011.205542 PMID: 21502287

95. Lindström S, Wróbel A. Frequency dependent corticofugal excitation of principal cells in the cat's dorsal lateral geniculate nucleus. Experimental Brain Research. 1990; 79(2):313–318. https://doi.org/10.1007/BF00608240 PMID: 2323378

96. Sherman SM. Dual response modes in lateral geniculate neurons: Mechanisms and functions. Visual Neuroscience. 1996; 13:205–213. https://doi.org/10.1017/S0952523800007446 PMID: 8737271

97. Zhu JJ, Uhlrich DJ, Lytton WW. Burst firing in identified rat geniculate interneurons. Neuroscience. 1999; 91(4):1445–1460. https://doi.org/10.1016/S0306-4522(98)00665-4 PMID: 10391450

98. Rivadulla C, Martinez L, Grieve KL, Cudeiro J. Receptive field structure of burst and tonic firing in feline lateral geniculate nucleus. Journal of Physiology. 2003; 553(2):601–610. https://doi.org/10.1113/jphysiol.2003.048561 PMID: 12972624

99. Lesica NA, Stanley GB. Encoding of natural scene movies by tonic and burst spikes in the lateral geniculate nucleus. Journal of Neuroscience. 2004; 24(47):10731–10740. https://doi.org/10.1523/JNEUROSCI.3059-04.2004 PMID: 15564591

100. Alitto HJ, Weyand TG, Usrey WM. Distinct properties of stimulus-evoked bursts in the lateral geniculate nucleus. Journal of Neuroscience. 2005; 25(2):514–523. https://doi.org/10.1523/JNEUROSCI.3369-04.2005 PMID: 15647497

101. Lesica NA, Weng C, Jin J, Yeh CI, Alonso JM, Stanley GB. Dynamic encoding of natural luminance sequences by LGN bursts. PLoS Biology. 2006; 4(7):e209. https://doi.org/10.1371/journal.pbio.0040209 PMID: 16756389

102. Gilbert CD Laminar differences in receptive of receptive field properties of cells in car primary visual cortex. Journal of Physiology. 1977; 268:391–421. https://doi.org/10.1113/jphysiol.1977.sp011863 PMID: 874916

103. Hill S, Tononi G. Modeling sleep and wakefulness in the thalamocortical system. Journal of Neurophysiology. 2005; 93(3):1671–1698. https://doi.org/10.1152/jn.00915.2004 PMID: 15537811

104. Sompolinsky H, Shapley R. New perspectives on the mechanisms for orientation selectivity. Current Opinion in Neurobiology. 1997; 7(4):514–522. https://doi.org/10.1016/S0959-4388(97)80031-1 PMID: 9287203

105. Somers DC, Nelson SB, Sur M. An emergent model of orientation selectivity in cat visual cortical simple cells. Journal of Neuroscience. 1995; 15(8):5448–5465. PMID: 7643194

106. Sclar G, Freeman R. Orientation selectivity in the cat's striate cortex is invariant with stimulus contrast. Experimental Brain Research. 1982; 46(3):457–461. https://doi.org/10.1007/BF00238641 PMID: 7095050

107. Potjans TC, Diesmann M. The cell-type specific cortical microcircuit: relating structure and activity in a full-scale spiking network model. Cerebral Cortex (New York,NY:1991). 2014; 24:785–806.

108. Olsen SR, Bortone DS, Adesnik H, Scanziani M Gain control by layer six in cortical circuits of vision. Nature 2012; 483:47–52. https://doi.org/10.1038/nature10835 PMID: 22367547